On the Wake Flow behind a Sphere in a Pipe Flow at Low Reynolds Numbers

Guang Yin (尹光)[a], Muk Chen Ong*[a]

[a] Department of Mechanical and Structural Engineering and Materials Science,
University of Stavanger, N-4036 Stavanger, Norway

Abstract

Numerical simulations are carried out to investigate the flow around a stationary sphere in a pipe. Seven sphere diameters $d = 0.1D \sim 0.9D$ (D is the diameter of the pipe) are chosen to investigate the effects of the blockage ratio on the flow characteristics. Three series of simulations are conducted. The first series of simulations is based on a fixed pipe flow Reynolds number $Re_p = 1250$ (based on the inlet mean velocity and D) and the sphere Reynolds number Re_s (based on the sphere cross-section mean velocity and d) is varying in the range of $249 \leq Re_s \leq 1360$. The second series of simulations is based on a fixed $Re_s = 500$ and Re_p varying between $460 \leq Re_p \leq 678$. The third series of simulations is based on a fixed $Re_g = 500$ (based on the mean velocity of flow through the gap between the sphere and the pipe wall and d) and Re_p varying between $113 \leq Re_p \leq 773$. The instantaneous vortical structures are presented to show different flow patterns behind the spheres with different d. For the sphere with the small diameter ($d \leq 0.5D$), the vortex shedding in the wake flow behind the sphere is similar to that with the sphere subjected to a uniform flow. However, for the sphere with larger diameter ($d \geq 0.7D$), the flow behind the sphere is different from the sphere subjected to a uniform flow. At $Re_p = 1250$, the large-scale vortex shedding behind the sphere is suppressed for $d \geq 0.8D$ and strong small-scale vortical structures are formed behind the sphere. At $Re_s = 500$, different behaviors of wake flow are observed with the increasing d. It is found that the vortex shedding is stabilized for $0.4D \leq d \leq 0.7D$ due to the confinement of the pipe wall while the wake vortices become chaotic for $d \geq 0.8D$ due to the interaction between the wake flow and pipe wall boundary layer. The vortex shedding is suppressed for $d \geq 0.9D$. At $Re_g = 500$, the wake flow behind the sphere is stabilized with the increasing d. The combined effects of the blockage ratio and Reynolds number on the flow pattern in the wake region, the hydrodynamic quantities of the sphere and the power spectra of the velocities at different detection points are discussed in detail. Furthermore, in addition to power spectra analysis, sparsity-promoted Dynamic Mode Decomposition (SPDMD) is used to analyze the dominant flow modes in the wake region for different blockage ratios. The dominant flow characters associated with the hairpin vortex shedding, the Kelvin-Helmholtz (KH) instability and the low-frequency modulation of the wake flow can be captured by the DMD modes, and their spatial structures are revealed by the mode shapes.

1. Introduction

A flow past a stationary sphere is one of the most classical problems in fluid mechanics and a simplified example of bluff-bodies immersed in flows with wide industrial applications. There

---

* Corresponding author.
Email address: muk.c.ong@uis.no

Physics of Fluids ACCEPTED MANUSCRIPT
This is the author's peer reviewed, accepted manuscript. However, the online version of record will be different from this version once it has been copyedited and typeset.
PLEASE CITE THIS ARTICLE AS DOI:10.1063/5.0017349
AIP Publishing

have been a large number of studies on the subject due to the complex three-dimensional flow characteristics. Experimental and numerical studies have shown that the flow displays different behaviors behind a sphere at different ranges of Reynolds number, which are usually defined based on the sphere diameter and the inflow characteristic velocity as $Re = Ud/\nu$ (ν is the kinematic viscosity of the fluid and U is the velocity of the incoming flow and d is the sphere diameter). The flow starts to separate from the sphere and a steady, axisymmetric vortex ring appears at $Re = 20$. Then when Re exceeds 130, a long periodic motion is formed behind the vortex ring (Taneda[59]). At $Re = 190$, the steady wake becomes non-axisymmetric and eventually becomes unstable at $Re = 270$. The unsteady vortex then begins to shed from the sphere and generates hairpin-like vortices. Due to the experimental conditions, the Reynolds number at which the onset of the laminar vortex shedding takes place covers a large range of $Re = 290{\sim}400$ (Sakamoto and Haniu[45, 46]; Achenbach[1]). The vortex shedding at this Re range happens in a periodic manner with a single frequency corresponding to a vortex shedding Strouhal number St_{VS} (defined as $St_{\mathrm{VS}} = f_{\mathrm{VS}}d/U$ with f_{VS} referred to the vortex shedding frequency). According to the previous published studies reported by Achenbach, Mittal and Najjar[32], Gushchin et al.[12], Kim and Durbin[20] and Rodríguez et al.[43], the typical range of St_{VS} is $0.13 < St_{\mathrm{VS}} < 0.2$. At $Re < 420$, the large-scale shedding hairpin-like vortices can remain planar symmetry and their heads are located on one side. It is reported by Gushchin et al.[12] that for $Re > 600$, there is rotation of the hairpin-like vortices in the wake flow behind a sphere. As Re further increases, a small-scale, shear-layer Kelvin-Helmholtz (KH) instability occurs on the fringe of the wake region and leads to a secondary mode with a higher frequency denoted as St_{KH} (Kim and Durbin[20]; Tomboulides et al.[62]; Mittal and Najjar[32]; Lee[26]). The onset of KH instability was reported experimentally by Sakamoto and Haniu[45] to occur at $Re \approx 800$ while according to the direct numerical simulations (DNS) carried out by Mittal and Najjar[32], KH instability takes place at $Re \approx 650$. The two modes can coexist at a Reynolds number up to $Re{\sim}10^5$ (Kim and Durbin[20]; Chomaz et al.[4]). The frequency of the high mode grows with increasing Re (Sakamoto and Haniu[45]; Mittal and Najjar[32]). Some typical values of St_{KH} are reported as $St_{\mathrm{KH}} = 0.175$ at $Re = 880$ (Gushchin et al.,[12]), $St_{\mathrm{KH}} = 0.72$ at $Re = 3700$ (Rodríguez et al.,[43]) and $St_{\mathrm{KH}} = 1.77$ at $Re = 10000$ (Rodríguez et al.,[44]). Apart from St_{VS} and St_{KH}, it has been widely reported that there is an additional low frequency mode with St_{m} at $Re > 250$. The value of St_{m} varies from 0.0178 (Rodríguez et al.,[43]) to 0.05 (Constantinescu and Squirs,[6]). As mentioned by Rodríguez et al.[43], this low frequency can be related to the shrinkage and enlargement of the recirculation region behind the sphere. Similar phenomena were also observed in the separation bubbles behind a back-face step (Nadge and Govardhan,[33]) or induced by suction-blowing velocity profiles (Wu et al.,[68]). The modulation of the separation region can be described as ‘breathing’ or ‘flapping’ of the separated shear layer, which can be also observed in the form of the quasiperiodic lift and drag coefficients of the sphere as shown in Tiwari et al.[61].

The vortex street behind a sphere remains laminar up to $Re \approx 1000$; and with the further increasing Re, the shear layer instability induces even higher frequency mode with an amplitude 40% larger than that of the primary vortex shedding. The wake region behind a sphere undergoes transition to turbulence at $Re \approx 3000$ and becomes fully turbulence at $Re \approx 6000$ as reported by Sakamoto and Haniu[45]. There have been numerous numerical and experimental investigations on a flow past a sphere at these high Reynolds numbers. Direct numerical simulation (DNS) was used by Seidl et al.[49] at $Re = 5000$ to uncover the physics of vortex shedding in the wake region. Large Eddy Simulation (LES) and Detached Eddy Simulation (DES) have been carried out at $Re =$

Physics of Fluids ACCEPTED MANUSCRIPT

$3700{\sim}2\times10^4$ (Kim and Choi[21]; Constantinescu and Squires[6]; Tomboulides and Orzag[63]) to study the hydrodynamics on the sphere as well as the shedding frequencies. Turbulent quantities have been studied at $Re=5\times10^4$ by LES (Schmid and Perić [48]). Recently, Rodríguez et al.[43] carried out detailed DNS to investigate a uniform flow past a sphere at $Re=3700$ and a power spectra analysis of the velocities behind the sphere was conducted.

The above investigations all focused on a flow around a sphere located in an infinitively large domain while more interesting phenomena can be expected when the sphere is located in a pipe. There are many examples in subsea engineering, biomedical engineering and chemical engineering where submerged bodies are placed in a pipe flow, such as ores in lifting pipe in deep sea mining, red blood cells in capillaries and pulverized coal in combustion chamber. These submerged bodies are usually moving in the pipe flow. Their dynamics are determined by the drag force on them and the forces on these bodies are highly influenced by the hydrodynamics interactions with the pipe wall. Therefore, it is significant to investigate the hydrodynamics characteristics of these bodies in the pipe flow. A sphere in the pipe flow can be regarded as the simplest case of these types of flow problems, which can be foundations of understanding the hydrodynamic characteristics of the submerged bodies in pipe flows. Different from the sphere in an infinitively large domain, the hydrodynamics of the sphere may be subjected to the effect of the pipe wall. The vortex strength and the circulation density on the surface of the sphere with varying blockage ratio (BR defined as the ratio between the sphere diameter d and the pipe diameter D) have been first given theoretically by Smythe[53] based on the potential flow theory. The blockage effects of the pipe wall on the drag and lift coefficients on the sphere have been studied in creeping flows at low Reynolds number (Haberman and Sayre[13]). Fayon and Happel[8] gave a semiempirical formula for the drag on the sphere, which is associated with the effect of the pipe wall and the inertial effects at $Re<40$ with the blockage ratio $BR=0.125{\sim}0.3125$. New correlations of the drag on the sphere under the influence of the pipe wall were determined by Wham et al.[65] at higher Re ($Re{\sim}100$) with $BR=0.08{\sim}0.7$. It was also shown that the critical Re to generate the wake and the length of the wake are also affected by BR. Experiments and numerical simulations at $Re=20{\sim}130$ of Oh and Lee[37] revealed that the size of the vortex decreases and the drag on the sphere increases with increasing BR. Except for the hydrodynamics, the heat transfer over the sphere has also been extensively studied. The drag and lift coefficients on the sphere placed eccentrically in a pipe and the Nusselt number, which characterizes the heat flux, have been studied by Shahcheraghi and Dwyer[50]. It was shown that a lift force is induced by the off-centered position and its value varies with Re. The blockage effect results in a significant change of the pressure distribution on the sphere. However, due to the limited Re (i.e. $Re=25$ and 125) under investigations, the influence of the pipe wall on the Nusselt numbers are not observed compared with the sphere placed in an external uniform flow. Krishnan and Kannan[24] extended the study for the cases at Re up to 500 using numerical simulations. It was found that the separation of the flow around the sphere is delayed due to high BR. The new relationships between the hydrodynamic and thermodynamic quantities (such as drag coefficients, boundary layer separation angle, the averaged Nusselt number) and Re as well as BR were proposed in their study. Furthermore, the effects of the eccentrically sphere positions were also investigated by Krishnan and Kannan[57]. It was shown that at low Re, the drag coefficient on the sphere decreases when the sphere was positioned eccentrically with respect to the tube axis while at high Re, the drag coefficient increases with increasing eccentric positions of the sphere towards the pipe wall. The separations of the boundary layer around the

Physics of Fluids ACCEPTED MANUSCRIPT

This is the author's peer reviewed, accepted manuscript. However, the online version of record will be different from this version once it has been copyedited and typeset.
PLEASE CITE THIS ARTICLE AS DOI:10.1063/5.0017349

AIP Publishing

sphere are also affected by the eccentric positions even at a very low Re. Moreover, many studies focused on this configuration with different conditions, such as investigations on viscoelastic fluid past a sphere in a pipe (Zheng et al.[71]), and a flow past a series of moving spheres (Yang et al.[69], Sheard and Ryan[51]) in a pipe. Furthermore, there are several studies considering the wall effects on the wake flow behind bluff bodies when they are placed in an internal flow. Singha and Sinhamahapatra[52] carried out two-dimensional simulations of flow past a cylinder between two parallel walls at low Re with different BR. It was found that the separation points move rearward and the wake region behind the cylinder becomes shorter with the increasing BR. The mean drag and vortex shedding frequency become significantly large with high. Three-dimensional DNS study of flow around cylinder in a channel was carried out by Kanaris et al.[19] to study the confinement of the wall on the evolution and shape of the two instability modes in the wake flow behind the cylinder. It was found by Mathupriya et al.[30] using three-dimensional DNS that the interaction between the wake flow behind a cylinder and the boundary layer on the channel wall induces counter rotating spanwise vortices, which influence the properties of the wake flow.

According to the state of art, even though the effects of the pipe wall on the hydrodynamics and the heat transfer on the sphere have been reported, to the author's knowledge, most of the previous benchmark studies of this type of flow problems such as Smythe[53], Fayon and Happel[8], Wham et al.[65] and Oh and Lee[37] used potential flow theory or investigated low Reynolds number flow at $Re < 150$. How are the flow structures different from those behind an isolated sphere subjected to external uniform flows with the gradually increasing BR? How are the hydrodynamic quantities of the sphere different from those of an isolated sphere subjected to external uniform flows? How does the pipe wall influence the wake flow behind the sphere? These complicated problems have not been investigated in detail in the mentioned studies. The present study attempts to investigate these problems by provide detailed discussion on hydrodynamic forces on the sphere and the flow structures behind the sphere in a laminar pipe flow. The results of the present study can also be used as a baseline for further investigations of this type of flow problems. In the present study, numerical simulations are carried out to investigate the flow characters behind a sphere located centrally in a laminar pipe flow. Three Reynolds numbers are discussed. The first series of simulations are based on a fixed pipe Reynolds number to investigate the influence of BR on the wake flow structures. The second and third series of simulations are based fixed sphere Reynolds numbers to investigate the influence of BR on the hydrodynamic quantities of the sphere. The outline of the paper is as follows. First, mathematical formulations and numerical methods are described in Section 2. The convergence and the validation studies are also presented. The results and discussions are given in Section 3 and finally the conclusions are made in Section 4.

2. Numerical Set up

2.1. Mathematical formulations and numerical methods

The governing equations of the viscous, incompressible and laminar flow are

$$\frac{\partial u_i}{\partial x_i} = 0 \tag{1}$$

$$\frac{\partial u_i}{\partial t} + u_j \frac{\partial u_i}{\partial x_j} = -\frac{1}{\rho}\frac{\partial p}{\partial x_i} + \nu \frac{\partial^2 u_i}{\partial x_j \partial x_j} \tag{2}$$

where x_i $(i = 1,2,3$ for $x, y, z)$ represent the three directions in a Cartesian coordinate system. u_i

($i = 1,2,3$ for u, v, w) are the corresponding velocity components and p is the pressure. ρ and ν are the density and kinematic viscosity, respectively.

The open source Computational Fluid Dynamics code OpenFOAM is employed in the present study to discretize the governing equations using the finite volume method (FVM). The PISO (Pressure Implicit with Splitting of Operators) scheme-based solver, icoFoam is used to carry out the simulations. The spatial discretization of the gradient term, Laplacian term and divergence term in the governing equations are Gauss linear and in second order. The second-order Euler scheme is used for the time integrations.

2.2. Computational overview, convergence studies and validation

2.2.1. Computational overview

The computational domain of the present study is shown in Figure 1. The center of the sphere is located on the axis of the pipe with a distance of $Lu = 5D$ (D is the diameter of the pipe) from the center of the sphere to the inlet of the pipe and $Ld = 7.5D$ from the center of the sphere to the outlet. Two examples of a small sphere and a large sphere are also shown in Figure 1. It was shown in Krishnan and Kaman[24] that a computational domain with $Lu = 5D$ and $Ld = 7.5D$ is sufficient to provide convergent hydrodynamic forces on the sphere. An additional investigation on the influence of computational domain sizes is presented in Appendix A. At the inlet, a parabolic laminar velocity profile $u(r) = U_{\max}[1 - (r/R)^2]$ $(0 \leq r \leq R)$, $v = 0$ and $w = 0$ is prescribed, where $U_{\max} = 2\mathrm{m/s}$ is the central line velocity of the pipe flow and r is the distance to the pipe center line and $R = D/2$ is the radius of the pipe. The pressure is set to be zero normal gradient at the inlet. At the outlet, the velocities are specified as zero normal gradient boundary conditions and the pressure is set to be zero. On the pipe wall surface and the sphere surface, no-slip boundary condition is used for the velocities, $u = v = w = 0$ and the pressure is set to be zero normal gradient.

Figure 1 Computational domain and an example view of the sphere with $BR = 0.4$ and $BR = 0.8$.

The important parameters are non-dimensionalized by the characteristic length and velocity of the pipe flow. As suggested by Krishnan and Kaman[24], there are three types of Reynolds number Re based on three characteristic velocities and two characteristic lengths: (1) the pipe $Re_p = \bar{U}D/\nu$ based on the pipe flow rate velocity $\bar{U} = 1\mathrm{m/s}$ and pipe diameter D; (2) the sphere $Re_s = U_s d/\nu$ based on the inlet cross-section averaged velocity of the sphere $U_s = Q(r)/(\pi r^2) = 2(1 - 2r^2)$ (where $Q(r)$ is the flow rate within the cross-section of the sphere calculated by $Q(r) = 2\pi \int_0^r u(r')r'dr'$. r' is the integral variable in the range between 0 and r. $r = d/2$ is the radius of the sphere) and the sphere diameter d; (3) the sphere $Re_g = U_g d/\nu$ based on the averaged velocity of the flow through the gap between the sphere and the pipe wall $U_g = Q(r)/(\pi(R^2 - r^2))$. Therefore, three series of simulations are carried out in the present study and the values of the three Reynolds numbers for each series are listed in Tables 1 to 3. It is worth mentioning that at the highest pipe Reynolds number of $Re_p = 1250$ of these simulations, the pipe flow remains laminar and the pipe wall can further act as stabilization to suppress turbulence disturbance in the sphere wake region.

Table 1 Cases at a fixed $Re_p = 1250$ and their corresponding Re_s and Re_g

BR	$Re_s = U_s d/\nu$	$Re_p = \bar{U}D/\nu$	$Re_g = U_g d/\nu$
0.1	249	1250	126
0.2	490	1250	260
0.4	920	1250	595
0.5	1094	1250	833
0.6	1230	1250	1172
0.7	1321	1250	1715.69
0.8	1360	1250	2778
0.9	1338.75	1250	5921

Table 2 Cases at a fixed $Re_s = 500$ and their corresponding Re_p and Re_g

BR	$Re_s = U_s d/\nu$	$Re_p = \bar{U}D/\nu$	$Re_g = U_g d/\nu$
0.4	500	678	323.5
0.5	500	556	381
0.6	500	500	476
0.7	500	476	649
0.8	500	460	1021
0.9	500	467	2211

Table 3 Cases at a fixed $Re_g = 500$ and their corresponding Re_p and Re_s

BR	$Re_s = U_s d/\nu$	$Re_p = \bar{U}D/\nu$	$Re_g = U_g d/\nu$
0.4	1050	773	500
0.5	750	656	500
0.6	533	525	500
0.7	364	385	500
0.8	225	244.8	500
0.9	105	113	500

2.2.2. Convergence studies and validation studies

First, detailed mesh convergence studies are carried out for all cases in Table 1. As the pipe flow Reynolds number in Table 1 is larger than those in Tables 2 and 3, the grid resolutions which can provide convergent results in Table 1 can be used for the simulations in Tables 2 and 3. A body-fitted, structured mesh is used, and the grids are progressively refined near the sphere surface and pipe wall to resolve the boundary layer. For each BR, the number of the grids within the boundary layer (its thickness is approximated by $\delta \approx 1/\sqrt{Re_s}$ suggested by Johnson and Patel[16]) near the sphere surface varies from 5 to at least 10 for the finest mesh. This boundary layer resolution criterion is close to that was adopted in Lee[26], Rodríguez et al.[43] and Nagata et al.[34, 35]. The meshes are similar to those used in Poon et al.[41], where a quadrilateral shape arrangement of the hexahedra cells around the centerline are used as shown in Figure 2 in order to avoid a numerical singularity when rotating the mesh in the azimuthal direction. The number of the planes in the azimuthal direction is set to be around 80~100 which is close to the number used in Rodríguez et al. [43]. For large $BR \geq 0.5$, since the hydrodynamic interaction between the wake flow behind the sphere and the pipe wall boundary layer is strong, the grids near the pipe wall are further refined and a *posterior* test have been conducted to guarantee that the maximum value of y^+ (calculated by $y^+ = u^* \Delta y/\nu$ where u^* is the friction velocity on the pipe wall and Δy is the distance to the next point away from the pipe wall) near the pipe wall is around 1.0 even for the largest $BR = 0.9$. The detained results of the grid resolution studies are shown in Appendix A.

Figure 2 Computational grids. (a) YZ view at the inlet; (b) XZ view around the sphere for $BR = 0.2$ and (c) XZ view around the sphere and near the pipe wall for $BR = 0.8$

As stated in Section 2.2.1, the nonuniformity of the incoming flow is strong and the flow past the sphere is different from that is subjected to a uniform flow in the previous published studies. Therefore, additional simulations have also been carried out for a sphere subjected to a uniform flow to validate the present numerical model. For the uniform flow cases, the same grid resolutions of Cases A4 in Table 7 in Appendix A are used and the radial length of the computational domain is extended to $R = 14r$, which is the same as that used in Tiwari et al.[61] and larger than that used in Rodríguez et al. [43]. a uniform flow of $U_{max} = 2\mathrm{m}/s$ is prescribed at the inlet and a slip wall boundary condition is used at the pipe wall as suggested by Lorite-Díez and Jiménez-González[28]. Table 4 shows the present predicted time-averaged drag and lift coefficients defined as Eqs. 3 and 4 for the uniform flow case. The results are compared with the previous published data and the result obtained using the empirical relationship of Eq. 5 proposed by Subramanian[56] at $Re_s = 250$

$$\overline{C_d} = 2\overline{F_x}/\left(\rho {U_{\max}}^2 A\right) \tag{3}$$

$$\overline{C_l} = \sqrt{\overline{C_y^2 + C_z^2}} \tag{4}$$

$$\left(C_y = 2F_y/\left(\rho {U_{\max}}^2 A\right), C_z = 2F_z/\left(\rho {U_{\max}}^2 A\right)\right)$$

$$\overline{C_d} = \frac{24}{Re_s}\left[1 + 0.1935 {Re_s}^{0.6305}\right] \qquad (20 \leq Re_s \leq 260) \tag{5}$$

where F_x, F_y, F_z is the time-averaged force on the sphere in the three directions, which are obtained by integrating the pressure and shear stress on the sphere surface and $A = \pi r^2$ is the reference area of the sphere. Furthermore, the streamlines in two cross-section planes at $x/d = 1$ and 7 are

Physics of Fluids ACCEPTED MANUSCRIPT
AIP Publishing
This is the author's peer reviewed, accepted manuscript. However, the online version of record will be different from this version once it has been copyedited and typeset.
PLEASE CITE THIS ARTICLE AS DOI:10.1063/5.0017349

compared with those in Tiwari et al.[61] at $Re_s = 250$ in Figure 3. At this Re_s, the wake flow behind the sphere is planar symmetry. As suggested by Johnson and Patel[16], after the onset of the loss of axial symmetry, the orientation of the symmetry plane can be arbitrary. In Figure 3, the vortex positions of the present results are rotated to show a clear comparison with the results in Tiwari et al.[61]. The present study shows two similar vortical structures behind the sphere to those reported in Tiwari et al.[61].

In addition, at a higher $Re_s = 300, 350$ and 400, the wake flow becomes unsteady and periodic large-scale vortex shedding takes place. The values of $\overline{C_d}$, $\overline{C_l}$ and St_{VS} obtained by the present simulations for the uniform cases are compared with those reported in the previous studies in Table 5. It is shown that the present predicted value of $\overline{C_d}$ of the present study at these Re_s are close to that obtained using DNS and the empirical relationship given as

$$\log_{10}(\overline{C_d}) = 1.6435 - 1.1242\log_{10}(Re_s) + 0.1558\log_{10}(Re_s)^2 \qquad (Re_s \geq 260) \qquad (6)$$

The differences between the predicted $\overline{C_l}$ and those of previous studies are within 6%. Since the value of $\overline{C_l}$ is small and sensitive, the predicted value can be in reasonable agreement with those reported in the previous studies. The present predicted value of St_{VS} is also close to those of the previous studies. Figure 4 (a) shows the present predicted time-averaged streamwise velocity along the centerline of the pipe at $Re_s = 300$ compared with the experimental data reported in Wu and Faeth[67] at $Re_s = 280$ and the numerical results obtained by Tomboulides and Orszag[62] at $Re_s = 280$, where a satisfactory agreement is achieved. Figures 4 (b)~(d) show the present predicted pressure distributions defined as $C_p = 2(p - p_\infty)/(\rho U_s^2)$ (where p_∞ is the pressure of the incoming flow at infinity) on the sphere at $Re_s = 250, 300$ and 350 compared with the data in the previous studies carried out by Wu and Faeth[67], Le Clair et al.[25], Magnaudet et al.[29] and Bagchi et al.[2] at the same Re_s. Here, p is the pressure at the angle of ϕ^o measured clockwise from the stagnation point. The present predicted pressures show similar distributions to the data reported in these studies.

Table 4 Comparisons between the present results for $BR = 0.1$ subjected to a uniform flow and the previous published experimental and numerical data at $Re_s = 250$

Case	Re_s	$\overline{C_d}$	$\overline{C_l}$	L_w
Present/Num.	250	0.707	0.0612	1.787
Empirical formula (5)	250	0.6997	-	-
Clift et al.[5]/Exp.	250	0.70	-	-
Lee[26]/Num.	250	-	1.78	1.78
Lorite-Díez and Jiménez-González[28]/Num.	250	0.705	0.061	-
Poon et al.[41]	250	0.702	0.061	-
Johnson and Patel[16]	250	0.70	0.062	-
Kim and Choi[21]	250	0.702	0.06	-

Physics of Fluids ACCEPTED MANUSCRIPT

This is the author's peer reviewed, accepted manuscript. However, the online version of record will be different from this version once it has been copyedited and typeset.

PLEASE CITE THIS ARTICLE AS DOI:10.1063/5.0017349

AIP Publishing

Table 5 Comparisons between the present results for $BR = 0.1$ subjected to a uniform flow and the previous published experimental and numerical data at $Re_s = 300, 350$ and 400

Case	Re_s	$\overline{C_d}$	$\overline{C_l}$	St_{VS}
Present/Num.	300	0.661	0.071	0.133
Empirical formula (6)	300	0.657	-	-
Campregher et al.[3] /Num.	300	0.675	-	-
Tiwari et al.[61] /Num.	300	-	-	0.134
Johnson and Patel[16] /Num.	300	0.656	0.069	0.137
Tomboulides[62] /Num.	300	0.671	-	0.136
Poon et al.[41] /Num.	300	0.658	0.067	0.134
Kim et al.[23]/Num.	300	0.660	0.068	0.134
Present	350	0.628	0.066	0.135
Empirical formula	350	0.62	-	-
Tiwari et al. [61] /Num.	350	-	0.062	0.134
Mittal et al.[32] /Num.	350	0.62	-	0.138±0.003
Bagchi et al.[2] /Num.	350	0.62	-	0.135
Present	400	0.599	0.0524	0.13
Empirical formula	400	0.594	-	-
Campregher et al. [3] /Exp.	400	0.594	-	-
Goldburg and Florsheim[11] /Exp.	400	-	-	0.127
Sakamoto and Haniu[45] /Exp.	400	-	-	0.13-0.145
Lee[26] /Num.	400	0.5775	-	0.137
Kalro and Tezduyar[18] /Num.	400	0.59	-	0.131
Kim et al. [23] /Num. $Re = 425$	425	0.589	0.0589	0.144

Figure 3 Time-averaged streamlines on two constant x/d planes at (a) $x/d = 1$ and (b) $x/d = 7$ for $BR = 0.1$ at $Re_s = 250$ for the sphere subjected to a uniform flow of the present study (Left. The blue dashed lines indicate the sphere) compared with those in Tiwari et al. [61] (Right) at the same streamwise locations. The color contours denote the value of the time-averaged streamwise velocity.

Figure 4 (a) The time-averaged streamwise velocity along the centerline of the pipe at $Re_s = 300$; the pressure distributions on the sphere at (b) $Re_s = 250$; (c) $Re_s = 300$; (d) $Re_s = 350$ (solid lines: present study; red circles: experimental data in Wu and Faeth[67] at $Re_s = 280$; dashed: DNS data in Tomboulides and Orszag[62] at $Re_s = 200$; red diamond: Le Clair et al.[25] at $Re_s = 300$; blue square: Magnaudet et al.[29] at $Re_s = 300$; Dash-dotted: Bagchi et al.[2] at $Re_s = 350$)

Physics of Fluids ACCEPTED MANUSCRIPT

3. Results and discussion

3.1. Flow visualization

The Q criterion (Hunt et al.[14]) is used to analyze the vortical structures behind the sphere in the present study. The Q is defined as the difference between the strain and the rotation tensor:

$$Q = -(\|\boldsymbol{S}\|^2 - \|\boldsymbol{\Omega}\|^2)/2 \tag{7}$$

where $\boldsymbol{S}$ and $\boldsymbol{\Omega}$ denote the strain and the rotation tensors, respectively.

Figures 5 and 6 show the instantaneous vortical structures identified by Q for all BRs at $Re_p = 1250$ and at $Re_s = 500$. The iso-surfaces of Q are colored by the time-averaged streamwise velocity. In Figure 5, the iso-surface value of $Q = 2$ is used. First, it is obvious that when $BR > 0.2$, due to the blockage effect, there is backflow in front of the sphere where a vortex ring is formed. It can be seen that for $BR = 0.1$, $Re_p = 1250$ and $Re_s = 249$, the wake flow is steady and asymmetry with only two weak streamwise vortices, which is consistent with those reported in Tiwari et al. [61]. For $BR = 0.2$, the wake flow is unsteady and asymmetric. There is a periodic vortex shedding behind the sphere. The hairpin vortical structure is generated at the initial stage of the vortex shedding and experience dislocation at $3\sim4d$. The vortex dislocation denotes the small vortices detached from the hairpin vortical structure in Tiwari et al. [61], which is also observed in the present study and denoted as 'VD' in Figure 5 (b). It was observed in Kim et al. [23] and Tiwari et al. [61] that in the wake flow behind a sphere in an infinitely large domain, the downstream hairpin vortices can orient themselves normal to the flow direction as denoted by the arrow in Figure 5 (i). However, in the present study, these normal orienting hairpin vortices are weak and almost disappear with only pairs of two streamwise vortices legs left as seen in Figure 5 (b). This may be due to the mean shear of the incoming flow and the confinement of the pipe wall. For $BR = 0.4$, a similar hairpin vortex is shedding near the sphere and the shear flow between the wake region and the pipe wall induces secondary hairpin vortices as denoted in Figure 5 (c). Furthermore, the disturbances caused by the unsteady wake flow may enter the pipe wall boundary layer and develop into downstream streamwise near-wall vortical ribs (denoted as 'VR' in the Figure 5). For $BR = 0.5$ and 0.6, the secondary vortices near the sphere are becoming stronger and begin to form a larger vortex ring around the wake flow. In these two cases at a higher Re_s compared with the cases of $BR \leq 0.4$, two hairpin vortices can be generated simultaneously, which will be further illustrated in the following section. With the increasing BR up to 0.8, an increasing number of fine vortical structures are formed near the pipe wall compared with those behind the sphere with $BR = 0.6$. For $BR = 0.9$, the vortical structures are becoming even finer with an increasing density compared with those for $BR = 0.8$. Close to the sphere, these vortical structures tend to be in the azimuthal direction while in the downstream region, the structures are more in the streamwise directions.

At $Re_s = 500$, in order to clearly demonstrate the effects of BR, the nondimensional iso-surface value of $Q^* = Qd/U_s = 1$ is used to identify the vortical structures in Figure 6. For $BR = 0.2\sim0.7$, regular hairpin vortices with a similar shape are shedding from the sphere and further travel downstream together with weak secondary vortical structures above the primary hairpin vortices. There is planar symmetry for the wake flows for $BR = 0.4\sim0.7$ and this change from asymmetry for $BR = 0.2$ to planar symmetry may due to the mean shear of the incoming flow as found in Kim et al.[23]. Furthermore, due to the low value of Re_p, the downstream vortical ribs near the pipe wall are weak. For $BR = 0.7$, the shedding hairpin vortices still exist and the vortical ring around the wake is becoming stronger compared with that for $BR = 0.6$. However, for $BR = 0.8$, the flow structures are much different from those with smaller BR. The wake flow becomes more chaotic and the hairpin vortices cannot be viewed by this level of iso-surface. The planar symmetry disappears. The vortical structures in the azimuthal direction are more resulted from the interaction with the pipe wall boundary layer. The downstream vortical ribs (denoted as 'VR') tilted in the streamwise directions are formed. A further detailed view of the vortical structures behind the sphere is shown with the same view in Figure 7 by using a higher iso-surface value of $Q^* = 10$ and it can be seen clearly that there is still large-scale hairpin vortex shedding. However, for $BR = 0.9$, when using the iso-surface value of $Q^* = 10$, it is shown that the large-scale hairpin vortex shedding becomes suppressed and only finer vortical structures compared with those for $BR = 0.8$ are presented in the wake region.

Figure 5 Instantaneous iso-surfaces of $Q = 2$ colored by the time-averaged streamwise velocity at $Re_p = 1250$ for (a) $BR = 0.1$; (b) $BR = 0.2$; (c) $BR = 0.4$; (d) $BR = 0.5$; (e) $BR = 0.6$; (f) $BR = 0.7$; (g) $BR = 0.8$; (h) $BR = 0.9$; (i) $Re_s = 500$ reprint of Tiwari et al.[61]

Figure 6 Instantaneous iso-surfaces of $Q^* = 1$ colored by the time-averaged streamwise velocity at $Re_s = 500$ for (a) $BR = 0.2$; (b) $BR = 0.4$; (c) $BR = 0.5$; (d) $BR = 0.6$; (e) $BR = 0.7$; (f) $BR = 0.8$; (g) $BR = 0.9$

Figure 7 Instantaneous iso-surfaces of $Q^* = 10$ colored by the time-averaged streamwise velocity at $Re_s = 500$ for (a) $BR = 0.8$ and (b) $BR = 0.9$

At $Re_g = 500$, in order to clearly demonstrate the effects of BR, the nondimensional iso-surface value of $Q^* = Qd/U_s = 1$ is used to identify the vortical structures shown in Figure 8. The stabilization of the large-scale vortex shedding behind the sphere can be observed with the increasing BR from 0.4 to 0.7. The planar symmetry of the wake structures for $BR = 0.6$ and 0.7 is similar to the cases at $Re_s = 500$. For $BR = 0.8$ and 0.9, the vortex shedding behind the sphere is suppressed and the wake flow becomes steady. This may be due to the fact that the kinematic viscosities of the pipe flow are extremely large for the two largest BRs to keep the fixed Re_g as seen in Table 3. Therefore, the entire wake flow is stabilized.

Physics of Fluids ACCEPTED MANUSCRIPT

Figure 8 Instantaneous iso-surfaces of $Q^* = 1$ colored by the time-averaged streamwise velocity at $Re_g = 500$ for (a) $BR = 0.4$; (b) $BR = 0.5$; (c) $BR = 0.6$; (d) $BR = 0.7$; (e) $BR = 0.8$; (f) $BR = 0.9$

Figure 9 shows the time sequences of instantaneous vortical structures in the wake flow identified by $Q = 2$ for $BR = 0.2$ with a time interval between two consecutive time instants of $tU_s/d = 4$. The periodic shedding of the hairpin vortex loops is shown with pairs of streamwise vortices. Furthermore, between two consecutive hairpin vortices (denoted as 'V') with a vortex dislocation (denoted as 'VD'), there is another type of un-dislocated hairpin vortex with a weaker vortex head (denoted as 'S') and this is also reported in Tiwari et al. [61]. The head of the hairpin vortex induces a secondary vortex ring (denoted as 'R') due to the interaction with the shear flow outside the wake region. The mean velocity around the two ends of the vortex ring is higher than that in its middle part, which is close to the pipe wall. Therefore, this secondary vortex ring is further stretched to a 'Λ' shape as shown in Figure 9 (d) and travels downstream.

Figure 9 Instantaneous iso-surfaces of $Q = 2$ for $BR = 0.2$ colored by the time-averaged streamwise velocity at $Re_p = 1250$ at (a) $tU_s/d = 150$; (b) $tU_s/d = 154$; (c) $tU_s/d = 158$; (d) $tU_s/d = 162$; (e) $tU_s/d = 166$; (f) $tU_s/d = 170$

For $BR = 0.4$, in order to visualize the vortical structures more clearly in the wake flow, a larger iso-surface value of $Q = 10$ is used for visualization in Figure 10. It can be seen that due to the higher Re_s, there are time instants when the multiple pairs of counter rotation streamwise vortices are formed which will then generate two hairpin vortices at the same location (as denoted by 'MV1' and 'MV2'). The two haripin vortices at some time instants can be oriented towards different radial directions (as denoted by 'MV3'). However due to the different convection velocity, the hairpin vortices travel downstream separately. This phenomenon was also reported in Tiwari et al. [61] and the reason for this incoherency may be attributed to the irregular rotation of separation point in the azimuthal direction on the sphere. At other time instants, there is only one pair of streamwise vortices and a single hairpin vortex (as denoted by 'SV1') is shedding from the near wake. The size of the hairpin vortices is becoming larger and finally break into smaller-scale strutures further downstream.

Figure 10 Instantaneous iso-surfaces of $Q = 10$ for $BR = 0.4$ colored by the time-averaged streamwise velocity at $Re_p = 1250$ at (a) $tU_s/d = 649.52$; (b) $tU_s/d = 651.36$; (c) $tU_s/d = 653.2$; (d) $tU_s/d = 655.04$; (e) $tU_s/d = 656.88$; (f) $tU_s/d = 659.64$; (g) $tU_s/d = 661.48$; (h) $tU_s/d = 663.32$; (i) $tU_s/d = 665.16$; (j) $tU_s/d = 667$

For $BR = 0.6$, the iso-surface value of $Q = 10$ is also used in Figure 11. It can be seen that the formation of multiple pairs of streamwise counter rotation and two hairpin vortices resulted from the shear layer roll-up is more obvious than that for smaller BR. The two hairpin vortices can either entangle with each other, which is also found in Wood et al.[66] and Tamai et al.[58] in the wake behind a semisphere, and convect together (such as ‘MV1’) or travel downstream with different convection velocities (such as ‘MV2’). Furthermore, the heads of the hairpin vortices become oriented towards the cross flow direction as seen in Figure 11 (e) in the downstream region and induce strong secondary vortex rings by interaction with the pipe wall boundary layer denoted by ‘R1’ and ‘R2’. However, different from what is observed in Tiwari et al.[61], the cross flow oriented hairpin vortices will not grow larger but disappear, which may be due to the confinement of the pipe wall. The vortex rings can undergo bending due to the interaction with the mean shear flow. However, different from the ‘Λ’-shaped vortex ring for $BR = 0.2$ as shown in Figure 9 (d), there are time instants when the middle part of the vortex ring is tilted away from the pipe wall and convect faster than its two legs. The vortex ring is then stretched as shown in Figure 11 (d).

Figure 11 Instantaneous iso-surfaces of $Q = 10$ for $BR = 0.6$ colored by the time-averaged streamwise velocity at $Re_p = 1250$ at (a) $tU_s/d = 508.4$; (b) $tU_s/d = 509.5$; (c) $tU_s/d = 510.6$; (d) $tU_s/d = 511.7$; (e) $tU_s/d = 512.8$; (f) $tU_s/d = 513.9$; (g) $tU_s/d = 515$; (h) $tU_s/d = 516.1$; (i) $tU_s/d = 517.2$; (j) $tU_s/d = 518.3$

For $BR = 0.8$, the large value of $Q = 10$ is used to identify the vortical structures in Figure 12. Vortical strucures with high density are observed. The wake flow is chaotic and look similar to turbulent flow. The dynamics of these flow structures are also completely different from those for smaller $BR < 0.8$, which have not been observed or reported in the mentioned relevant studies such as Fayon and Happel[8], Wham et al.[65], Oh and Lee[37] and Krishnan and Kannan[24]. Near the sphere, the shear layer instability and break-down are observed (denoted as ‘SI’) and the vortex rings (denoted as ‘R1’ and ‘R2’) are generated between the shear layer of the wake. The vortex rings are convected downstream and can undergoes bending in the azimuthal direction due to different convection velocity and finally break into smaller-scale flow strucures in Figures 12 (d) and (h). In further downstream regions, more small-scale vortices appear. It is difficult to identify the dynamical evolution of a single vortical strucures near the pipe wall indicating that the time-scales of the flow structures are small. Figure 13 shows the vortical structures identified by a higher value of isosurface of $Q = 100$ and a large amount of small-scale vortical structures near the pipe wall are removed. Only the vortex rings are observed in the near wake region. There is no regular vortex shedding and large-scale haipin vortical structure from the vortex shedding. It also worth mentioning that in the downstream region, there are time steps when small-scale hairpin vortices (denoted as

Physics of Fluids ACCEPTED MANUSCRIPT

AIP Publishing

This is the author's peer reviewed, accepted manuscript. However, the online version of record will be different from this version once it has been copyedited and typeset.
PLEASE CITE THIS ARTICLE AS DOI:10.1063/5.0017349

'HV') togather with quasi-streamwise vortices (denoted as 'QS') appears. They may be related to stretching of the coherent structures within the pipe wall boundary layer due to the shear.

Figure 12 Instantaneous iso-surfaces of $Q = 10$ for $BR = 0.8$ colored by the time-averaged streamwise velocity at $Re_p = 1250$ at (a) $tU_s/d = 258.4$; (b) $tU_s/d = 258.74$; (c) $tU_s/d = 259.08$; (d) $tU_s/d = 259.42$; (e) $tU_s/d = 259.76$; (f) $tU_s/d = 260.1$; (g) $tU_s/d = 260.44$; (h) $tU_s/d = 260.78$

Figure 13 Instantaneous iso-surfaces of $Q = 100$ for $BR = 0.8$ colored by the time-averaged streamwise velocity at $Re_p = 1250$ at (a) $tU_s/d = 258.4$; (b) $tU_s/d = 258.74$; (c) $tU_s/d = 259.08$; (d) $tU_s/d = 259.42$ in Figure 12

3.2 Hydrodynamic quantities

The effect of BR on the hydrodynamic forces is analyzed based on the cases at $Re_s = 500$ and $Re_g = 500$. Figure 14 shows the time histories of instantaneous C_d for $BR = 0.2\sim0.9$ at $Re_s = 500$. The value of C_d is defined based on the characteristic velocity of U_s. It can be seen that for $BR = 0.4\sim0.7$, the variation of C_d with the nondimensional tU_s/d show periodic wave-like behaviors indicating regular vortex shedding. For $BR = 0.7$, there seems to be slightly periodic intermittency along with the primary periodicity and for $BR = 0.8$ and 0.9, the time variation of C_d becomes irregular and the values for $BR = 0.9$ are much larger compared with those for $BR = 0.8$.

Figure 14 The time histories of C_d for (a) $BR = 0.2$; (b) $BR = 0.4$; (c) $BR = 0.5$; (d) $BR = 0.6$; (e) $BR = 0.7$; (f) $BR = 0.8$; (g) $BR = 0.9$

As shown in Figure 6, the wake vortical structures show planar symmetry. The lateral force coefficients C_y, C_z in y and z direction can be projected into the directions parallel and normal to the symmetry plane. This forms two lateral force components defined as C_l (parallel to the symmetry plane) and C_n (normal to the symmetry plane) in the two directions. Figures 15 and 16 shows the phase diagram of (C_d, C_l) and (C_n, C_l) of the sphere at $Re_s = 500$ for $BR = 0.2\sim0.8$. Since the hydrodynamic force coefficients for $BR = 0.9$ are significantly larger than those for $BR \leq 0.8$, the phase diagrams for $BR = 0.9$ are shown independently in Figures 17 (a) and (b). The influences of BR on the dynamic behaviors of the drag and lift forces are clearly revealed in Figure 15. The monotonically increase of averaged value of C_d with the increasing BR while the fluctuation amplitudes of C_d and C_l show a non-monotonic behavior. The flow characteristics for $BR = 0.2$ are close to those with the sphere in an infinitely large domain and a

Physics of Fluids ACCEPTED MANUSCRIPT

This is the author's peer reviewed, accepted manuscript. However, the online version of record will be different from this version once it has been copyedited and typeset.
PLEASE CITE THIS ARTICLE AS DOI:10.1063/5.0017349

AIP Publishing

chaotic behavior is observed for (C_d, C_l). For $BR = 0.4$, the effect of the mean shear of the incoming flow is apparent. The close circle of the diagram indicates the periodicity of the time histories of the two force coefficients and a synchronous behavior is shown for (C_d, C_l). For $BR = 0.4, 0.5$ and 0.6, the pipe wall confines the cross-stream tilting of the large-scale hairpin vortex observed in Tiwari et al. [61] and Kim et al.[23]. The wall confinement may lead to the stabilization of the vortex shedding as seen in Figures 6 (c)~(e). In addition, Kim et al. [23] found that for the uniform incoming flow, the detachment location of the hairpin vortex varies along the azimuthal direction in time while for the uniform shear, the detachment location of the hairpin vortex remains on one side. Similar phenomenon is also observed in Figures 6 (c)~(e), which indicates that the mean shear of the incoming flow may also lead to stabilization effects. The amplitudes of the forces are increasing for $BR = 0.4, 0.5$ and 0.6.The possible reason for the increasing force amplitudes is that the increasing blockage effect of the sphere with the increasing BR causes the acceleration of the surrounding flow, which increases the amplitude of the shear force as well as the pressure difference on the sphere. Furthermore, for $BR = 0.7$, the synchronous behavior is observed, and slight intermittency appears. Tiwari et al. [61] observed similar behavior at $Re_s = 350$ and attributed such intermittent phenomenon to the imbalance between the pressure and the shear forces on the sphere. In the present study, this intermittent behavior may be also due to the strong interaction between the wake flow and the pipe wall. The intermittency can also indicate the generation of the secondary vortical structures as shown in Figure 6. For $BR = 0.8$, the diagram shows chaotic behavior again and the flow characteristics are totally different from other cases. The fluctuation amplitudes of the forces are extremely large. A possible explanation for this will be that the interaction between the shear layer in the fringe of the wake flow and the wall boundary layer becomes strong and more small-scale flow structures are induced for $BR = 0.8$ as seen in Figure 6 (f). When the induced near-wall flow structures enter the wake flow behind the sphere, the wake flow becomes chaotic. Furthermore, the jet flow coming out of the gap between the sphere and pipe wall is strong. The corresponding value of Re_g, can be much larger than that for $BR \leq 0.6$ as seen in Table 2, which further leads to the chaotic behavior of the wake flow behind the sphere for $BR \geq 0.8$. Furthermore, the overall envelop of the diagram indicates that there is a positive correlation between the total lift and drag forces, which is more apparent for $BR = 0.9$ as shown in Figure 17 compared with that for $BR = 0.8$. This positive correlation has also been reported for the flow past a plate in Tian et al.[60]. As shown in Figure 16, for $BR = 0.4 \sim 0.7$, the lateral force C_n is close to zero. Although at a low Reynolds number $Re_s = 500$, the shear layer instability can be still induced. According to Tiwari et al. [61], this instability generates strong radial motions which can result in the high amplitude fluctuation of C_n normal to the symmetry plane as shown in Figure 16 for $BR = 0.8$ and in Figure 17 for $BR = 0.9$.

Figure 15 Phase diagram (C_d, C_l) for the sphere at $Re_s = 500$

Figure 16 Phase diagram (C_n, C_l) for the sphere at $Re_s = 500$

Figure 17 Phase diagram (a) (C_d, C_l) and (b) (C_n, C_l) for the sphere at $Re_s = 500$ for $BR = 0.9$

Figure 18 shows the time histories of instantaneous C_d for $BR = 0.4{\sim}0.9$ at $Re_g = 500$. The value of C_d is defined based on the characteristic velocity of U_g. It can be seen that for $BR = 0.4$, the variations of C_d with the nondimensional tU_g/d display chaotic behavior, which is also shown in the phase diagrams of (C_d, C_l) in Figures 19. For $BR = 0.5$, the variation of C_d show quasiperiodic behavior with different amplitudes and the phase diagram of (C_d, C_l) show intermittency. The hydrodynamic behaviors for $BR = 0.5$ are also similar to those observed at $Re_s = 500$ as reported in Tiwari et al.[61]. For $BR = 0.6$ and 0.7, the time variations of C_d display periodic wave-like behaviors with a single frequency corresponding to vortex shedding and the synchronous behaviors are observed in the phase diagrams of (C_d, C_l). For $BR = 0.8$ and 0.9, the variations of C_d are steady.

Figure 18 The time histories of C_d for (a) $BR = 0.4$; (b) $BR = 0.6$; (c) $BR = 0.6$; (d) $BR = 0.7$; (e) $BR = 0.8$

Figure 19 Phase diagram (C_d, C_l) for the sphere at $Re_g = 500$

3.3 Power spectra analysis

In this section, power spectra analysis of the velocities sampled at different locations in the wake region is carried out to study the large-scale vortex shedding, KH instabilities of the shear layer as well as the modulation of the wake region. According to Tiwari et al.[61], the time spans of the samplings for all cases correspond to at least 30 vortex shedding cycles in order to capture the low frequency events. All the spectra are obtained using Welch's method (Welch[64]) combined with Hanning window and are averaged along the azimuthal direction at each streamwise location.

At the fixed $Re_p = 1250$, both Re_s and BR can influence the frequency spectra of the velocities. For $BR = 0.2$, the instantaneous streamwise, radial velocity signals are obtained at the locations of $(x/d, r/d) = (1,0.6), (2.4,0.6), (3,0.6), (5,0.6)$ and $(1,0.5)$, which are the same as those used in Rodríguez et al.[43]. First, it is obviously seen from Figure 20 that the velocity spectra at all the monitoring locations show dominant peaks at $St_{\mathrm{VS}} = f_{\mathrm{VS}} d/U_s = 0.14$, which is associated with the large-scale vortex shedding. Here, f_{VS} is the frequency of the large-scale vortex shedding. For these detection points, the peak is strongest at $(x/d, r/d) = (2.4,0.6)$ and decrease downstream the wake region. In addition, an obvious second peak appears at $2St_{\mathrm{VS}}$ indicating a second harmonic for the three velocities at $x/d = 2.4{\sim}5$. Different from what has been observed in Tiwari et al.[61] at the same Re_s, the low frequency of the wake modulation is not apparent in the frequency spectra except for the radial velocity at $(x/d, r/d) = (1,0.5)$. At this location, there is a broadband distribution around $St_{\mathrm{m}}=0.03\sim0.051$ and this value is close to that was reported as $St_{\mathrm{m}}=0.053$ in Tiwari et al. [61] at the same Re_s.

Figure 20 The spectra of the (a) radial velocity; (b) azimuthal velocity and (c) streamwise velocity for $BR=0.2$ at $Re_s=490$. (black solid: $(x/d,r/d)=(1{,}0.6)$; blue: $(x/d,r/d)=(2.4{,}0.6)$; red: $(x/d,r/d)=(3{,}0.6)$; green: $(x/d,r/d)=(5{,}0.6)$; black dashed: $(x/d,r/d)=(1{,}0.5)$)

For $BR=0.4$ at $Re_s=920$, Figure 21 shows that the large-scale vortex shedding takes place at $St_{\mathrm{VS}}=0.22$ observed in the three velocity components at all detection points. There exists a secondary higher spectrum peak with a broadband distribution around $St_{\mathrm{KH}}=0.3\sim0.34$ in the radial velocities which is associated with the shear layer KH instability occurring at $Re_s>800$. However, this secondary peak is not obvious in the streamwise and azimuthal velocities. Furthermore, the low frequency of wake region modulation is apparently observed in the streamwise and azimuthal velocities at $St_{\mathrm{m}}=0.053$. A comparison between the dominant frequencies in the present study with those reported in the previous studies at the similar Re_s is shown in Table 6. It can be seen that the values of St_{VS} and St_{KH} are close to the previous results reported by Tiwari et al. [61] and Sakamoto and Haniu[45] while the present predicted St_{m} is lower than that in Tiwari et al. [61], which may due to the influence of mean shear of the incoming flow in the radial direction. For $BR=0.5$ at $Re_s=1093.8$, as seen in the flow structures in Figure 5, more small-scale structures are induced in the downstream region and the interactions between the near-wake region and the pipe wall are getting stronger. Therefore, the frequency spectra in Figure 22 around the peak frequency St_{VS} and St_{KH} tend to be broadband. The vortex shedding $St_{\mathrm{VS}}\approx0.25$ is apparently detected in all velocity components and the frequency spectra of the radial velocity clearly show the KH instability at $St_{\mathrm{KH}}\approx0.36\sim0.43$. The streamwise velocity frequency spectrum shows a peak around $St_{\mathrm{m}}=0.055$ at $(x/d,r/d)=(1{,}0.5)$. It can be seen that the values of St_{VS} and St_{KH} are both slightly larger than those reported in the previous studies listed in Table 6 at $Re_s=1000$, which may be due to the strong fluctuations induced by the combination effects of pipe wall and the acceleration of the flow past the sphere caused by its blockage on the pipe flow. However, the present predicted value of St_{m} is lower than that of the previous study. This may be due to the confinement of the pipe wall to the shrinkage of the wake region.

Figure 21 The spectra of the (a) radial velocity; (b) azimuthal velocity and (c) streamwise velocity for $BR=0.4$ at $Re_s=920$. (black solid: $(x/d,r/d)=(1{,}0.6)$; blue: $(x/d,r/d)=(2.4{,}0.6)$; red: $(x/d,r/d)=(3{,}0.6)$; green: $(x/d,r/d)=(5{,}0.6)$; black dashed: $(x/d,r/d)=(1{,}0.5)$)

Physics of Fluids ACCEPTED MANUSCRIPT

Figure 22 The spectra of the (a) radial velocity; (b) azimuthal velocity and (c) streamwise velocity for $BR = 0.5$ at $Re_s = 1093.8$. (black solid: $(x/d, r/d) = (1{,}0.6)$; blue: $(x/d, r/d) = (2.4{,}0.6)$; red: $(x/d, r/d) = (3{,}0.6)$; green: $(x/d, r/d) = (5{,}0.6)$; black dashed: $(x/d, r/d) = (1{,}0.5)$)

Table 6. Comparison of the dominant St values with the literatures

Case	Re_s	St_{VS}	St_{KH}	St_{m}
Present $BR = 0.4$	920	0.22	0.3~0.34	0.053
Present $BR = 0.5$	1093.8	0.25	0.38~0.4	0.053
Tiwari et al.[61] /Num.	1000	0.192~0.2	0.3	0.095
Poon et al.[40] /Num.	1000	0.2	0.34	-
Sakamoto and Haniu[45] /Exp.	1000	0.21	0.34	-

For $BR = 0.6$ at $Re_s = 1230$, the frequency spectra in Figure 23 show multiple peaks. The dominant peak of $St_{\mathrm{VS}} = 0.32$ are clearly shown in the radial and azimuthal velocities and amplitude of the KH instability at $St_{\mathrm{KH}} = 0.43\sim0.46$ are much stronger than that of St_{VS} as shown in the two velocity components. Another obvious characteristic is that the frequency spectra of the streamwise velocity show peaks around low $St_{\mathrm{m}} = 0.06\sim0.072$. For $BR = 0.7$ at $Re_s = 1321$, as seen in Figure 24, the flow in the wake region becomes more complex and the large-scale vortex shedding becomes indiscernible. The dominant frequencies associated with the vortex shedding and KH instability are connected to form a broadband distribution covering $St = 0.6\sim1.0$. The spectra show peak at a low frequency of $St_{\mathrm{m}} = 0.12$ especially for the azimuthal velocity.

Figure 23 The spectra of the (a) radial velocity; (b) azimuthal velocity and (c) streamwise velocity for $BR = 0.6$ at $Re_s = 1230$. (black solid: $(x/d, r/d) = (1{,}0.6)$; blue: $(x/d, r/d) = (2.4{,}0.6)$; red: $(x/d, r/d) = (3{,}0.6)$; green: $(x/d, r/d) = (5{,}0.6)$; black dashed: $(x/d, r/d) = (1{,}0.5)$)

Figure 24 The spectra of the (a) radial velocity; (b) azimuthal velocity and (c) streamwise velocity for $BR = 0.7$ at $Re_s = 1321$. (black solid: $(x/d, r/d) = (1{,}0.6)$; blue: $(x/d, r/d) = (2.4{,}0.6)$; red: $(x/d, r/d) = (3{,}0.6)$; green: $(x/d, r/d) = (5{,}0.6)$; black dashed: $(x/d, r/d) = (1{,}0.5)$)

For $BR = 0.8$ at $Re_s = 1360$ and $BR = 0.9$ at $Re_s = 1338.75$, different behaviors of frequency spectra from other cases are shown in Figures 25 and 26, where there is no large-scale vortex shedding mode and apparent low-frequency wake modulation mode compared with those for

Physics of Fluids ACCEPTED MANUSCRIPT
This is the author's peer reviewed, accepted manuscript. However, the online version of record will be different from this version once it has been copyedited and typeset.
PLEASE CITE THIS ARTICLE AS DOI:10.1063/5.0017349
AIP Publishing

$BR \leq 0.6$. For $BR = 0.8$, the spectra show only one peak around $St \approx 1.5$ at $x/d = 1$ for the radial and streamwise velocities. For $BR = 0.9$, the frequency spectra of the radial and streamwise velocities show broadband distributions within $St \approx 2 \sim 5$, which indicates small-scale flow structures with a wide range of small time scales. This peak frequency for the two high BR is higher than the secondary shear layer instability frequency even at higher Re_s than the present study, such as $St_{\mathrm{KH}} = 0.72$ at $Re_s = 3700$ in Rodríguez et al.[43]. This mode may be due to the strong and complex interactions between the shear layer of the wake region and the pipe wall boundary layer. Furthermore, there seems to be low-frequency wake modulation modes observed in the frequency spectra of radial and streamwise velocities. However, the frequencies $St_{\mathrm{m}} \approx 0.18$ for $BR = 0.8$ and $St_{\mathrm{m}} \approx 0.4 \sim 0.7$ for $BR = 0.9$ are much higher than that for other BR.

Figure 25 The spectra of the (a) radial velocity; (b) azimuthal velocity and (c) streamwise velocity for $BR = 0.8$ at $Re_s = 1360$. (black solid: $(x/d, r/d) = (1,0.6)$; blue: $(x/d, r/d) = (2.4,0.6)$; red: $(x/d, r/d) = (3,0.6)$; green: $(x/d, r/d) = (5,0.6)$; black dashed: $(x/d, r/d) = (1,0.5)$)

Figure 26 The spectra of the (a) radial velocity; (b) azimuthal velocity and (c) streamwise velocity for $BR = 0.9$ at $Re_s = 1338.75$. (black solid: $(x/d, r/d) = (1,0.6)$; blue: $(x/d, r/d) = (2.4,0.6)$; red: $(x/d, r/d) = (3,0.6)$; green: $(x/d, r/d) = (5,0.6)$; black dashed: $(x/d, r/d) = (1,0.5)$)

The frequency spectra at the detection points of $x/d = 0.2 \sim 2$ for $BR = 0.4 \sim 0.7$ at $Re_s = 500$ are presented in Figure 27 for the radial velocity. It can be seen that due to the low Re_s, there is only one single dominant frequency peak corresponding to the regular large-scale vortex shedding. The other peaks are their second and third harmonic as $2St_{\mathrm{VS}}$, $3St_{\mathrm{VS}}\ldots$. In addition, Figure 27 shows that St_{VS} increases with the increasing BR. This may be due to the increasing mean streamwise velocity with the increasing blockage effect of the sphere and the spectra around the vortex shedding frequency tend to be more broadband with the increasing BR. However, for $BR = 0.8$, the frequency spectra are quite different as shown in Figure 28 for the three velocity components. Multiple frequency peaks with a broadband distribution are shown and high level of fluctuations are located around $x/d = 2 \sim 4$. A dominant vortex shedding $St_{\mathrm{VS}} \approx 0.47$ is observed and the frequency is much larger than that for $BR < 0.8$. Even at this low Re_s, there is still dominant KH instability mode, which is obviously seen in the radial and streamwise velocities spectra at $St_{\mathrm{KH}} \approx 0.71$. Furthermore, there is a low frequency mode at $St_{\mathrm{m}} \approx 0.157$ as seen in the streamwise velocity spectra which cannot be observed in the frequency spectra for lower BR. This low frequency can exist far downstream indicating that the low frequency mode is related to the modulation of the whole wake region. For $BR = 0.9$, there is no obvious vortex shedding mode in the frequency spectra of all the three velocities as shown in Figure 29. Broadband distributions are shown in the frequency spectra of the radial and streamwise velocities within $St \approx 1$ around $x/d \approx 1.5$. The low-frequency wake modulation mode at $St_{\mathrm{m}} \approx 0.2$ is also observed in the frequency spectra of the radial and azimuthal velocities. Furthermore, the low-frequency peak with high amplitudes in the frequency spectra of the streamwise velocity indicates the transition to turbulence.

Figure 27 The spectra of the radial velocities at the streamwise locations of $x/d = 0.2{\sim}2$ spaced by $x/d = 0.2$ for $BR = 0.4$ (red); 0.5 (blue); 0.6 (green); 0.7 (black) at $Re_s = 500$

Figure 28 The spectra of the (a) radial velocity; (b) azimuthal velocity and (c) streamwise velocity for $BR = 0.8$ at $Re_s = 500$ at the streamwise locations of $x/d = 0.2{\sim}5$ spaced by $x/d = 0.2$

Figure 29 The spectra of the (a) radial velocity; (b) azimuthal velocity and (c) streamwise velocity for $BR = 0.9$ at $Re_s = 500$ at the streamwise locations of $x/d = 0.2{\sim}5$ spaced by $x/d = 0.2$

The frequency spectra at the detection points of $x/d = 0.2{\sim}2$ for $BR = 0.4{\sim}0.7$ at $Re_g = 500$ are presented in Figure 30 for the radial velocity. Different variations of the frequency spectra with the increasing BR are shown compared with those at $Re_s = 500$. For $BR = 0.4$ and 0.5, in addition to the large-scale vortex shedding frequency St_{VS}, the frequency peaks corresponding to the KH instability mode at St_{KH} and the low-frequency wake modulation mode at St_{m} are shown. For $BR = 0.6$ and 0.7, only one single dominant frequency peak corresponding to the regular large-scale vortex shedding is shown together with their second and third harmonic as $2St_{\mathrm{VS}}$, $3St_{\mathrm{VS}}$…. Figure 30 shows a decreasing St_{VS} with the increasing BR. This may due to the reason that with the increasing BR, the kinematic viscosity increases to keep the same Re_g and the flow tends to be stabilized, which is also shown in the wake vortical structures in Figure 8.

Figure 30 The spectra of the radial velocities at the streamwise locations of $x/d = 0.2{\sim}2$ spaced by $x/d = 0.2$ for $BR = 0.4$ (red); 0.5 (blue); 0.6 (green); 0.7 (black) at $Re_g = 500$

3.4 Dynamic Mode Decomposition analysis of the wake flow

In order to gain a better understand of the coherent structures associated with the dominant frequency obtained at different points in Section 3.2, the spatial shapes of these modes are revealed by using the data-drive Dynamic Mode Decomposition (DMD) method proposed by Schmid[47] in

Physics of Fluids ACCEPTED MANUSCRIPT

this section. The method is able to develop a reduced order representation of snapshots from a dynamical system and provide temporal information and the spatial structures of the dominant modes used to build the reduced order model as

$$u(x,y,z) \approx \sum_{i=1}^{N} a_i \phi_i(x,y,z) \exp(\lambda_i t) \tag{8}$$

where ϕ_i is the spatial mode with their amplitude a_i and λ_i is the complex frequency of each mode (Re(λ_i) is the temporal growth and Im(λ_i) is the frequency).

In the present study, the modes which make the most contributions to the dynamical system of the wake flow are extracted by applying sparsity promote algorithm on the DMD (SPDMD) modes obtained by using the original DMD method. The idea of the algorithm is to achieve a balance between the approximation error in Eq. (8) and the number of the extracted modes by solving a convex optimization problem. This algorithm has been invented by Jovanović et al.[17] and widely used in the studies of coherent structures in Statnikov et al.[55], Loosen et al.[27], Wu et al.[68] and Yu et al.[70]. Furthermore, in order to reduce the memory of matrices decompositions in DMD analysis of 3D flow data, the sparsity-promoted algorithm is further combined with the on-the-fly incremental Singular Value Decomposition (SVD) algorithm used in Ohmichi[38], Matsumoto and Indinger[31] and Oxberry et al.[39]. The detailed information of these algorithms can be found in abovementioned studies and is not presented here. The flow data of $BR = 0.4$ at $Re_s = 920$, $BR = 0.6$ at $Re_s = 1230$ and $BR = 0.8$ at $Re_s = 1360$ is analyzed here. An example of how SPDMD is applied for $BR = 0.8$ is present in Appendix B.

For $BR = 0.4$ at $Re_s = 920$, the 3D flow snapshots are sampled over a time span of 33 vortex shedding cycles, which is also consistent with the least number that is able to capture the low frequency events as reported in Tiwari et al. [61]. The time interval between the snapshots is set to be $\Delta t U_s/d = 0.46$, which corresponds to a sampling frequency 5 times of the highest dominant mode of KH instability and satisfies Nyquist criterion as mentioned in Schmid[47]. For $BR = 0.6$ at $Re_s = 1230$, 3D flow snapshots are sampled over a time span of 50 vortex shedding cycles with the time interval between the snapshots of $\Delta t U_s/d = 0.55$, which also satisfies Nyquist criterion. For $BR = 0.8$ at $Re_s = 1360$, there is no vortex shedding and the 3D flow snapshots are sampled over a time span of approximate 10 low frequency events with $St_{\mathrm{m}} \approx 0.18$ as shown in Figure 25 (c) and the time interval between the snapshots is set to be $\Delta t U_s/d = 0.17$, which can capture the instability mode with the high frequency in Figure 25. Therefore, the parameters of the DMD method used here can fulfill the requirement of capturing the dominant modes.

Figure 31 displays the frequency spectrum of the DMD modes obtained by using the original DMD method and by applying sparsity-promoted algorithm for $BR = 0.4$, 0.6 and 0.8. Only the modes with $\mathrm{Im}(\lambda_i) \geq 0$ are shown. It can be seen that after the sparsity-promoted algorithm is applied, a large part of the original modes is removed due to their low contribution to the dynamical systems. Therefore, the analysis should focus on the remaining modes after applying the sparsity-promoted algorithm. Modes with $St = 0$ denote the time-averaged flow. It is obvious that for $BR = 0.4$ and 0.6, the remaining fluctuation modes for the two cases cluster around three peaks which roughly correspond to the three dominant modes as shown in comparison with the frequency spectra in the figures. The slight difference between the frequency analysis and the DMD method may be due to the fact that the coherency among the three velocity components are considered in the DMD method while the power spectra analysis is performed for each velocity component respectively. For $BR = 0.8$, because the wake flow is chaotic and looks similar to fully developed turbulent flow, the streamwise and radial velocity spectra display broadband distribution around the low frequency range. After applying the sparsity-promoted algorithm, the remaining DMD modes seem to be continuous distributed. However, the clustering of these DMD modes can still be observed. and the dominant KH instability mode in the two velocity components can be captured by the DMD modes. Furthermore, there is an additional modes cluster around $St \approx 0.6 \sim 0.9$. According to Schmid[47], the cluster of modes are associated with the advection and diffusion of the flow structures and the modes on one cluster usually have similar wavelength in the streamwise direction. Therefore, these modes are not related to the large-scale hairpin vortices and may correspond to the small-scale flow structures that are periodically shedding and traveling downstream. The low-frequency mode is also captured by the DMD mode of $St_{\mathrm{m}} \approx 0.18$.

Figure 31 The frequency spectra of the DMD modes for (a) $BR = 0.4$; (b) 0.6 and (c) 0.8 with the dominant modes denoted by the arrows (Blue circles: the modes obtained by using the original DMD method; red crossings: the modes obtained by applying sparsity-promoted algorithm)

The radial and streamwise velocities for the three fluctuation modes are shown in Figures 32~34. It is observed that for $BR = 0.4$ and 0.6, both the vortex shedding mode and the KH instability mode display wave-packet form and the St values of the modes are related to their streamwise spatial length scale, which is consistent with what have been reported in Nidhan et al.[36]. The streamwise length scale of KH mode is smaller than that of the vortex shedding mode especially for the streamwise velocity with $BR = 0.4$. Furthermore, different from the modes obtained in the wake flow behind a sphere and a cylinder placed in an infinitely large domain in Stankiewicz et al.[54], Nidhan et al.[36] and Ohmichi[38], the structures in the downstream region are stretched in the streamwise direction due to the interactions with the pipe boundary layer especially for $BR = 0.6$. For the low frequency modes, they display streamwise elongated structures and more energy is contained in the streamwise velocity compared with the radial velocity. This is consistent with the frequency analysis in Section 3.3 where the low frequency mode is more apparent in the streamwise velocity components. In addition, the structures of the low frequency modes near the sphere are located closer to the center of the wake flow compared with other two modes and they are strongly coherent with the downstream long streamwise structures near the pipe wall. For $BR = 0.8$, two example modes in the cluster around $St \approx 0.6 \sim 0.9$ with $St_{\mathrm{DMD}} = 0.74$ and $St_{\mathrm{DMD}} = 0.835$ respectively are shown in Figure 34. Both the radial and streamwise velocity modes of the two modes display a form of oblique waves oriented in different directions. Their length scale is much smaller than that of the vortex shedding modes of $BR = 0.4$ and 0.6. Due to the turbulence in the further downstream region, the DMD modes in the region are smaller and more chaotic than the other two BRs. The radial velocity of the low frequency mode is also weak and compared with this

Physics of Fluids ACCEPTED MANUSCRIPT

This is the author's peer reviewed, accepted manuscript. However, the online version of record will be different from this version once it has been copyedited and typeset.
PLEASE CITE THIS ARTICLE AS DOI:10.1063/5.0017349

AIP Publishing

mode for $BR = 0.4$ and 0.6, the coherency with the flow structures near the pipe wall is closer to the sphere.

Figure 32 Iso-surfaces of $u_r/U_m = \pm 0.0002$ for the radial velocity (a, c, e) and $u/U_m = \pm 0.0005$ for the streamwise velocity (b, d, f) of the three dominant DMD modes of $BR = 0.4$: (a, b) vortex shedding mode; (c, d) KH instability mode; (e, f) low-frequency mode

Figure 33 Iso-surfaces of $u_r/U_m = \pm 0.0002$ for the radial velocity (a, c, e) and $u/U_m = \pm 0.0005$ for the streamwise velocity (b, d, f) of the three dominant DMD modes of $BR = 0.6$: (a, b) vortex shedding mode; (c, d) KH instability mode; (e, f) low-frequency mode

Figure 34 Iso-surfaces of $u_r/U_m = \pm 0.0002$ for the radial velocity (a, c, e, g) and $u/U_m = \pm 0.0005$ for the streamwise velocity (b, d, f, h) of the four dominant DMD modes of $BR = 0.8$: (a, b) DMD modes at $St_{\mathrm{DMD}} = 0.74$; (c, d) DMD modes at $St_{\mathrm{DMD}} = 0.835$; (e, f) KH instability mode; (g, h) low-frequency mode

In order to show the dynamical contribution of the low frequency mode to the flow, the streamwise velocity of the mean flow with the superposition of the low frequency mode at eight instants on the XY slice are shown in Figure 35. The slow modulation of the wake flow can be observed in the deformation of the recirculation region (denoted as '1'). Furthermore, the shear layer in the fringe of the recirculation region display periodic elongated and shrinkage motions (denoted as '2'). The downstream wake flow is flapping (denoted as '3'). However, the flapping motions are confined by the pipe wall.

Figure 35 The streamwise velocity of the mean flow with the superposition of the low frequency DMD mode at eight instants on the XY slice at (a) $tU_\infty/d = 579.47$; (b) $tU_\infty/d = 582.2$; (c) $tU_\infty/d = 584.93$; (d) $tU_\infty/d = 587.66$; (e) $tU_\infty/d = 590.39$; (f) $tU_\infty/d = 593.12$; (g) $tU_\infty/d = 595.85$; (h) $tU_\infty/d = 595.58$

Physics of Fluids ACCEPTED MANUSCRIPT

AIP Publishing

This is the author's peer reviewed, accepted manuscript. However, the online version of record will be different from this version once it has been copyedited and typeset.
PLEASE CITE THIS ARTICLE AS DOI:10.1063/5.0017349

3. Conclusion

In the present study, three series of numerical simulations of three-dimensional flow past a stationary sphere with the diameter of $d = 0.1D{\sim}0.9D$ are performed. The first series of simulations is based on a fixed $Re_p = 1250$ and Re_s varying between $249 \leq Re_s \leq 1360$. The second series of simulations is based on a fixed $Re_s = 500$ and Re_p varying between $460 \leq Re_p \leq 678$. The third series of simulations is based on a fixed $Re_g = 500$ and Re_p varying between $113 \leq Re_p \leq 773$. Grid resolution studies have been performed for each BR to determine sufficient grid resolutions at $Re_p = 1250$. Simulations of uniform flow past a sphere in an infinitely large domain are carried out to validate the present numerical model by comparing their hydrodynamic quantities with the published studies at $Re_s = 250{\sim}400$. The hydrodynamic characteristics such as the drag and lift coefficients and the pressure coefficients on the sphere, the vortex-shedding frequencies, the time-averaged streamlines and the centerline time-averaged velocity profile agree reasonably with the published data. Then various physical phenomena on the instantaneous wake vortical structures, power spectra of the velocities are discussed for $BR = 0.2, 0.4, 0.5, 0.6, 0.7, 0.8$ and 0.9. The main conclusions can be summarized as follows:

1. The vortical structures in the wake flow behind the sphere display different characteristics with the increasing BR. At $Re_p = 1250$, for the smallest $BR = 0.1$, the wake flow is steady and asymmetric with two streamwise vortices. For $BR = 0.2{\sim}0.7$, there is large-scale vortex shedding. However, due to the interaction of the wake flow and the pipe flow boundary layer, induced secondary vortices are generated around the primary hairpin vortices. With the increasing BR, the secondary vortices become vortex rings around the wake region. For $BR \geq 0.4$ at $Re_s > 900$, there are time instants when multiple hairpin vortices shedding simultaneously and are entangled together. When the disturbances enter the pipe wall boundary layer, small-scale streamwise vortical ribs are formed downstream near the pipe wall. For large $BR = 0.8$ and 0.9, the large-scale shedding hairpin vortices disappear, and strong chaotic small-scale vortical structures are generated. For $BR = 0.4{\sim}0.7$ at $Re_s = 500$, regular large-scale planar-symmetric hairpin vortices with a similar shape are shedding from the sphere compared with $BR = 0.2$ due to the stabilization of the pipe wall. However, for $BR = 0.8$, the vortex shedding still exists while the vortices are chaotic, and the planar symmetry disappears. For $BR = 0.9$, the vortex shedding is suppressed. At $Re_g = 500$, with the increasing BR, a gradually stabilized wake flow is observed.
2. The hydrodynamic quantities of the sphere such as drag coefficients C_d and the lateral force coefficients C_l, C_n parallel to and normal to the symmetry plane for different BRs at the same Re_s and Re_g are investigated. At $Re_s = 500$, for $BR = 0.4{\sim}0.7$, due to the effects of BR and the mean shear of the incoming flow, a regular periodicity is observed for the time histories of C_d and a synchronous behavior is observed for the phase diagram of (C_d, C_l) and the values of C_n for these cases are close to zero. For $BR = 0.7$, a slight intermittency begins to appear for (C_d, C_l) and the amplitudes of C_d and C_l are also increasing. For $BR = 0.8$ and 0.9, the phase diagrams of the forces appear to be strongly chaotic and a positive correlation is observed between C_d and C_l. At $Re_g = 500$, for $BR = 0.4$, the time histories of instantaneous C_d display chaotic behavior. For $BR = 0.5$, the variation of C_d shows intermittency. For $BR = 0.6$ and 0.7, the time variations of C_d display periodic wave-like behaviors and the synchronous behaviors are observed in the phase diagrams of (C_d, C_l). For $BR = 0.8$ and 0.9,

Physics of Fluids ACCEPTED MANUSCRIPT

steady behaviors are observed for the hydrodynamic quantities.

3. The power spectra analysis is performed for the velocity signals at different locations in the wake region. For $BR = 0.2{\sim}0.7$, the large-scale vortex shedding frequency is detected, and their values are in good agreement with the data reported in the previous studies at the similar Re_s. For $BR \geq 0.4$ at $Re_s > 800$, the KH instability mode is also observed with a broadband distribution in the radial velocity. For $BR = 0.8$ and 0.9, the vortex shedding frequency disappears, and an instability mode is captured with a higher frequency than that associated with the KH instability. In addition, a low frequency wake modulation mode is observed in these cases. For $BR < 0.8$ at $Re_s = 500$, only vortex shedding frequency is detected in the wake region and the frequency value increases with the increasing BR. This may be due to acceleration of the flow because of the blockage effect of the sphere to the pipe flow. For $BR = 0.8$ and 0.9, both the strong KH instability mode and the wake modulation mode are observed. The vortex shedding frequency disappears for $BR = 0.9$ at $Re_s = 500$. At $Re_g = 500$, the vortex shedding mode, the KH instability mode and the low-frequency mode are displayed for $BR = 0.4$ and 0.5 while only vortex shedding frequency appears for $BR = 0.6$ and 0.7. The stabilization of the wake flow is also observed with the increasing BR at this Reynolds number.
4. In order to further investigate the coherent structures in the wake region, a data-driven method, Dynamic Mode Decomposition (DMD) is used to analyze the flow data for $BR = 0.4, 0.6$ and 0.8 at $Re_p = 1250$ and a sparsity-promoted algorithm is applied to extract the dominant modes. All of the important modes associated with the vortex-shedding, KH instability as well as the wake modulation can be captured by the sparsity-promoted DMD. The vortex shedding mode and the KH instability mode display wave-packet form traveling downstream. The wake modulation mode is more obvious in the streamwise velocity and shows that the modulation of the wake region is also coherent with the downstream flow structures near the pipe wall. Furthermore, from the effect of the low-frequency wake modulation mode on the time-averaged flow, the slow deformation motions of the wake region and the flapping of the downstream flow are observed.

Physics of Fluids ACCEPTED MANUSCRIPT

Appendix A

Convergence studies

The time-averaged drag coefficient $\overline{C_d}$ and the time-averaged recirculation length L_w behind the sphere obtained by using different meshes numbers are shown in Table 7. The value of $\overline{C_d}$ is calculated using Eq. (3). All the cases are run for at least 20 vortex shedding cycles to obtain time-averaged values. The Courant–Friedrichs–Lewy (CFL) numbers for all cases are kept below 0.4 to ensure the stability of the simulations. For each BR, the relative differences of $\overline{C_d}$ between different meshes are all below 1%. For L_w, the relative differences between different meshes for $BR < 0.7$ are below 1%. For $BR = 0.7$, 0.8 and 0.9, due to the fluctuation of the separation bubbles, there is variance in the value of L_w between different meshes. However, for the two finest meshes of the two BRs, the relative differences lower than 5% of L_w can be achieved. Further comparisons are made for the azimuthal- and time-averaged streamwise velocity $\bar{u}$ at six different streamwise locations at $x/d = 0.2, 1, 2, 3, 4, 5$ behind the sphere for each BR as shown in Figure 36. For each BR, the velocity profiles for the two finest meshes agree well with each other. Therefore, it can be seen that sufficient grid resolutions have been achieved for Cases A4, B3, C3, D3, E3, F3, G4 and H3 and all the results presented in following sections are obtained based on these cases. A time-step sensitivity study has been done with a CFL number below 0.2 for $BR = 0.2$ using Case B3. Both the relative differences of $\overline{C_d}$ and L_w are below 1%. Finally, based on Tiwari et al. [61], a time span of at least 30 vortex shedding cycles are then simulated for each BR to capture the low modulation frequency of St_{m} in the present study.

Similar to what were done in Rodríguez et al.[44] and Tiwari et al. [61], the quality of the meshes can be further checked in a posteriori analysis based on the ratio between the grid size h and Kolmogorov length scale η (where h is defined as $\sqrt[3]{\Delta x \Delta y \Delta z}$ of each cell). The value of η is calculated as $\eta = (\nu^3/\varepsilon)^{1/4}$ even though the flow is not fully developed turbulent flow. The averaged ratios for the finest meshes in Table 7 for $BR > 0.4$ in the wake region of $0 < x/d < 5$ are presented in Table 8 and the grid size of $h \sim O(\eta)$ can be achieved for each case. It is noted that the averaged value of h/η is 0.91 for the grid in the wake region in Rodríguez et al. [44]. The value of h/η is 0.177 for the grid of the first layer near the sphere surface in Tiwari et al. [61] and this value for the present study is approximately 0.03~0.1 near the sphere surface and the pipe wall. Also, it is worth mentioning that according to Pope[42], the dissipation length scales are in the range of $8 < h/\eta < 60$ with the dissipation peak at $h/\eta \sim 24$ and the grid size in the present study should fulfill the requirement to capture the dissipation spectrum. Therefore, based on these considerations, it can be concluded that the present simulations can provide satisfactory spatial resolutions for each BR.

Table 7 Results for grid resolution studies

BR	Cases	No. of cells (million)	N_{plane}	N_{BL}	$\overline{C_d}$	L_w
0.1	A1	0.84	80	5	0.6969	1.791
	A2	1.2	80	9	0.6932	1.782
	A3	1.9	100	11	0.6917	1.787
	A4	3	100	11	0.6910	1.798
0.2	B1	0.83	80	9	0.5204	1.73
	B2	1.2	80	11	0.5189	1.78
	B3	2.3	100	11	0.5192	1.81
0.4	C1	1.1	80	9	0.4140	1.71
	C2	2.1	80	12	0.4126	1.77
	C3	3.0	100	12	0.4131	1.77
0.5	D1	1.0	80	9	0.4294	1.64
	D2	1.8	80	12	0.4311	1.65
	D3	3	100	12	0.4303	1.67
0.6	E1	0.89	80	9	0.5331	1.62
	E2	1.8	80	12	0.5342	1.66
	E3	2.5	100	12	0.5341	1.66
0.7	F1	8.7	80	9	0.8592	1.38
	F2	1.9	80	12	0.8673	1.42
	F3	3.0	100	12	0.8687	1.42
0.8	G1	0.78	80	9	2.02	1.27
	G2	1.5	80	12	2.0097	1.33
	G3	2.2	100	12	2.0086	1.30
	G4	3.3	120	12	2.006	1.34
0.9	H1	0.65	80	9	8.937	1.31
	H2	1.2	100	12	8.89	1.28
	H3	2.8	120	12	8.86	1.34

Figure 36 Azimuthal- and time-averaged streamwise profiles at the streamwise locations of $x/d = 0.2, 1, 2, 3, 4, 5$ in the wake flow behind the sphere for different grid resolutions: Case 1: Solid lines; Case 2: Dashed; Case 3: Dash-dotted; Case 4: Black circles with $BR =$ (a) 0.1; (b) 0.2; (c) 0.4; (d) 0.5; (e) 0.6; (f) 0.7; (g) 0.8; (h) 0.9

Table 8 The averaged ratios between the grids size and the Kolmogorov length scale in the wake region for the finest cases in Table 7 with $BR = 0.4{\sim}0.9$

BR	0.4	0.5	0.6	0.7	0.8	0.9
$\bar{h}/\eta$	0.445	0.503	0.667	0.870	1.087	1.7

Physics of Fluids ACCEPTED MANUSCRIPT

This is the author's peer reviewed, accepted manuscript. However, the online version of record will be different from this version once it has been copyedited and typeset.
PLEASE CITE THIS ARTICLE AS DOI:10.1063/5.0017349

AIP Publishing

Influence of the computational domains

The distance between the inlet and the sphere center is set to be $Lu = 5D$ in the present study. This length is larger than $5d$, which is adopted in Rodríguez et al.[43, 44] and Tiwari et al.[61]. Therefore, the length of $Lu = 5D$ can be sufficient even for the two largest $BR = 0.8$ and 0.9. Additional simulations for $BR = 0.8$ and 0.9 at $Re_p = 1250$ have been carried out to investigate the influence of the domain sizes. The same grid resolutions as Cases G3 and H1 in Table 7 are used because sufficiently convergent results in terms of $\overline{C_d}$ can be obtained using the grid resolutions as shown in Table 7. The values of $\overline{C_d}$ for different cases are shown in Table 9. The value of Ld is set to be $20d$ which corresponds to $16D$ and $18D$ for $BR = 0.8$ and 0.9, respectively. It can be seen that when increasing Lu from $5D$ to $10D$ and Ld from $7.5D$ to $20d$, the differences of $\overline{C_d}$ are within 1% and the differences of L_w are within 5%. Furthermore, the centerline time-averaged streamwise velocity profiles of Cases H3 and H3L are shown in Figure 37. It can be seen that the difference in the two profiles within $r < x < 7.5D$ is negligible. As a result, it is suggested that the time-averaged hydrodynamic quantities and wake flow features are independent when further increasing the inlet and outlet lengths in Section 2.2.1 and rest of the present study. The values of $Lu = 5D$ and $Ld = 7.5D$ are sufficient to investigate the hydrodynamic forces on the sphere.

Table 9 Results for the study of the domain sizes influence

BR	Cases	No. of cells (million)	Lu	Ld	$\overline{C_d}$	L_w
0.8	H3	1.9	$5D(6.25d)$	$7.5D(9.38d)$	2.0086	1.30
	H3L	3	$10D(12.5d)$	$16D(20d)$	2.0087	1.297
0.9	G1	0.83	$5D(5.6d)$	$7.5D(8.33d)$	8.937	1.31
	G1L	1.2	$10D(11.1d)$	$18D(20d)$	8.949	1.26

Figure 37 The time-averaged streamwise velocity along the centerline of the pipe (Solid lines: H3; Dashed: H3L)

Physics of Fluids ACCEPTED MANUSCRIPT

This is the author's peer reviewed, accepted manuscript. However, the online version of record will be different from this version once it has been copyedited and typeset.
PLEASE CITE THIS ARTICLE AS DOI:10.1063/5.0017349

AIP Publishing

Appendix B

Sparsity-promoted dynamic mode decomposition

A brief description of the sparsity-promoted dynamic mode decomposition (SPDMD) algorithm proposed in Jovanovic et al. [17] is presented here.

The aim of the algorithm is to select a subset of dynamically important DMD modes that make large contribution to the dynamical evolution of the flow. Given the DMD modes and their eigenvalues obtained by using standard DMD analysis, the reduced order representation of snapshots (8) in Section 3.4 can be reformulated in a matrix form as

$$[\mathbf{u}_1, \mathbf{u}_2, \mathbf{u}_3 \dots, \mathbf{u}_K] = \mathbf{V}_1^N \approx \mathbf{\Phi}\mathbf{D}_\alpha\mathbf{V}_{\mathrm{and}} = [\boldsymbol{\phi}_1, \boldsymbol{\phi}_2, \boldsymbol{\phi}_3 \dots, \boldsymbol{\phi}_N]\begin{bmatrix}\alpha_1 & & \\ & \dots & \\ & & \alpha_N\end{bmatrix}\begin{bmatrix}\mu_1^0 & \cdots & \mu_1^{K-1} \\ \vdots & \ddots & \vdots \\ \mu_N^0 & \cdots & \mu_N^{K-1}\end{bmatrix} \quad \text{(B1)}$$

where $\mathbf{u}_i = [u(x_l, y_m, z_n, t_i)]_{L\times M\times N}$ denote a column vector gathering three velocities components at all spatial grid points $(1 \le l \le L, 1 \le m \le M, 1 \le n \le N)$ in the flow field at the time step of time step of $t = t_i$ $(t_i = i\Delta t, i = 1\sim K)$. In Eq (B1), $\mathbf{D}_\alpha = \mathbf{diag}(\alpha_1, \dots, \alpha_N)$ denote the amplitudes of their corresponding DMD modes within the time span of $T = (K-1)\Delta t$. The amplitude of each DMD mode α_i $(i = 1,2,3 \dots N)$ is regarded as the measurement of its contribution to the dynamic system. $\mathbf{V}_{\mathrm{and}}$ denotes the Vandermonde matrix contained the temporal variations of each mode during the time span. In the sparsity-promoted dynamic mode decomposition algorithm, a penalty function γ is introduced and an optimization problem is solved to determine the unknown amplitudes matrix $\mathbf{D}_\alpha$

$$\min_{\boldsymbol{\alpha}} \|\mathbf{V}_1^N - \mathbf{\Phi}\mathbf{D}_\alpha\mathbf{V}_{\mathbf{and}}\|_F^2 + \gamma\sum_{i=1}^{N}|\alpha_i| \quad \text{(B2)}$$

$\|\dots\|_F$ is the Frobenius norm of a matrix. The positive parameter γ is a user-specified regularization parameter chosen to achieve a balance between the quality of the approximation (B1) and the number of efficient DMD modes N used in the approximation. For a large γ, most of the element in $[\alpha_1, \dots, \alpha_N]$ becomes 0. It means that the SPDMD algorithm removes both the modes which only influence the early stages of the time evolution and decay quickly, and the modes with small amplitudes. As a result, the DMD modes with non-zero elements in $[\alpha_1, \dots, \alpha_N]$ which contribute the most to the dynamical evolution are kept. The convex optimization problem (B2) are solved by using the alternating direction method of multipliers (ADMM, Ghadimi et al.[10]), a state-of-the-art method for solving large-scale and distributed optimization problems according to Jovanović et al. [17].

The SPDMD analysis results are presented in detail here for $BR = 0.8$. Similar results are also obtained for $BR = 0.4$ and 0.6 which are not presented in detail. The approximation loss $\Pi_{\mathrm{loss}} = 100\sqrt{\|\mathbf{V}_1^N - \mathbf{\Phi}\mathbf{D}_\alpha\mathbf{V}_{\mathbf{and}}\|_F^2/\mathbf{V}_1^N}$ for the optimal vector of amplitudes α and the number of modes N retain in the approximation (B1) by applying the sparsity-promoting DMD algorithm are shown in Figure 38 (a) as a function of the user-specified penalty parameter γ. Similar to the results reported in Jovanović et al. [17], with the increasing values of γ, the approximation error increases and the number N decreases. Figure 38 (b) shows how the dynamical important modes are selected in the DMD frequency spectra. It can be seen that the SPDMD algorithm removes the modes with large amplitudes.

Figure 38 (a) The approximation loss Π_{loss} with γ; (b) the number of modes N retain in Eq (B1) with γ

As suggested in Section 3.4, for $BR = 0.8$, the flow is close to turbulent state and the SPDMD method concentrates on some clusters of modes. The modes in each cluster may correspond to similar flow structures. For $N = 57$ in Figure 38 (a), the clusters of modes related the KH instability, the typical modes representing the periodically shedding small-scale flow structures and the low-frequency events as shown in Figure 29 of Section 3.4 are identified. For $N = 13$ in Figure 38 (b), the KH instability modes are removed due to their high frequency and lower contribution to the dynamics compared with the other two types of modes. For $N = 9$ in Figure 38 (c), only the low-frequency mode is kept. It worth mentioning that the finally left modes by using large γ concentrate on extremely low frequencies, which is in consistent with the frequency spectra shown in Figure 26 (c) and may be characteristic of turbulent flow.

Figure 39 The frequency spectra of the DMD modes obtained by using the original standard DMD method (Blue circles) and the SPDMD (red crossings) with different number of modes (a) $N = 57$; (b) $N = 13$; (c) $N = 9$

Authors' contributions
All authors contributed equally to this work.

Acknowledgement
This study was supported with computational resources provided by the Norwegian Metacenter for Computational Science (NOTUR), under Project No: NN9372K.

Data availability
The data that support the findings of this study are available from the corresponding author upon reasonable request.

Physics of Fluids ACCEPTED MANUSCRIPT
This is the author's peer reviewed, accepted manuscript. However, the online version of record will be different from this version once it has been copyedited and typeset.
PLEASE CITE THIS ARTICLE AS DOI:10.1063/5.0017349
AIP Publishing

References

[1] Achenbach, Elmar. "Vortex shedding from spheres." Journal of Fluid Mechanics 62.2 (1974): 209-221.

[2] Bagchi, Prosenjit, M. Y. Ha, and S. Balachandar. "Direct numerical simulation of flow and heat transfer from a sphere in a uniform cross-flow." J. Fluids Eng. 123.2 (2001): 347-358.

[3] Campregher, Rubens, et al. "Computations of the flow past a still sphere at moderate Reynolds numbers using an immersed boundary method." Journal of the Brazilian Society of Mechanical Sciences and Engineering 31.4 (2009): 344-352.

[4] Chomaz, J. M., P. Bonneton, and E. J. Hopfinger. "The structure of the near wake of a sphere moving horizontally in a stratified fluid." Journal of Fluid Mechanics 254 (1993): 1-21.

[5] Clift, Roland, John R. Grace, and Martin E. Weber. Bubbles, drops, and particles. Courier Corporation, 2005.

[6] Constantinescu, George S., and Kyle D. Squires. "LES and DES investigations of turbulent flow over a sphere at Re= 10,000." Flow, Turbulence and Combustion 70.1-4 (2003): 267-298.

[7] Fadlun, E. A., et al. "Combined immersed-boundary finite-difference methods for three-dimensional complex flow simulations." Journal of computational physics 161.1 (2000): 35-60.

[8] Fayon, A. M., and John Happel. "Effect of a cylindrical boundary on a fixed rigid sphere in a moving viscous fluid." AIChE journal 6.1 (1960): 55-58.

[9] Fornberg, Bengt. "Steady viscous flow past a sphere at high Reynolds numbers." Journal of Fluid Mechanics 190 (1988): 471-489.

[10] Ghadimi, Euhanna, et al. "On the optimal step-size selection for the alternating direction method of multipliers." IFAC Proceedings Volumes 45.26 (2012): 139-144.

[11] Goldburg, A., and B. H. Florsheim. "Transition and Strouhal number for the incompressible wake of various bodies." The Physics of Fluids 9.1 (1966): 45-50.

[12] Gushchin, V. A., et al. "Direct numerical simulation of the transitional separated fluid flows around a sphere and a circular cylinder." Journal of Wind Engineering and Industrial Aerodynamics 90.4-5 (2002): 341-358.

[13] Haberman, William L., and Rose M. Sayre. Motion of rigid and fluid spheres in stationary and moving liquids inside cylindrical tubes. No. DTMB-1143. David Taylor Model Basin Washington DC, 1958.

[14] Hunt, Julian CR, Alan A. Wray, and Parviz Moin. "Eddies, streams, and convergence zones in turbulent flows." (1988).

[15] Jang, Young Il, and Sang Joon Lee. "Visualization of turbulent flow around a sphere at subcritical Reynolds numbers." Journal of Visualization 10.4 (2007): 359-366.

[16] Johnson, T. A., and V. C. Patel. "Flow past a sphere up to a Reynolds number of 300." Journal of Fluid Mechanics 378 (1999): 19-70.

[17] Jovanović, Mihailo R., Peter J. Schmid, and Joseph W. Nichols. "Sparsity-promoting dynamic mode decomposition." Physics of Fluids 26.2 (2014): 024103.

[18] Kalro, Vinay, and T. Tezduyar. "Parallel 3D Finite Element Computation of Unsteady Flows Past a Sphere." Advances in High Performance Computing. Springer, Dordrecht, 1997. 335-352.

[19] Kanaris, Nicolas, Dimokratis Grigoriadis, and Stavros Kassinos. "Three dimensional flow around a circular cylinder confined in a plane channel." Physics of Fluids 23.6 (2011): 064106.

[20] Kim, H. J., and P. A. Durbin. "Observations of the frequencies in a sphere wake and of drag

Physics of Fluids ACCEPTED MANUSCRIPT
This is the author's peer reviewed, accepted manuscript. However, the online version of record will be different from this version once it has been copyedited and typeset.
PLEASE CITE THIS ARTICLE AS DOI:10.1063/5.0017349
AIP Publishing

increase by acoustic excitation." The Physics of fluids 31.11 (1988): 3260-3265.

[21]Kim, Dongjoo, and Haecheon Choi. "Laminar flow past a sphere rotating in the streamwise direction." Journal of Fluid Mechanics 461 (2002): 365.

[22]Kim, Inchul, and Arne J. Pearlstein. "Stability of the flow past a sphere." Journal of Fluid Mechanics 211 (1990): 73-93.

[23]Kim, Dongjoo, Hyungseok Choi, and Haecheon Choi. "Characteristics of laminar flow past a sphere in uniform shear." Physics of Fluids 17.10 (2005): 103602.

[24]Krishnan, Suresh, and A. Kaman. "Effect of blockage ratio on drag and heat transfer from a centrally located sphere in pipe flow." Engineering Applications of Computational Fluid Mechanics 4.3 (2010): 396-414.

[25]Le Clair, B. P., A. E. Hamielec, and H. R. Pruppacher. "A numerical study of the drag on a sphere at low and intermediate Reynolds numbers." Journal of the Atmospheric Sciences 27.2 (1970): 308-315.

[26]Lee, Sungsu. "A numerical study of the unsteady wake behind a sphere in a uniform flow at moderate Reynolds numbers." Computers & Fluids 29.6 (2000): 639-667.

[27]Loosen, S., et al. "Numerical investigation of the turbulent wake of a generic space launcher at transonic speed." 7th European Conference for Aeronautics and Aerospace Sciences, https://doi.org/10.13009/EUCASS2017-561. 2017.

[28]Lorite-Díez, M., and J. I. Jiménez-González. “Description of the Transitional Wake behind a Strongly Streamwise Rotating Sphere.” Journal of Fluid Mechanics, vol. 896, 2020, p. A18., doi:10.1017/jfm.2020.342.

[29]Magnaudet, Jacques, Mayela Rivero, and Jean Fabre. "Accelerated flows past a rigid sphere or a spherical bubble. Part 1. Steady straining flow." Journal of fluid mechanics 284 (1995): 97-135.

[30]Mathupriya, P., et al. "Numerical investigations of flow over a confined circular cylinder." 21st Australasian Fluid Mechanics Conference, AFMC 2018. Australasian Fluid Mechanics Society, 2018.

[31]Matsumoto, Daiki, and Thomas Indinger. "On-the-fly algorithm for dynamic mode decomposition using incremental singular value decomposition and total least squares." arXiv preprint arXiv:1703.11004 (2017).

[32]Mittal, Rajat, and F. Najjar. "Vortex dynamics in the sphere wake." 30th Fluid Dynamics Conference. 1999.

[33]Nadge, Pankaj M., and R. N. Govardhan. "High Reynolds number flow over a backward-facing step: structure of the mean separation bubble." Experiments in fluids 55.1 (2014): 1657.

[34]Nagata, Takayuki, et al. "Investigation on subsonic to supersonic flow around a sphere at low Reynolds number of between 50 and 300 by direct numerical simulation." Physics of Fluids 28.5 (2016): 056101.

[35]Nagata, T., et al. "Direct numerical simulation of flow past a transversely rotating sphere up to a Reynolds number of 300 in compressible flow." Journal of Fluid Mechanics 857 (2018): 878-906.

[36]Nidhan, Sheel, et al. "Dynamic Mode Decomposition of Stratified Wakes." AIAA Aviation 2019 Forum. 2019.

[37]Oh, Jang Hoon, and Seung Jong Lee. "A study on the Newtonian fluid flow past a sphere in a tube." Korean Journal of Chemical Engineering 5.2 (1988): 190-196.

[38]Ohmichi, Yuya. "Preconditioned dynamic mode decomposition and mode selection algorithms for large datasets using incremental proper orthogonal decomposition." AIP Advances 7.7 (2017):

Physics of Fluids ACCEPTED MANUSCRIPT
This is the author's peer reviewed, accepted manuscript. However, the online version of record will be different from this version once it has been copyedited and typeset.
PLEASE CITE THIS ARTICLE AS DOI:10.1063/5.0017349
AIP Publishing

075318.

[39]Oxberry, Geoffrey M., et al. "Limited-memory adaptive snapshot selection for proper orthogonal decomposition." International Journal for Numerical Methods in Engineering 109.2 (2017): 198-217.

[40]Poon, E., et al. "Numerical studies of high Reynolds number flow past a stationary and rotating sphere." Proceedings of the 7th International Conference on CFD in the Minerals and Process Industries. 2009.

[41]Poon, Eric KW, et al. "Flow past a transversely rotating sphere at Reynolds numbers above the laminar regime." Journal of Fluid Mechanics 759 (2014): 751-781.

[42]Pope, Stephen B. "Turbulent flows." (2001): 2020.

[43]Rodríguez, Ivette, et al. "Direct numerical simulation of the flow over a sphere at Re= 3700." Turbulence Heat and Mass Transfer 6. Proceedings of the Sixth International Symposium On Turbulence Heat and Mass Transfer. Begel House Inc., 2009.

[44]Rodríguez, I., et al. "Flow dynamics in the turbulent wake of a sphere at sub-critical Reynolds numbers." Computers & Fluids 80 (2013): 233-243.

[45]Sakamoto, H., and H. Haniu. "A study on vortex sheldding from spheres in a uniform flow." Journal of fluids engineering 112.4 (1990): 386-392.

[46]Sakamoto, Hiroshi, and Hiroyuki Haniu. "The formation mechanism and shedding frequency of vortices from a sphere in uniform shear flow." Journal of Fluid Mechanics 287 (1995): 151-171.

[47]Schmid, Peter J. "Dynamic mode decomposition of numerical and experimental data." Journal of fluid mechanics 656 (2010): 5-28.

[48]Schmid, M., and M. Perić. "Large eddy simulation of subcritical flow around sphere." High Performance Computing in Science and Engineering 2000. Springer, Berlin, Heidelberg, 2001. 368-376.

[49]Seidl, V., S. Muzaferija, and M. Perić. "Parallel DNS with local grid refinement." Applied Scientific Research 59.4 (1997): 379-394.

[50]Shahcheraghi, N., and H. A. Dwyer. "Fluid flow and heat transfer over a three-dimensional spherical object in a pipe." (1998): 985-990.

[51]Sheard, G. J., and Kris Ryan. "Pressure-driven flow past spheres moving in a circular tube." Journal of Fluid Mechanics 592 (2007): 233-262.

[52]Singha, Sintu, and K. P. Sinhamahapatra. "Flow past a circular cylinder between parallel walls at low Reynolds numbers." Ocean Engineering 37.8-9 (2010): 757-769.

[53]Smythe, W. R. "Flow around a sphere in a circular tube." The Physics of Fluids 4.6 (1961): 756-759.

[54]Stankiewicz, Witold, et al. "On the need of mode interpolation for data-driven Galerkin models of a transient flow around a sphere." Theoretical and Computational Fluid Dynamics 31.2 (2017): 111-126.

[55]Statnikov, Vladimir, et al. "Analysis of pressure perturbation sources on a generic space launcher after-body in supersonic flow using zonal turbulence modeling and dynamic mode decomposition." Physics of Fluids 27.1 (2015): 016103.

[56]Subramanian, R. Shankar. "Drag on spherical particles and steady settling velocities." note available online at http://www. clarkson. edu/subramanian/ch301/notes/index. htm (2010): 1-3.

[57]Suresh, Krishnan, and Aravamudan Kannan. "Effects of particle diameter and position on hydrodynamics around a confined sphere." Industrial & engineering chemistry research 50.23

Physics of Fluids ACCEPTED MANUSCRIPT

AIP Publishing

This is the author's peer reviewed, accepted manuscript. However, the online version of record will be different from this version once it has been copyedited and typeset.
PLEASE CITE THIS ARTICLE AS DOI:10.1063/5.0017349

(2011): 13137-13160.

[58] Tamai, Nobuyuki, Takashi Asaeda, and Norio Tanaka. "Vortex structures around a hemispheric hump." Boundary-layer meteorology 39.3 (1987): 301-314.

[59] Taneda, Sadatoshi. "Experimental investigation of the wake behind a sphere at low Reynolds numbers." Journal of the Physical Society of Japan 11.10 (1956): 1104-1108.

[60] Tian, Xinliang, et al. "Large-eddy simulation of the flow normal to a flat plate including corner effects at a high Reynolds number." Journal of Fluids and Structures 49 (2014): 149-169.

[61] Tiwari, Shashank S., et al. "Insights into the physics of dominating frequency modes for flow past a stationary sphere: Direct numerical simulations." Physics of Fluids 31.4 (2019): 045108.

[62] Tomboulides, Ananias G., and Steven A. Orszag. "Numerical investigation of transitional and weak turbulent flow past a sphere." Journal of Fluid Mechanics 416 (2000): 45-73.

[63] Tomboulides, A., S. Orszag, and G. Karniadakis. "Direct and large-eddy simulations of axisymmetric wakes." 31st Aerospace Sciences Meeting. 1993.

[64] Welch, Peter. "The use of fast Fourier transform for the estimation of power spectra: a method based on time averaging over short, modified periodograms." IEEE Transactions on audio and electroacoustics 15.2 (1967): 70-73.

[65] Wham, R. M., O. A. Basaran, and C. H. Byers. "Wall effects on flow past solid spheres at finite Reynolds number." Industrial & engineering chemistry research 35.3 (1996): 864-874.

[66] Wood, Jens Nikolas, et al. "Experimental investigation and large-eddy simulation of the turbulent flow past a smooth and rigid hemisphere." Flow, Turbulence and Combustion 97.1 (2016): 79-119.

[67] Wu, J-S., and G. M. Faeth. "Sphere wakes in still surroundings at intermediate Reynolds numbers." AIAA journal 31.8 (1993): 1448-1455.

[68] Wu, Wen, Charles Meneveau, and Rajat Mittal. "Spatio-temporal dynamics of turbulent separation bubbles." Journal of Fluid Mechanics 883 (2020).

[69] Yang, B. et al. “Migration of a sphere in tube flow.” Journal of Fluid Mechanics 540 (2005): 109-131.

[70] Yu, Ming, et al. “Data-Driven Construction of a Reduced-Order Model for Supersonic Boundary Layer Transition.” Journal of Fluid Mechanics, vol. 874, 2019, pp. 1096–1114., doi:10.1017/jfm.2019.470.

[71] Zheng, R., N. Phan-Thien, and R. I. Tanner. "The flow past a sphere in a cylindrical tube: effects of intertia, shear-thinning and elasticity." Rheologica acta 30.6 (1991): 499-510.

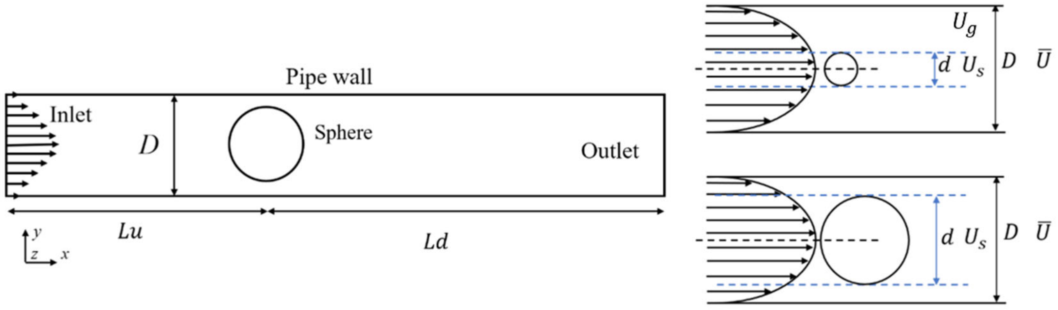
Pipe wall
Inlet
D
Sphere
Outlet
Lu
Ld
y
z
x
U_g
d
U_s
D
$\overline{U}$
d
U_s
D
$\overline{U}$

Figure 1 Computational domain and an example view of the sphere with $BR = 0.4$ and $BR = 0.8$.

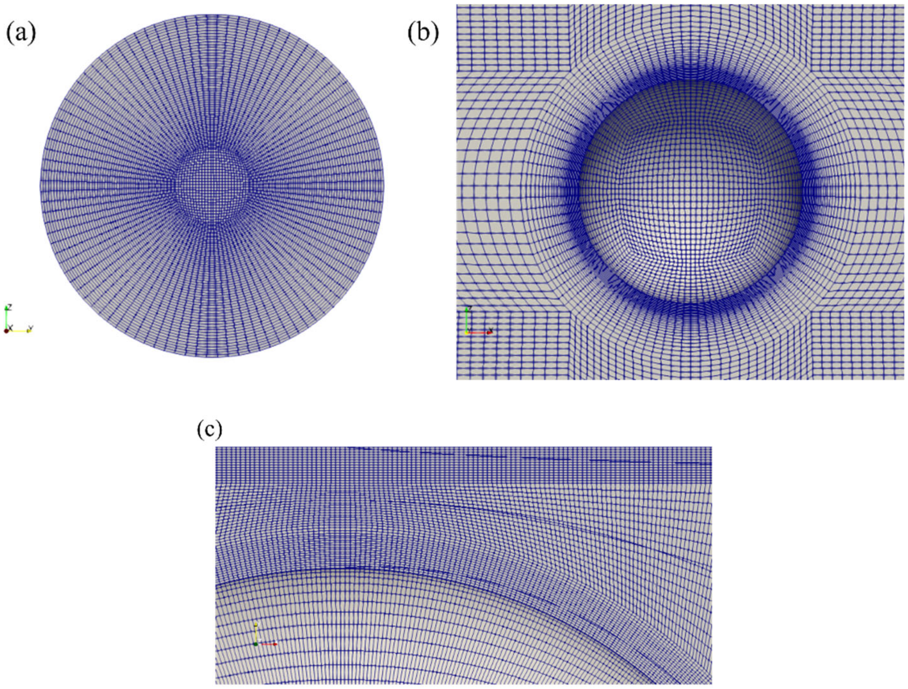

Figure 2 Computational grids. (a) YZ view at the inlet; (b) XZ view around the sphere for $BR = 0.2$ and (c) XZ view around the sphere and near the pipe wall for $BR = 0.8$

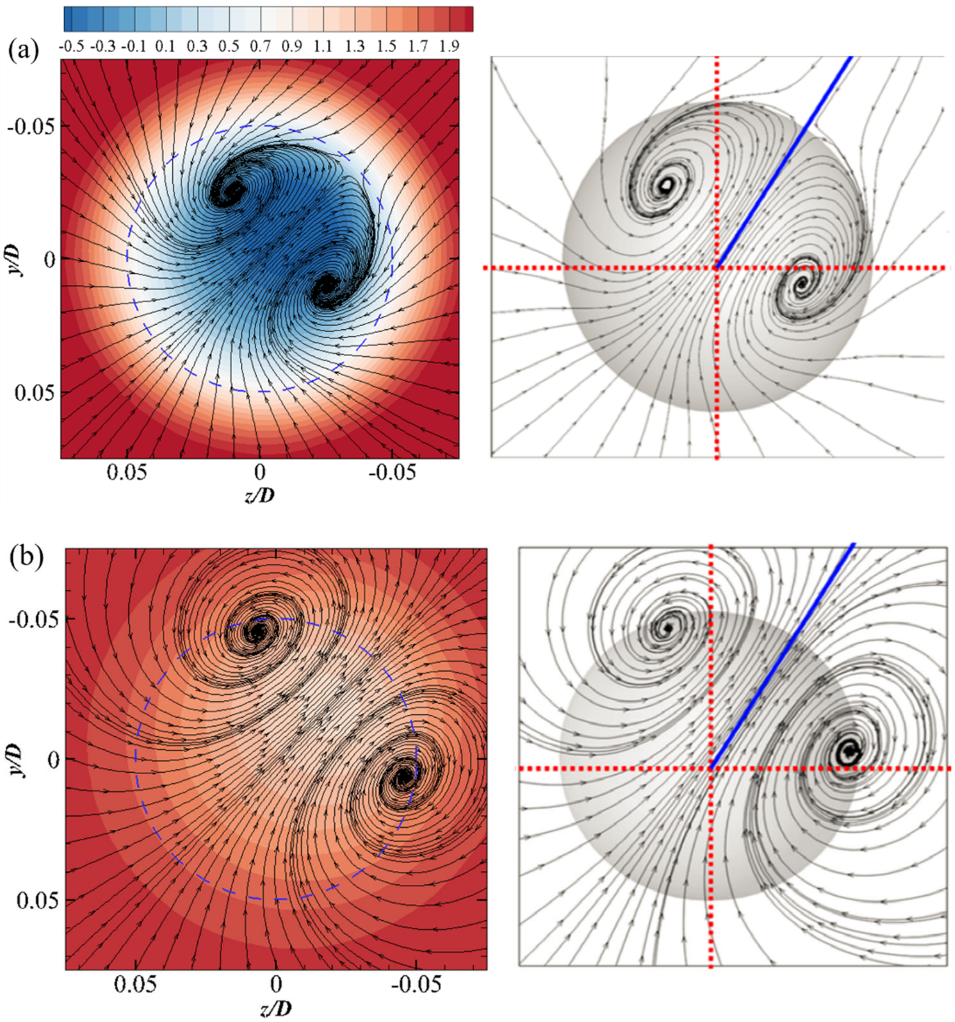

Figure 3 Time-averaged streamlines on two constant x/d planes at (a) $x/d = 1$ and (b) $x/d = 7$ for $BR = 0.1$ at $Re_s = 250$ for the sphere subjected to a uniform flow of the present study (Left. The blue dashed lines indicate the sphere) compared with those in Tiwari et al. [61] (Right) at the same streamwise locations. The color contours denote the value of the time-averaged streamwise velocity.

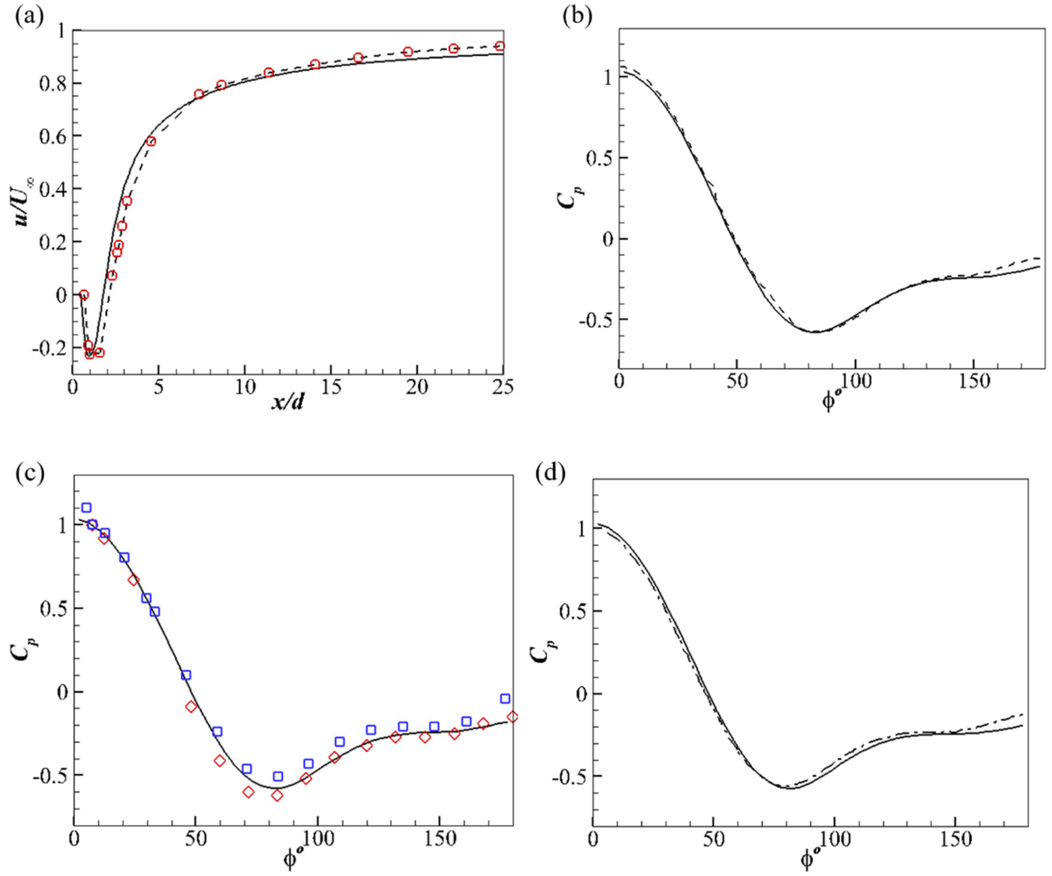

Figure 4 (a) The time-averaged streamwise velocity along the centerline of the pipe at $Re_s = 300$; the pressure distributions on the sphere at (b) $Re_s = 250$; (c) $Re_s = 300$; (d) $Re_s = 350$ (solid lines: present study; red circles: experimental data in Wu and Faeth[67] at $Re_s = 280$; dashed: DNS data in Tomboulides and Orszag[62] at $Re_s = 200$; red diamond: Le Clair et al.[25] at $Re_s = 300$; blue square: Magnaudet et al.[29] at $Re_s = 300$; Dash-dotted: Bagchi et al.[2] at $Re_s = 350$)

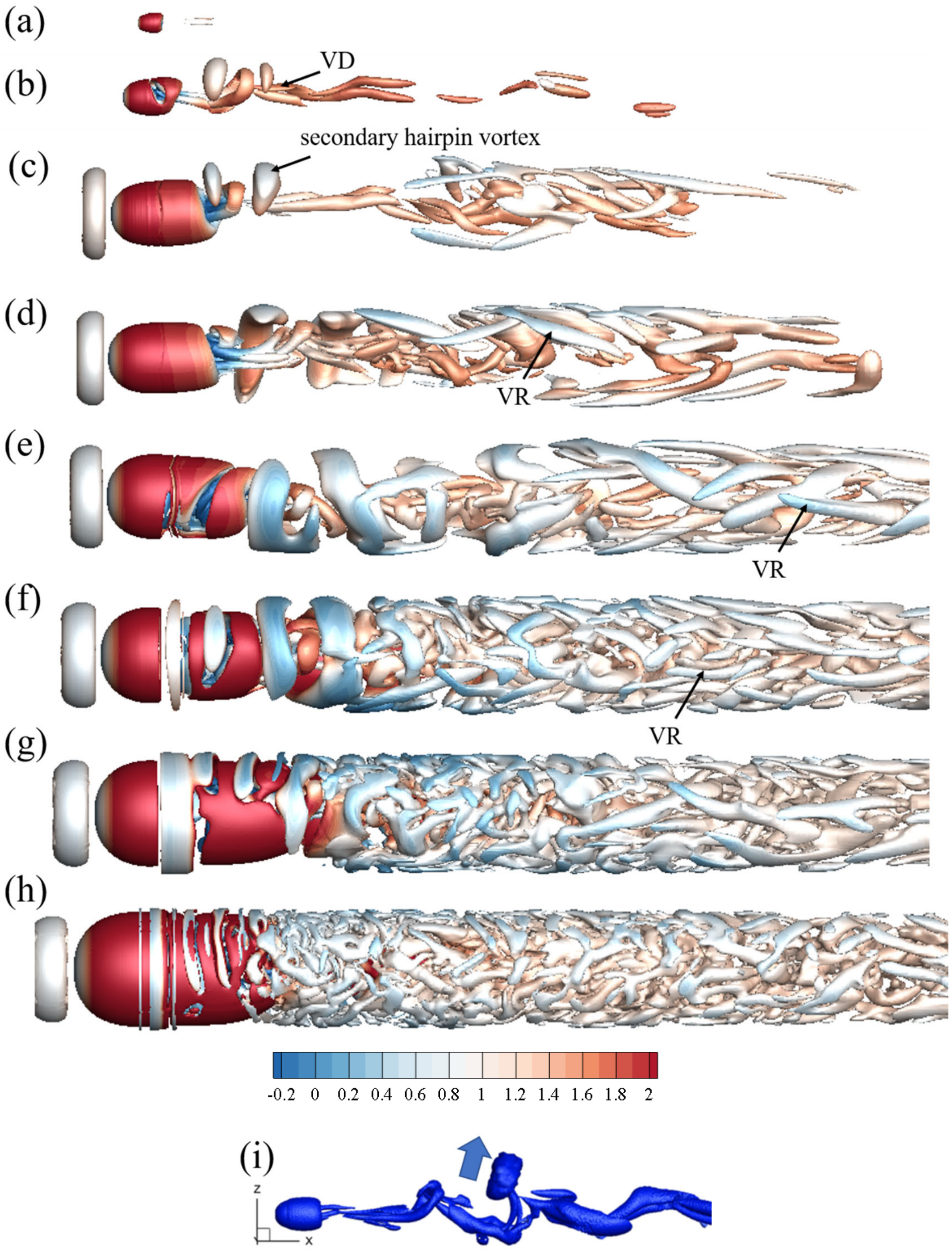
(a)
(b)
VD
(c)
secondary hairpin vortex
(d)
VR
(e)
VR
(f)
VR
(g)
(h)
-0.2
0
0.2
0.4
0.6
0.8
1
1.2
1.4
1.6
1.8
2
(i)
z
x

Figure 5 Instantaneous iso-surfaces of $Q = 2$ colored by the time-averaged streamwise velocity at $Re_p = 1250$ for (a) $BR = 0.1$; (b) $BR = 0.2$; (c) $BR = 0.4$; (d) $BR = 0.5$; (e) $BR = 0.6$; (f) $BR = 0.7$; (g) $BR = 0.8$; (h) $BR = 0.9$; (i) $Re_s = 500$ reprint of Tiwari et al.[61]

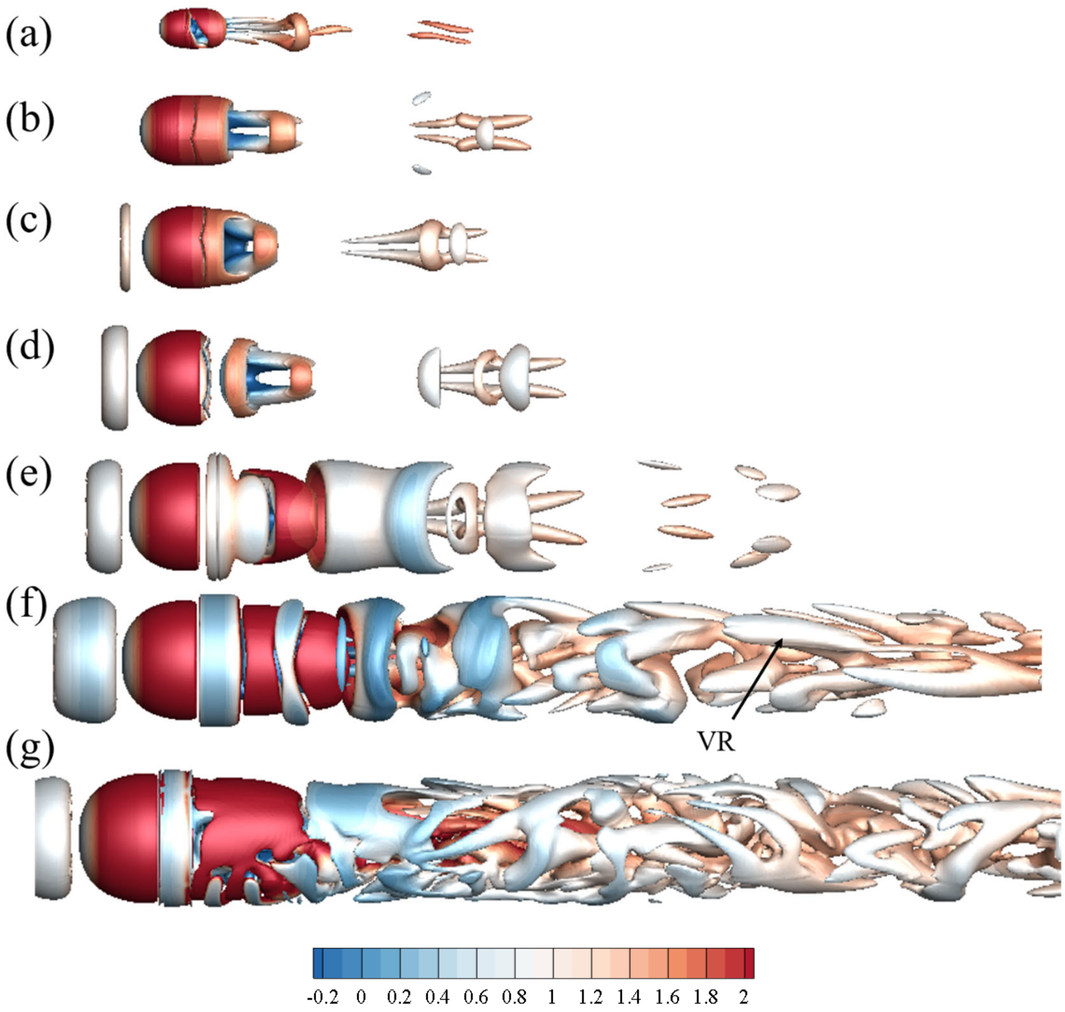
(a)
(b)
(c)
(d)
(e)
(f)
(g)
VR
-0.2
0
0.2
0.4
0.6
0.8
1
1.2
1.4
1.6
1.8
2

Figure 6 Instantaneous iso-surfaces of $Q^* = 1$ colored by the time-averaged streamwise velocity at $Re_s = 500$ for (a) $BR = 0.2$; (b) $BR = 0.4$; (c) $BR = 0.5$; (d) $BR = 0.6$; (e) $BR = 0.7$; (f) $BR = 0.8$; (g) $BR = 0.9$

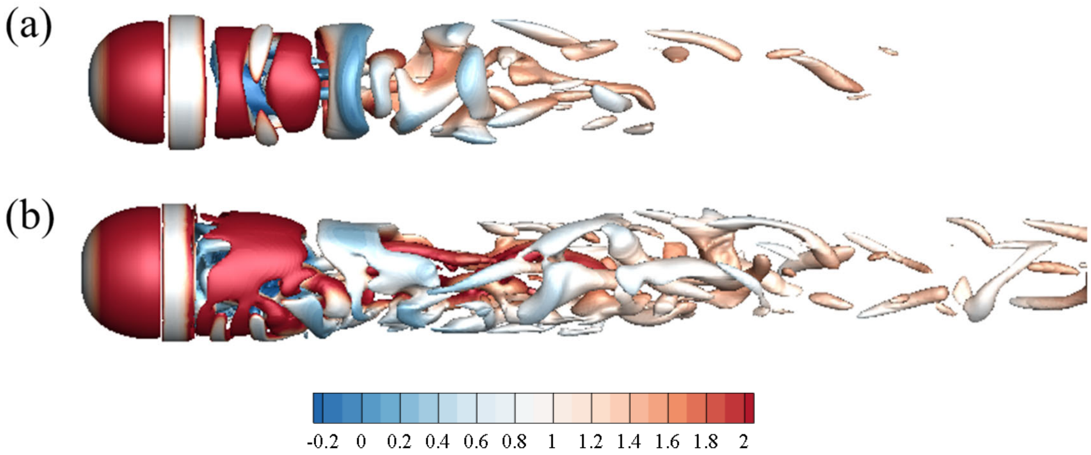
(a)
(b)
-0.2
0
0.2
0.4
0.6
0.8
1
1.2
1.4
1.6
1.8
2

Figure 7 Instantaneous iso-surfaces of $Q^* = 10$ colored by the time-averaged streamwise velocity at $Re_s = 500$ for (a) $BR = 0.8$ and (b) $BR = 0.9$

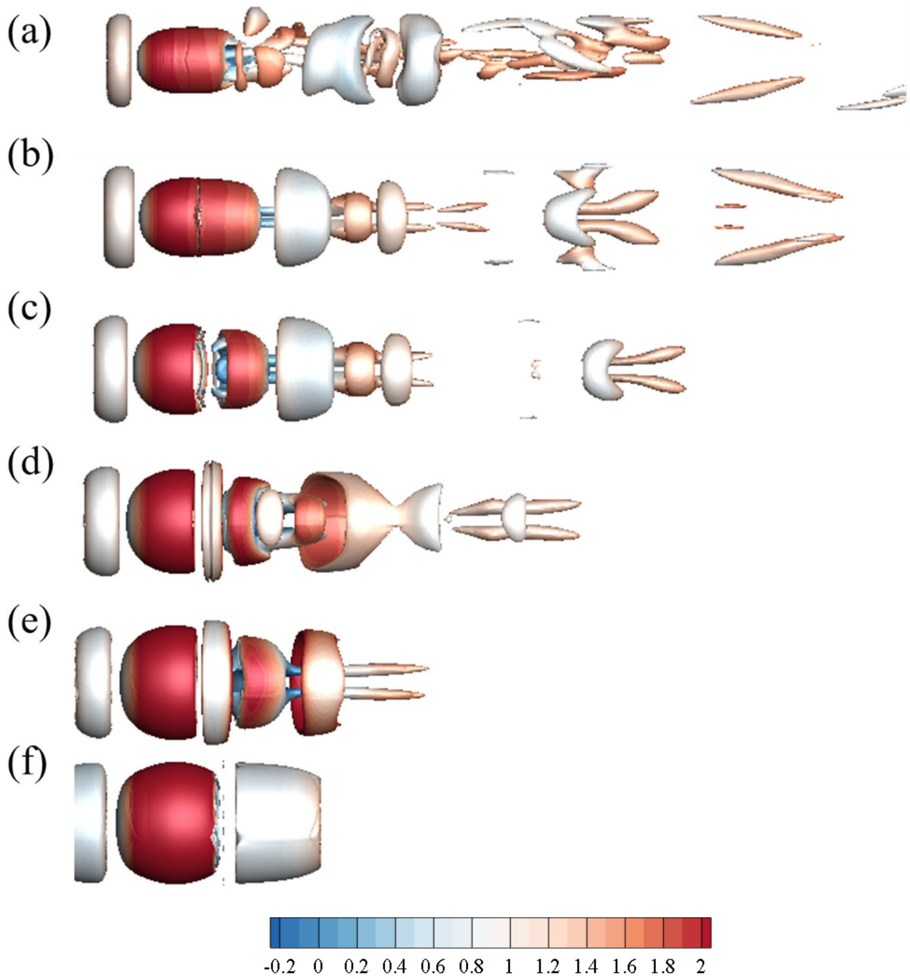
(a)
(b)
(c)
(d)
(e)
(f)
-0.2
0
0.2
0.4
0.6
0.8
1
1.2
1.4
1.6
1.8
2

Figure 8 Instantaneous iso-surfaces of $Q^* = 1$ colored by the time-averaged streamwise velocity at $Re_g = 500$ for (a) $BR = 0.4$; (b) $BR = 0.5$; (c) $BR = 0.6$; (d) $BR = 0.7$; (e) $BR = 0.8$; (f) $BR = 0.9$

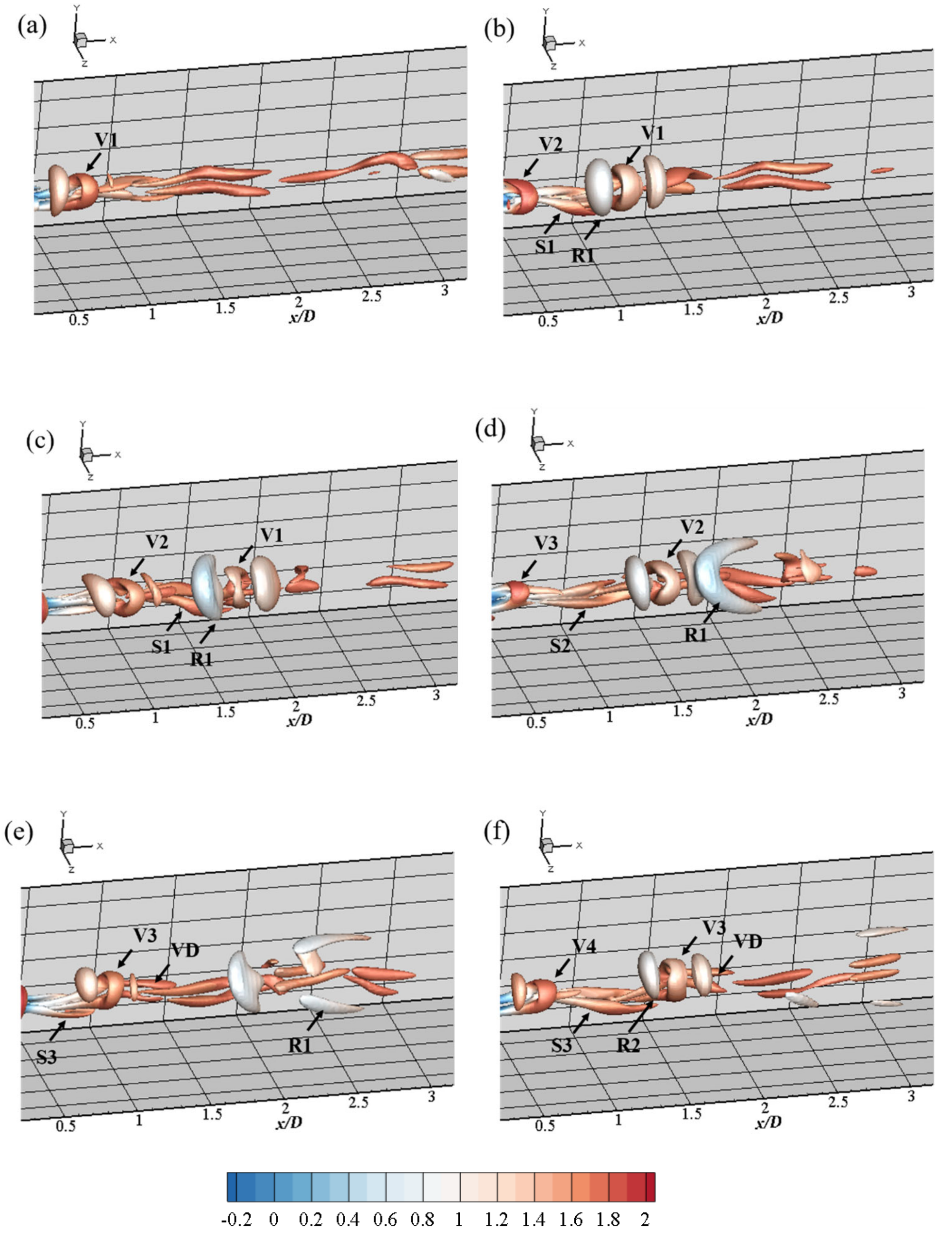
(a)
V1
(b)
V2
V1
S1
R1
(c)
V2
V1
S1
R1
(d)
V3
V2
S2
R1
(e)
V3
VD
S3
R1
(f)
V4
V3
VD
S3
R2
Y
X
Z
0.5
1
1.5
2
2.5
3
x/D
-0.2
0
0.2
0.4
0.6
0.8
1
1.2
1.4
1.6
1.8
2

Figure 9 Instantaneous iso-surfaces of $Q = 2$ for $BR = 0.2$ colored by the time-averaged streamwise velocity at $Re_p = 1250$ at (a) $tU_s/d = 150$; (b) $tU_s/d = 154$; (c) $tU_s/d = 158$; (d) $tU_s/d = 162$; (e) $tU_s/d = 166$; (f) $tU_s/d = 170$

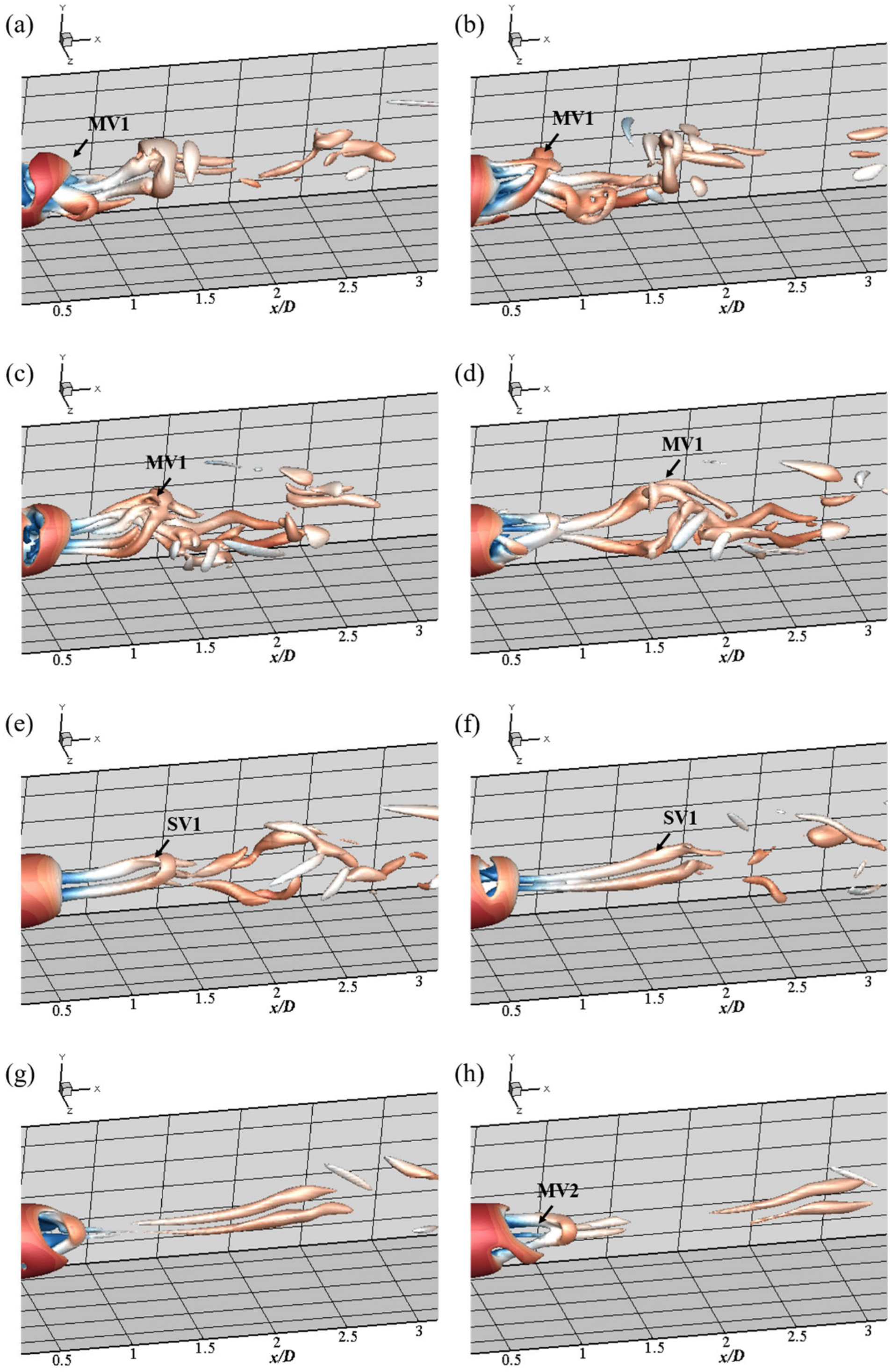
(a)
MV1
(b)
MV1
(c)
MV1
(d)
MV1
(e)
SV1
(f)
SV1
(g)
(h)
MV2
Y
X
Z
0.5
1
1.5
2
2.5
3
x/D

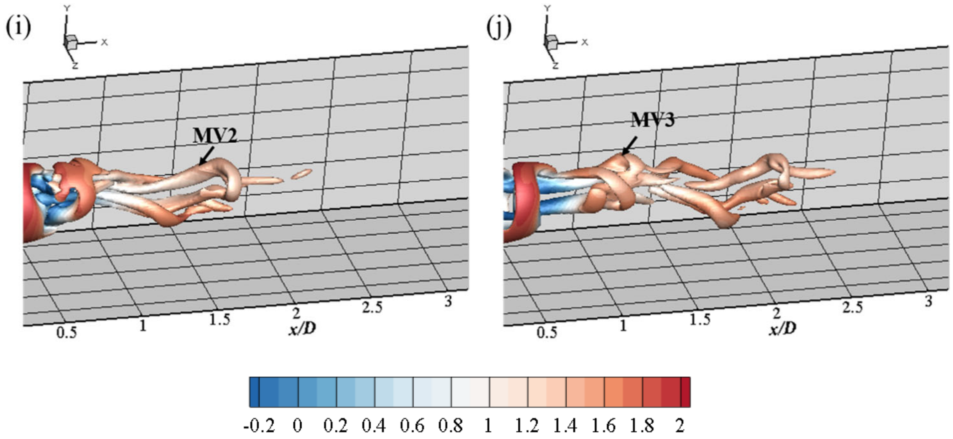
(i)
(j)
Y
X
Z
MV2
MV3
0.5
1
1.5
2
2.5
3
x/D
-0.2
0
0.2
0.4
0.6
0.8
1
1.2
1.4
1.6
1.8
2

Figure 10 Instantaneous iso-surfaces of $Q = 10$ for $BR = 0.4$ colored by the time-averaged streamwise velocity at $Re_p = 1250$ at (a) $tU_s/d = 649.52$; (b) $tU_s/d = 651.36$; (c) $tU_s/d = 653.2$; (d) $tU_s/d = 655.04$; (e) $tU_s/d = 656.88$; (f) $tU_s/d = 659.64$; (g) $tU_s/d = 661.48$; (h) $tU_s/d = 663.32$; (i) $tU_s/d = 665.16$; (j) $tU_s/d = 667$

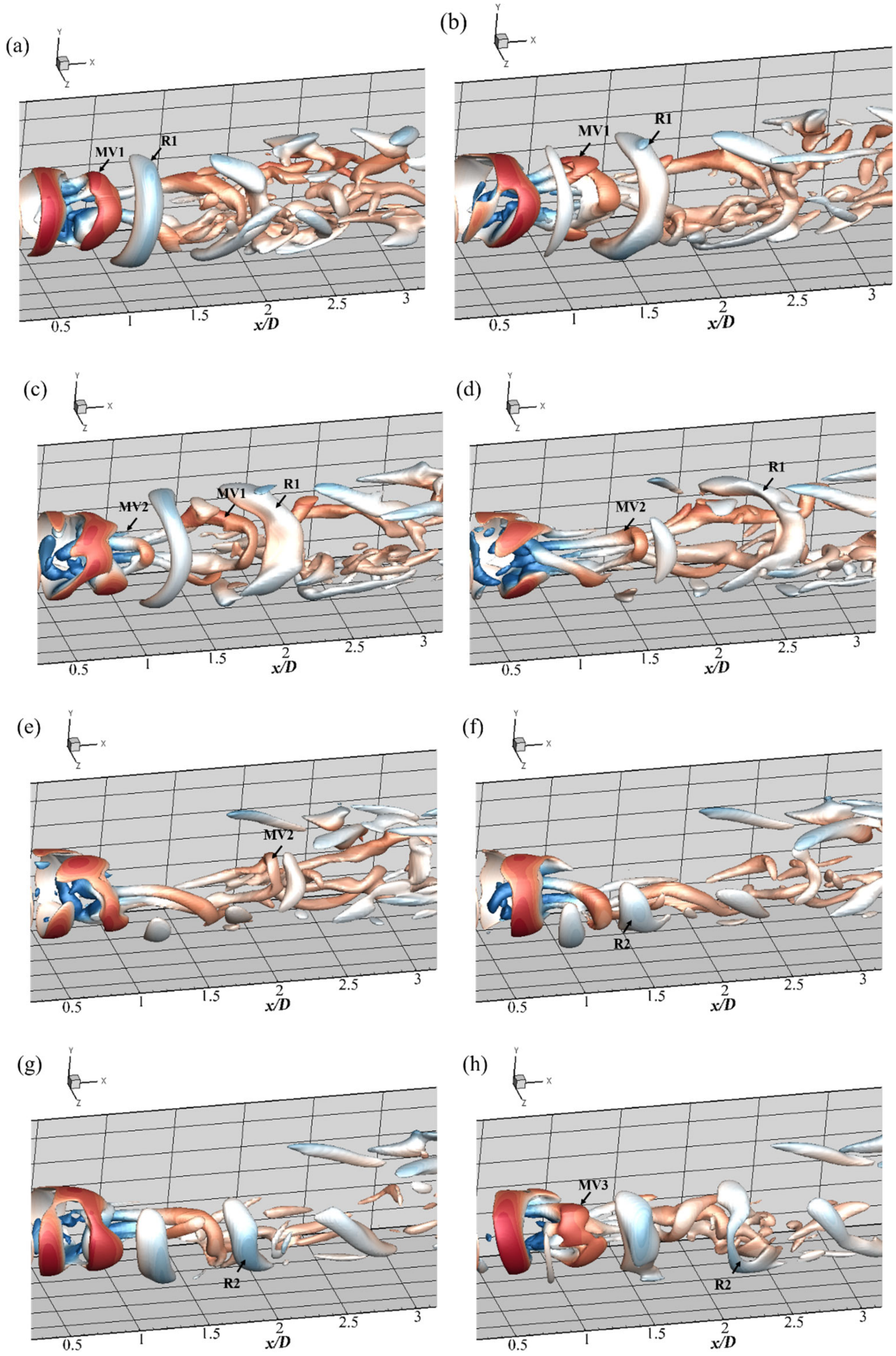
(a)
MV1
R1
(b)
MV1
R1
(c)
MV2
MV1
R1
(d)
MV2
R1
(e)
MV2
(f)
R2
(g)
R2
(h)
MV3
R2
Y
X
Z
0.5
1
1.5
2
2.5
3
x/D

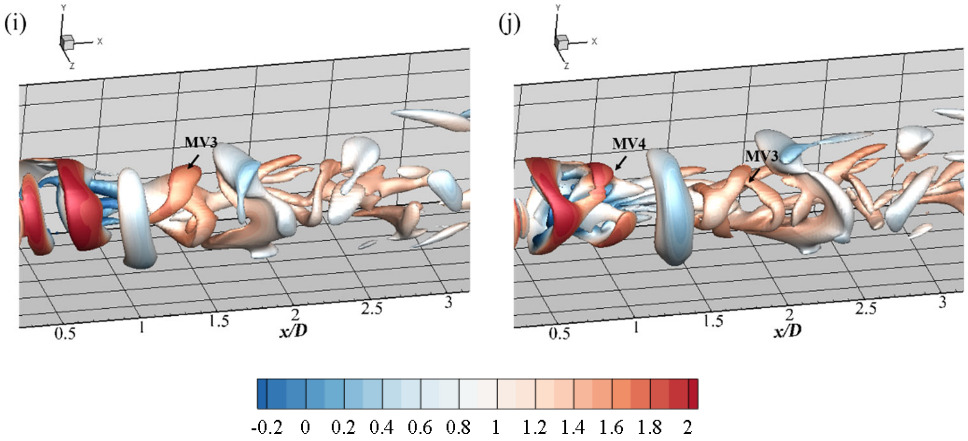
(i)
MV3
0.5
1
1.5
2
2.5
3
x/D
(j)
MV4
MV3
0.5
1
1.5
2
2.5
3
x/D
-0.2
0
0.2
0.4
0.6
0.8
1
1.2
1.4
1.6
1.8
2

Figure 11 Instantaneous iso-surfaces of $Q = 10$ for $BR = 0.6$ colored by the time-averaged streamwise velocity at $Re_p = 1250$ at (a) $tU_s/d = 508.4$; (b) $tU_s/d = 509.5$; (c) $tU_s/d = 510.6$; (d) $tU_s/d = 511.7$; (e) $tU_s/d = 512.8$; (f) $tU_s/d = 513.9$; (g) $tU_s/d = 515$; (h) $tU_s/d = 516.1$; (i) $tU_s/d = 517.2$; (j) $tU_s/d = 518.3$

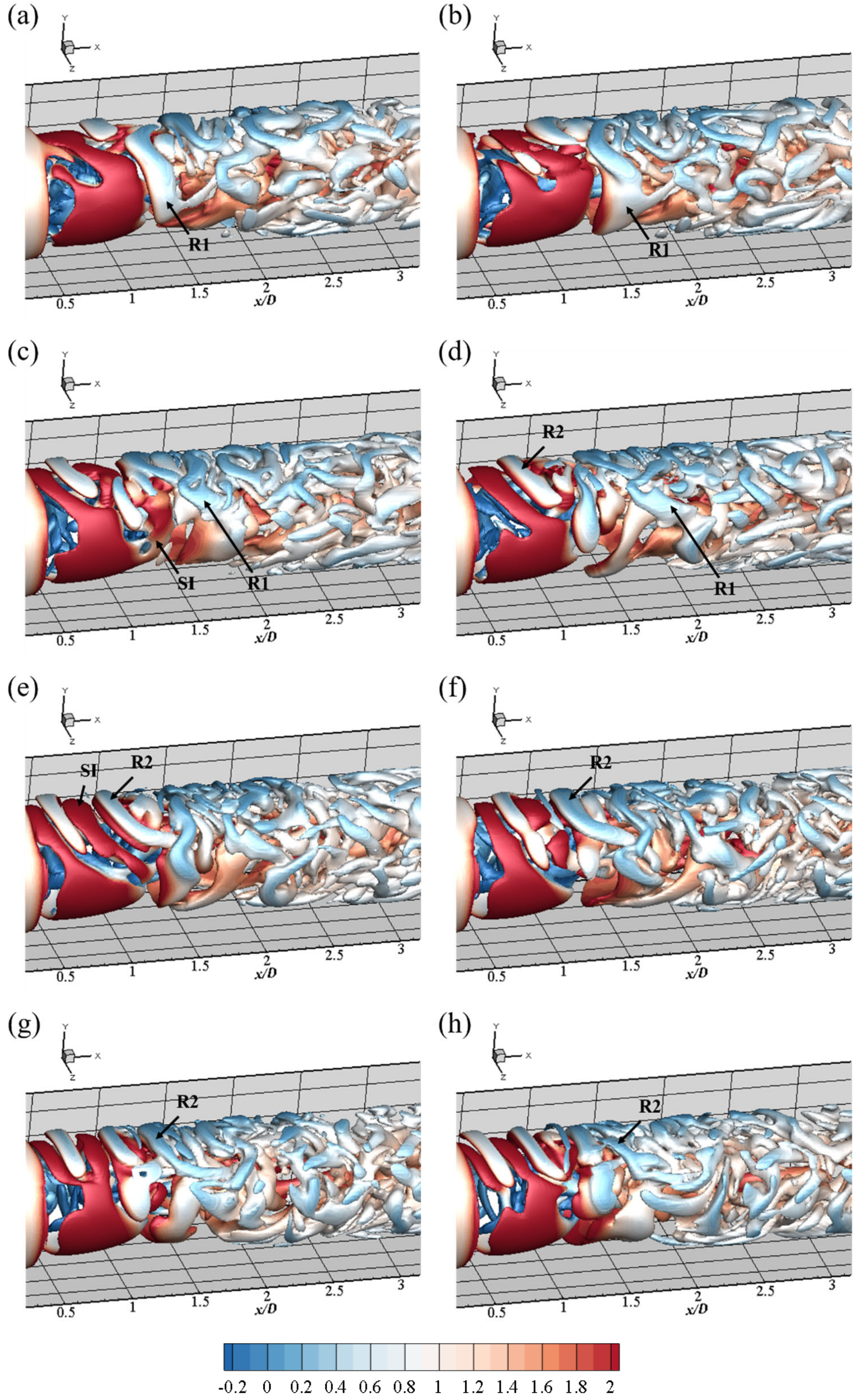
(a)
R1
(b)
R1
(c)
SI
R1
(d)
R2
R1
(e)
SI
R2
(f)
R2
(g)
R2
(h)
R2
Y
X
Z
0.5
1
1.5
2
2.5
3
x/D
-0.2
0
0.2
0.4
0.6
0.8
1
1.2
1.4
1.6
1.8
2

Figure 12 Instantaneous iso-surfaces of $Q = 10$ for $BR = 0.8$ colored by the time-averaged streamwise velocity at $Re_p = 1250$ at (a) $tU_s/d = 258.4$; (b) $tU_s/d = 258.74$; (c) $tU_s/d = 259.08$; (d) $tU_s/d = 259.42$; (e) $tU_s/d = 259.76$; (f) $tU_s/d = 260.1$; (g) $tU_s/d = 260.44$; (h) $tU_s/d = 260.78$

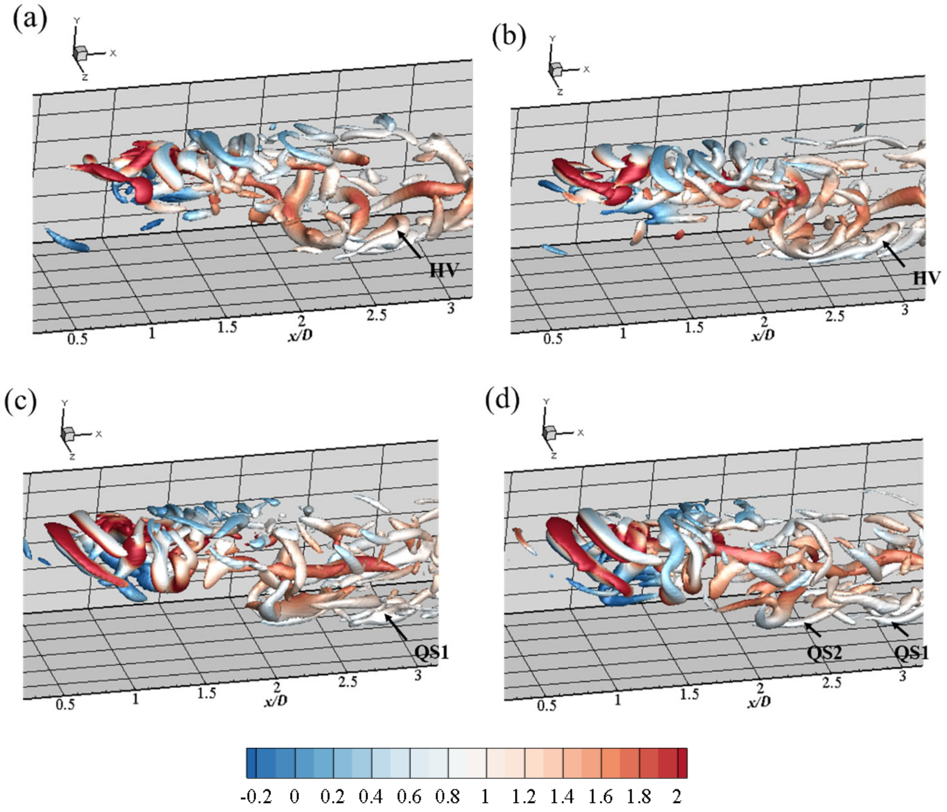
(a)
HV
0.5
1
1.5
2
2.5
3
x/D
(b)
HV
(c)
QS1
(d)
QS2
QS1
-0.2
0
0.2
0.4
0.6
0.8
1
1.2
1.4
1.6
1.8
2

Figure 13 Instantaneous iso-surfaces of $Q = 100$ for $BR = 0.8$ colored by the time-averaged streamwise velocity at $Re_p = 1250$ at (a) $tU_s/d = 258.4$; (b) $tU_s/d = 258.74$; (c) $tU_s/d = 259.08$; (d) $tU_s/d = 259.42$ in Figure 12

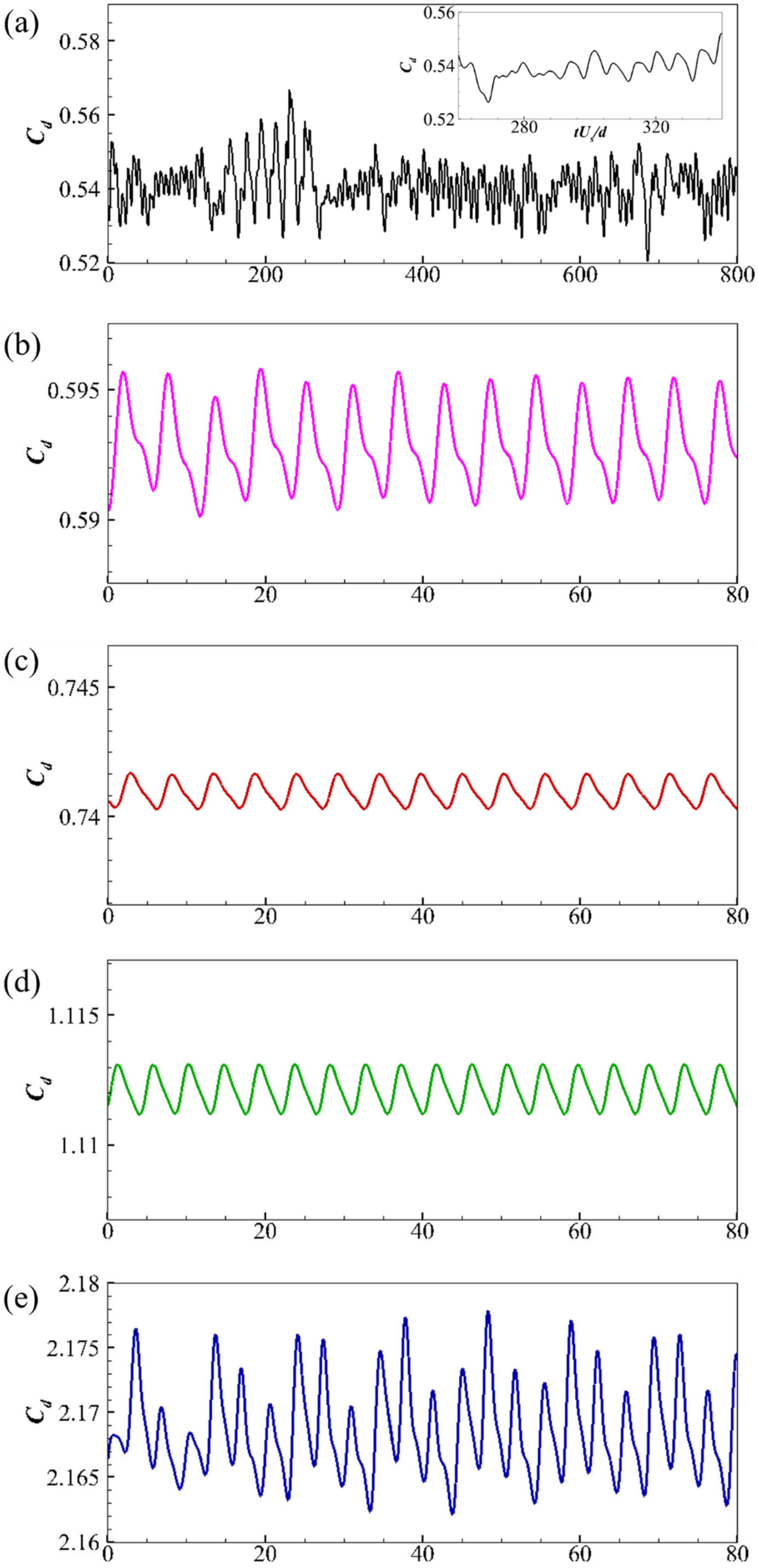
(a)
C_d
0.58
0.56
0.54
0.52
0
200
400
600
800
0.56
0.54
0.52
C_d
280
tU_s/d
320
(b)
C_d
0.595
0.59
0
20
40
60
80
(c)
C_d
0.745
0.74
0
20
40
60
80
(d)
C_d
1.115
1.11
0
20
40
60
80
(e)
C_d
2.18
2.175
2.17
2.165
2.16
0
20
40
60
80

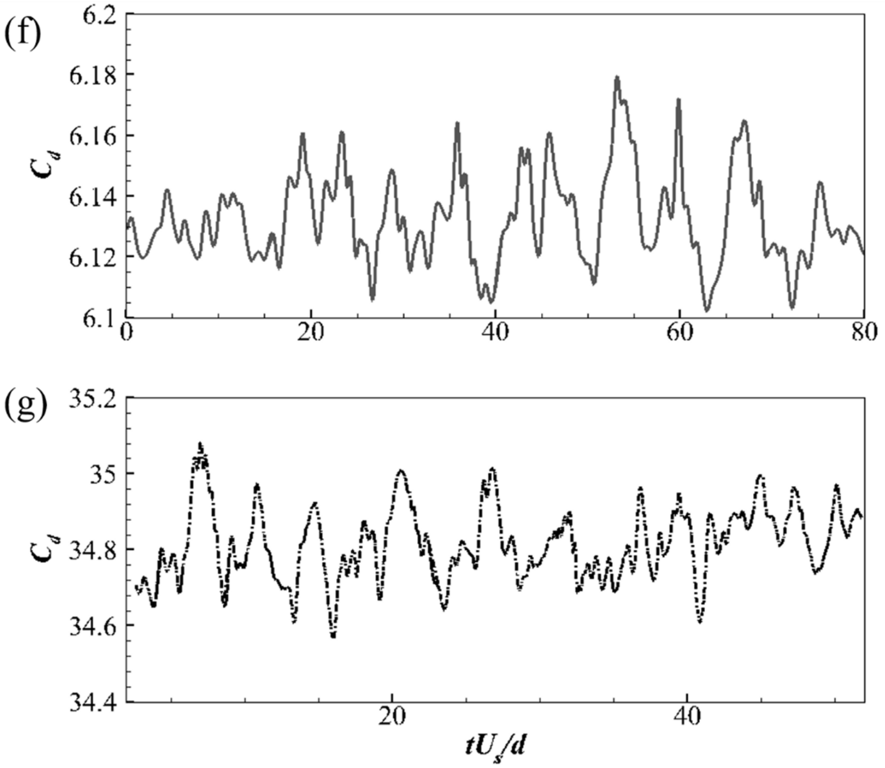

Figure 14 The time histories of C_d for (a) $BR = 0.2$; (b) $BR = 0.4$; (c) $BR = 0.5$; (d) $BR = 0.6$; (e) $BR = 0.7$; (f) $BR = 0.8$; (g) $BR = 0.9$

Physics of Fluids ACCEPTED MANUSCRIPT

AIP Publishing

This is the author's peer reviewed, accepted manuscript. However, the online version of record will be different from this version once it has been copyedited and typeset.
PLEASE CITE THIS ARTICLE AS DOI:10.1063/5.0017349

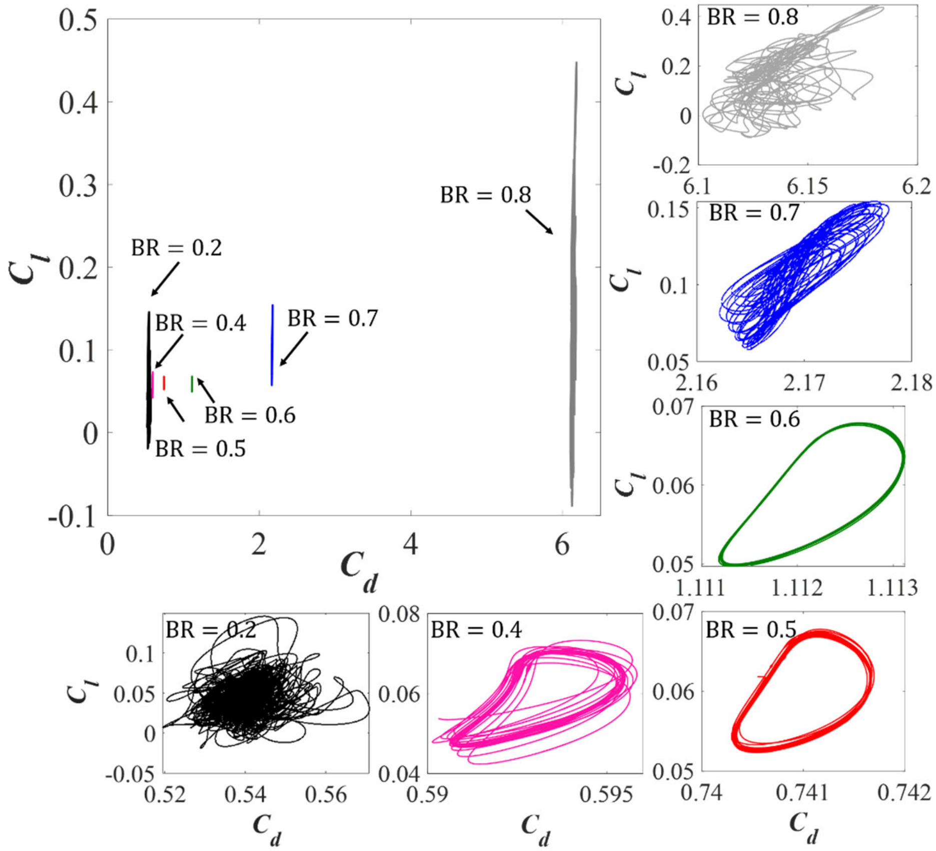

Figure 15 Phase diagram (C_d, C_l) for the sphere at $Re_s = 500$

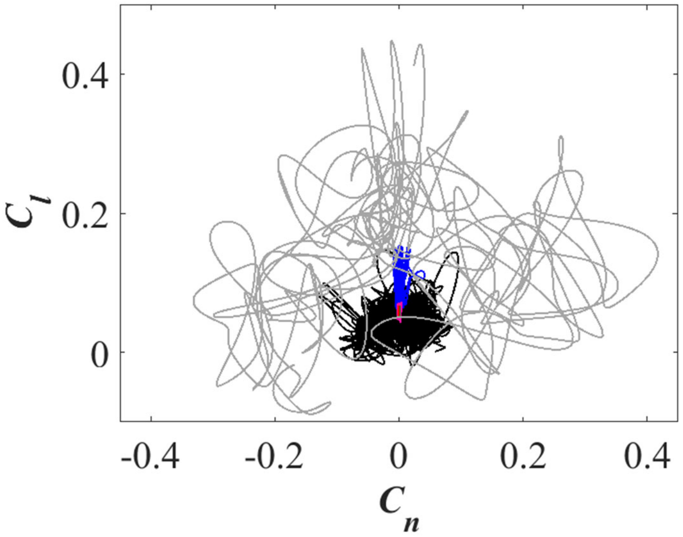

Figure 16 Phase diagram (C_n, C_l) for the sphere at $Re_s = 500$

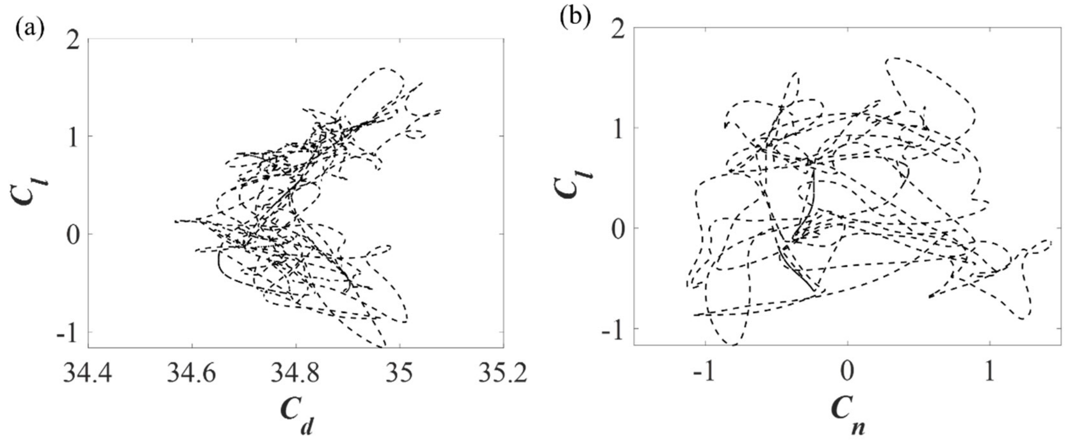

Figure 17 Phase diagram (a) (C_d, C_l) and (b) (C_n, C_l) for the sphere at $Re_s = 500$ for $BR = 0.9$

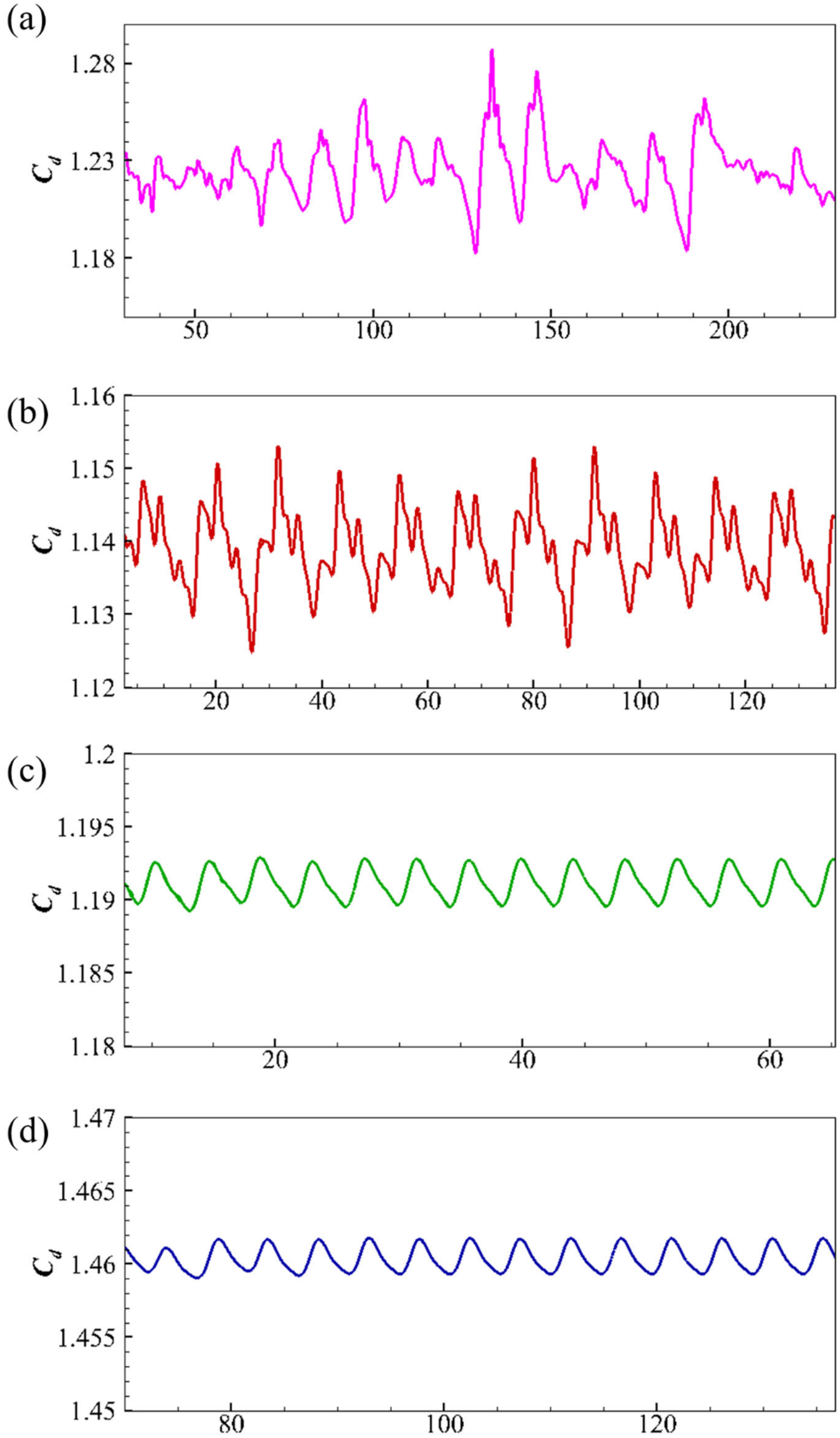
(a)
C_d
1.28
1.23
1.18
50
100
150
200
(b)
C_d
1.16
1.15
1.14
1.13
1.12
20
40
60
80
100
120
(c)
C_d
1.2
1.195
1.19
1.185
1.18
20
40
60
(d)
C_d
1.47
1.465
1.46
1.455
1.45
80
100
120

Physics of Fluids ACCEPTED MANUSCRIPT

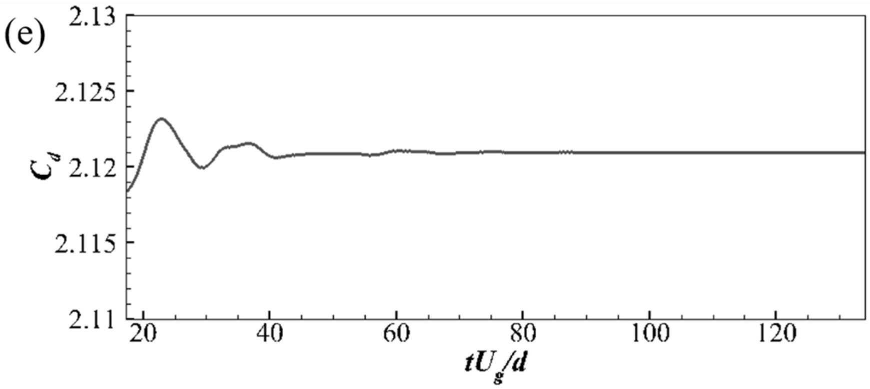

Figure 18 The time histories of C_d for (a) $BR = 0.4$; (b) $BR = 0.6$; (c) $BR = 0.6$; (d) $BR = 0.7$; (e) $BR = 0.8$

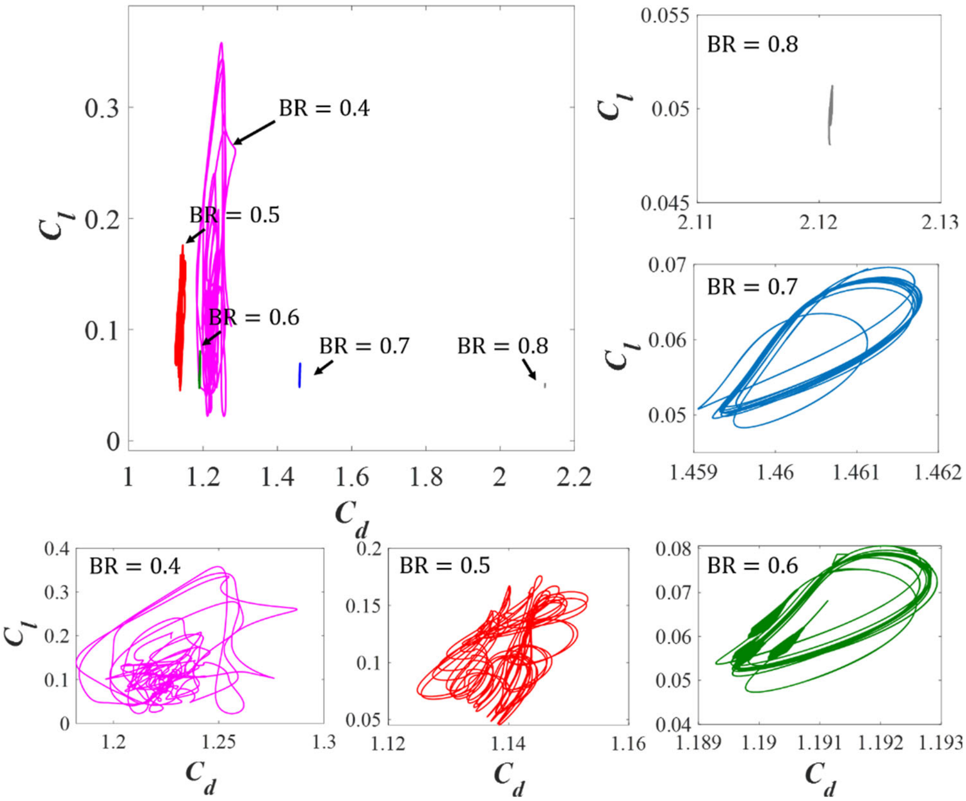

Figure 19 Phase diagram (C_d, C_l) for the sphere at $Re_g = 500$

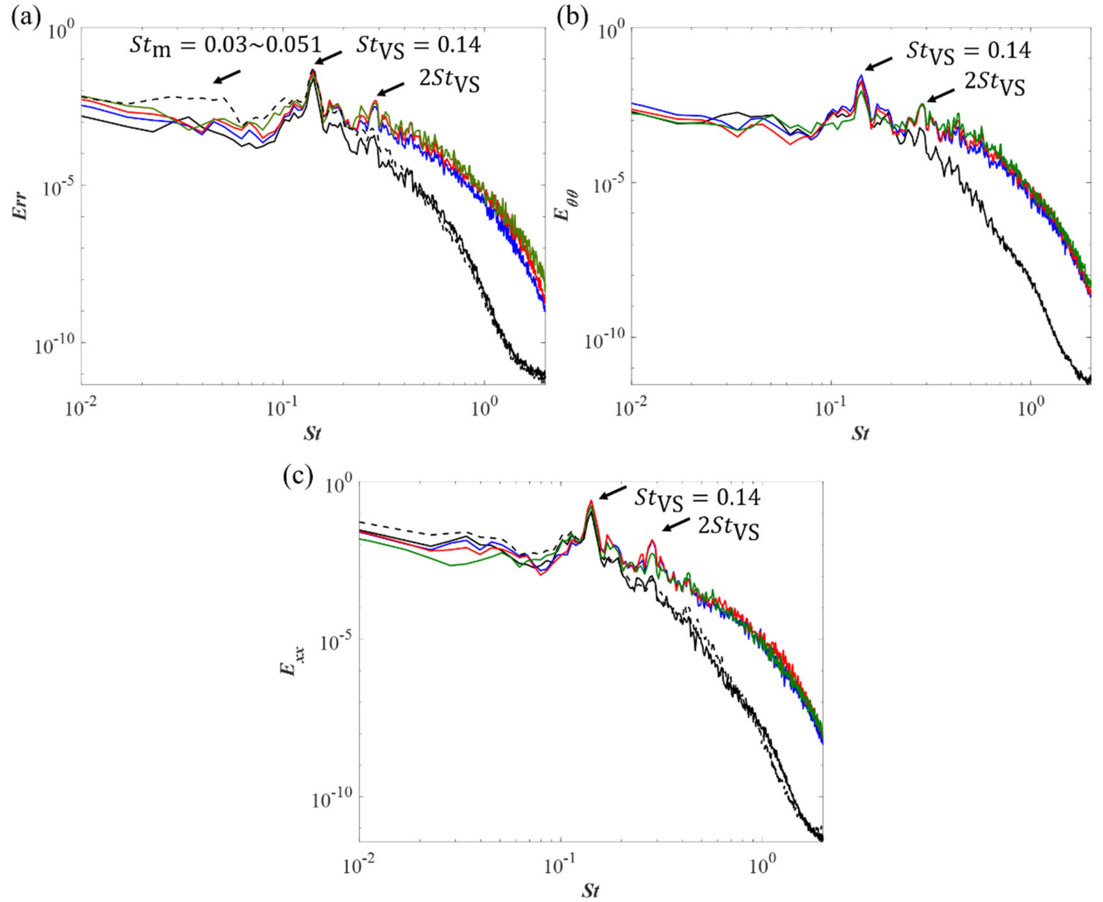

Figure 20 The spectra of the (a) radial velocity; (b) azimuthal velocity and (c) streamwise velocity for $BR = 0.2$ at $Re_s = 490$. (black solid: $(x/d, r/d) = (1,0.6)$; blue: $(x/d, r/d) = (2.4,0.6)$; red: $(x/d, r/d) = (3,0.6)$; green: $(x/d, r/d) = (5,0.6)$; black dashed: $(x/d, r/d) = (1,0.5)$)

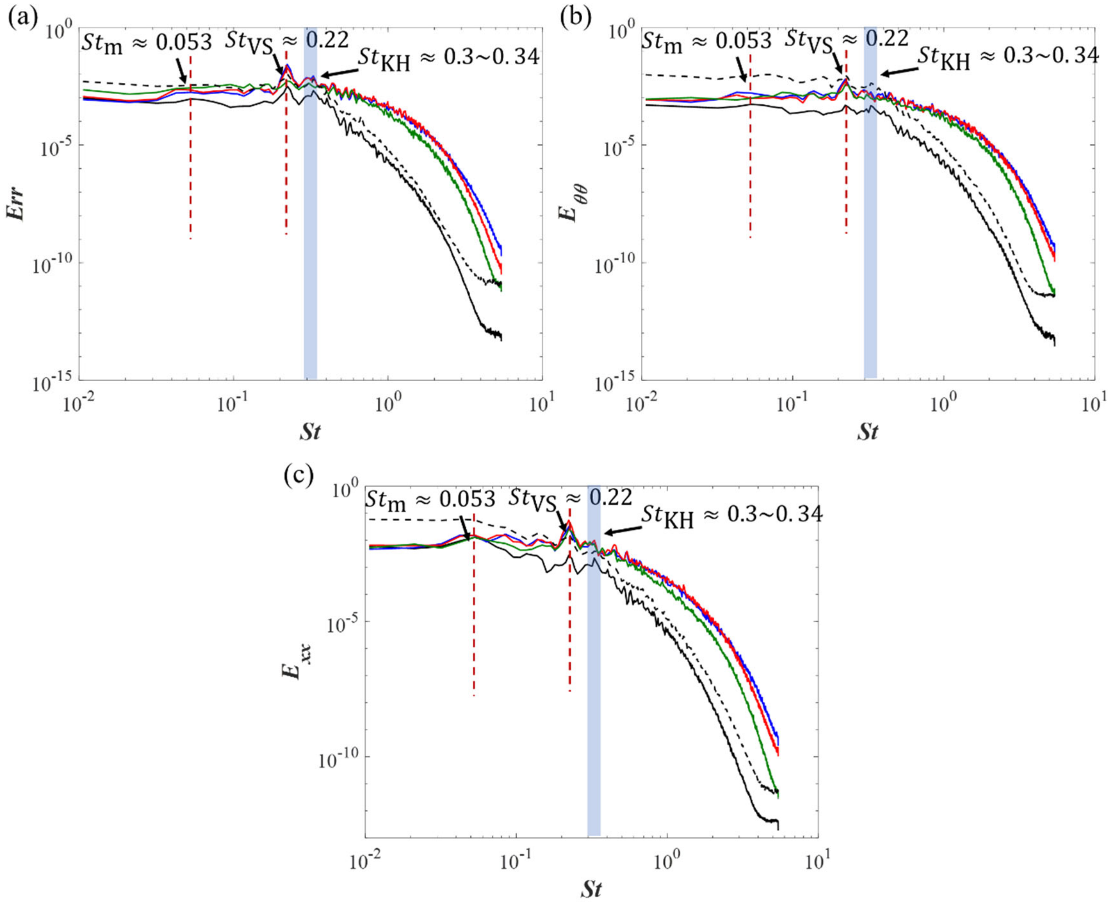

Figure 21 The spectra of the (a) radial velocity; (b) azimuthal velocity and (c) streamwise velocity for $BR = 0.4$ at $Re_s = 920$. (black solid: $(x/d, r/d) = (1,0.6)$; blue: $(x/d, r/d) = (2.4,0.6)$; red: $(x/d, r/d) = (3,0.6)$; green: $(x/d, r/d) = (5,0.6)$; black dashed: $(x/d, r/d) = (1,0.5)$)

Physics of Fluids ACCEPTED MANUSCRIPT

AIP Publishing

This is the author's peer reviewed, accepted manuscript. However, the online version of record will be different from this version once it has been copyedited and typeset.
PLEASE CITE THIS ARTICLE AS DOI:10.1063/5.0017349

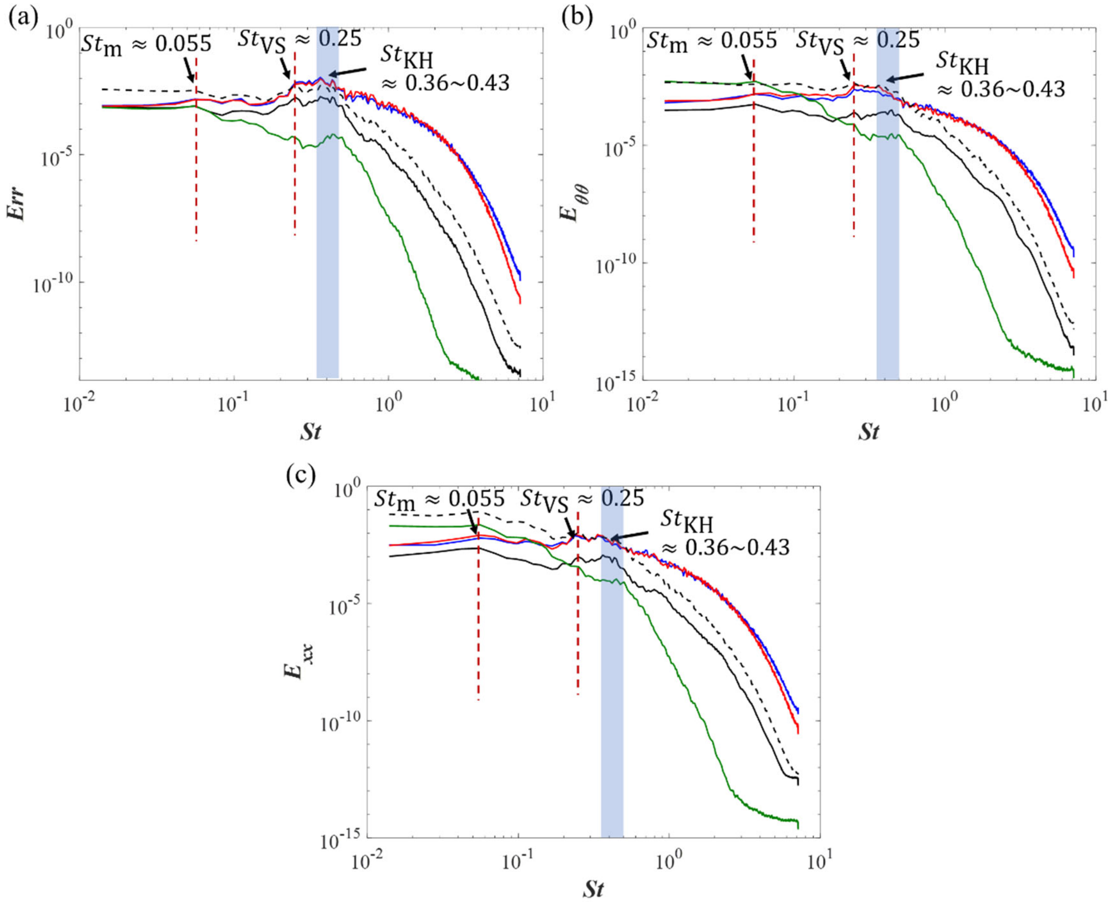

Figure 22 The spectra of the (a) radial velocity; (b) azimuthal velocity and (c) streamwise velocity for $BR = 0.5$ at $Re_s = 1093.8$. (black solid: $(x/d, r/d) = (1,0.6)$; blue: $(x/d, r/d) = (2.4,0.6)$; red: $(x/d, r/d) = (3,0.6)$; green: $(x/d, r/d) = (5,0.6)$; black dashed: $(x/d, r/d) = (1,0.5)$)

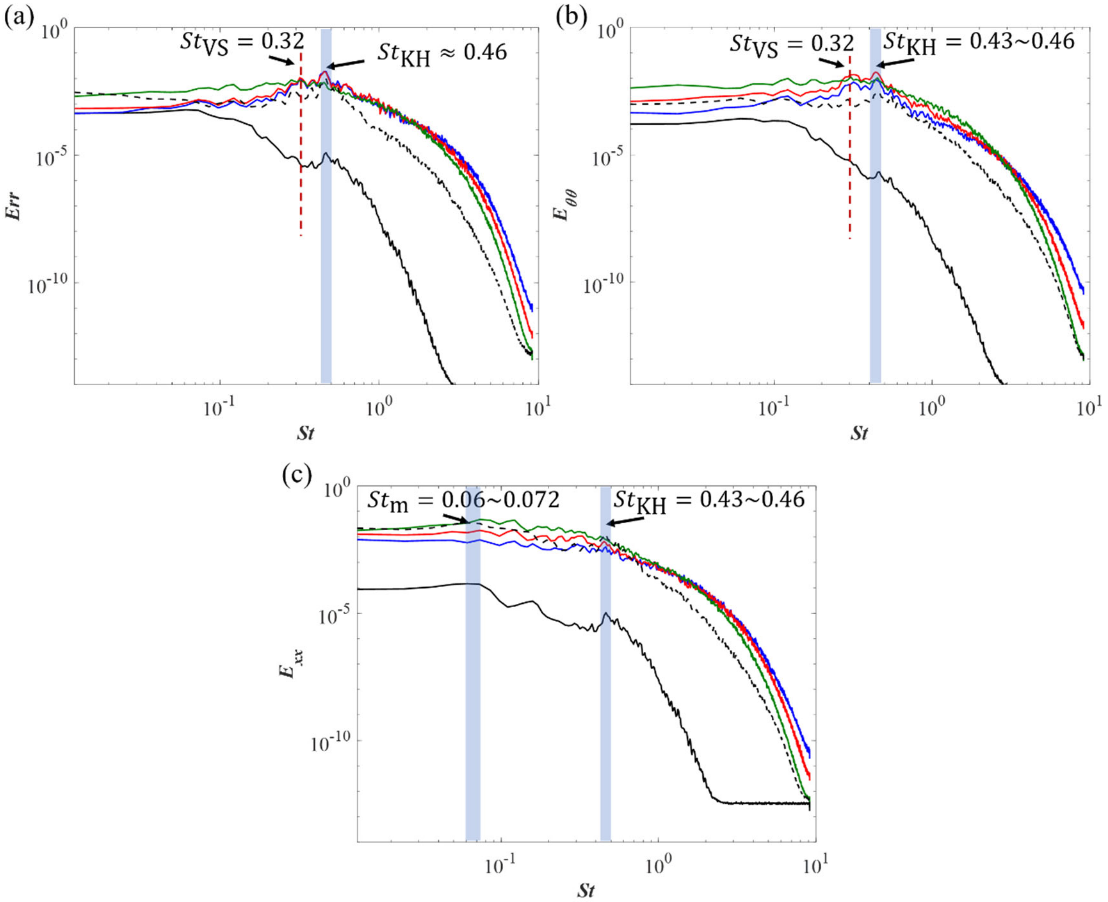

Figure 23 The spectra of the (a) radial velocity; (b) azimuthal velocity and (c) streamwise velocity for $BR = 0.6$ at $Re_s = 1230$. (black solid: $(x/d, r/d) = (1,0.6)$; blue: $(x/d, r/d) = (2.4,0.6)$; red: $(x/d, r/d) = (3,0.6)$; green: $(x/d, r/d) = (5,0.6)$; black dashed: $(x/d, r/d) = (1,0.5)$)

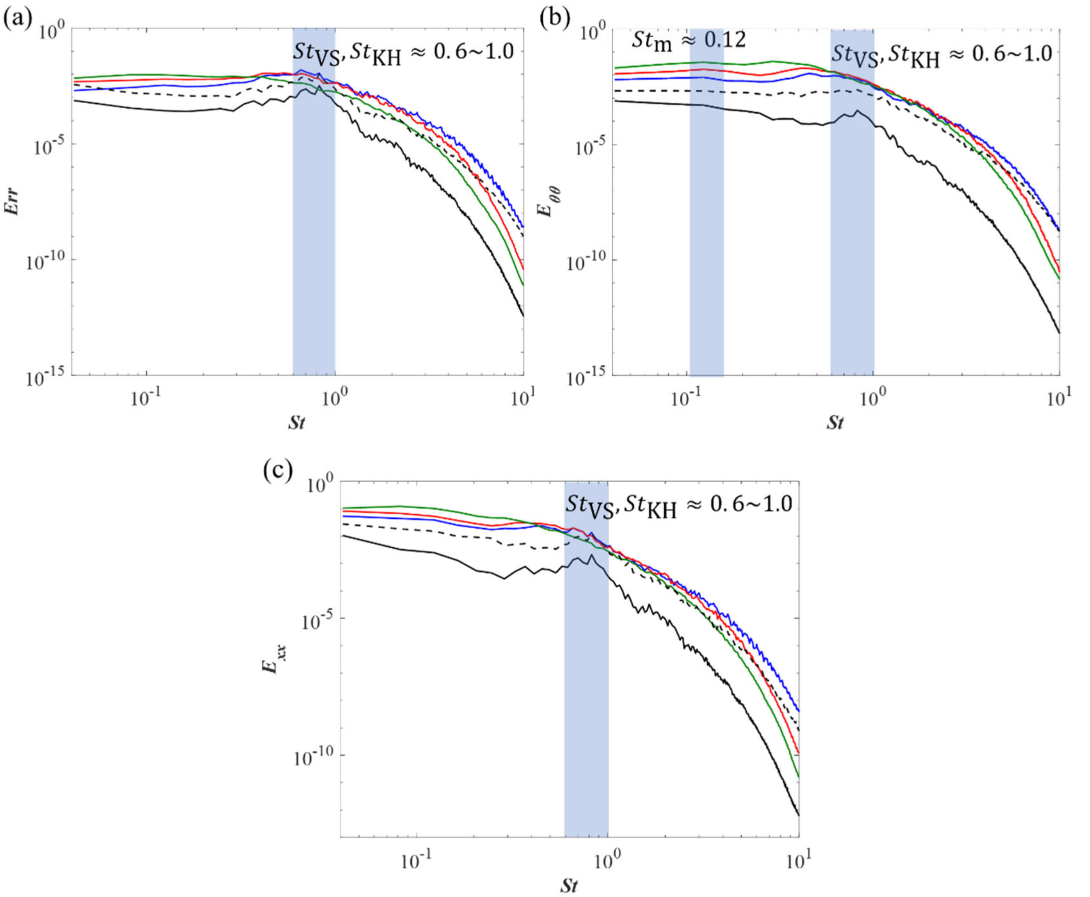

Figure 24 The spectra of the (a) radial velocity; (b) azimuthal velocity and (c) streamwise velocity for $BR = 0.7$ at $Re_s = 1321$. (black solid: $(x/d, r/d) = (1,0.6)$; blue: $(x/d, r/d) = (2.4,0.6)$; red: $(x/d, r/d) = (3,0.6)$; green: $(x/d, r/d) = (5,0.6)$; black dashed: $(x/d, r/d) = (1,0.5)$)

.

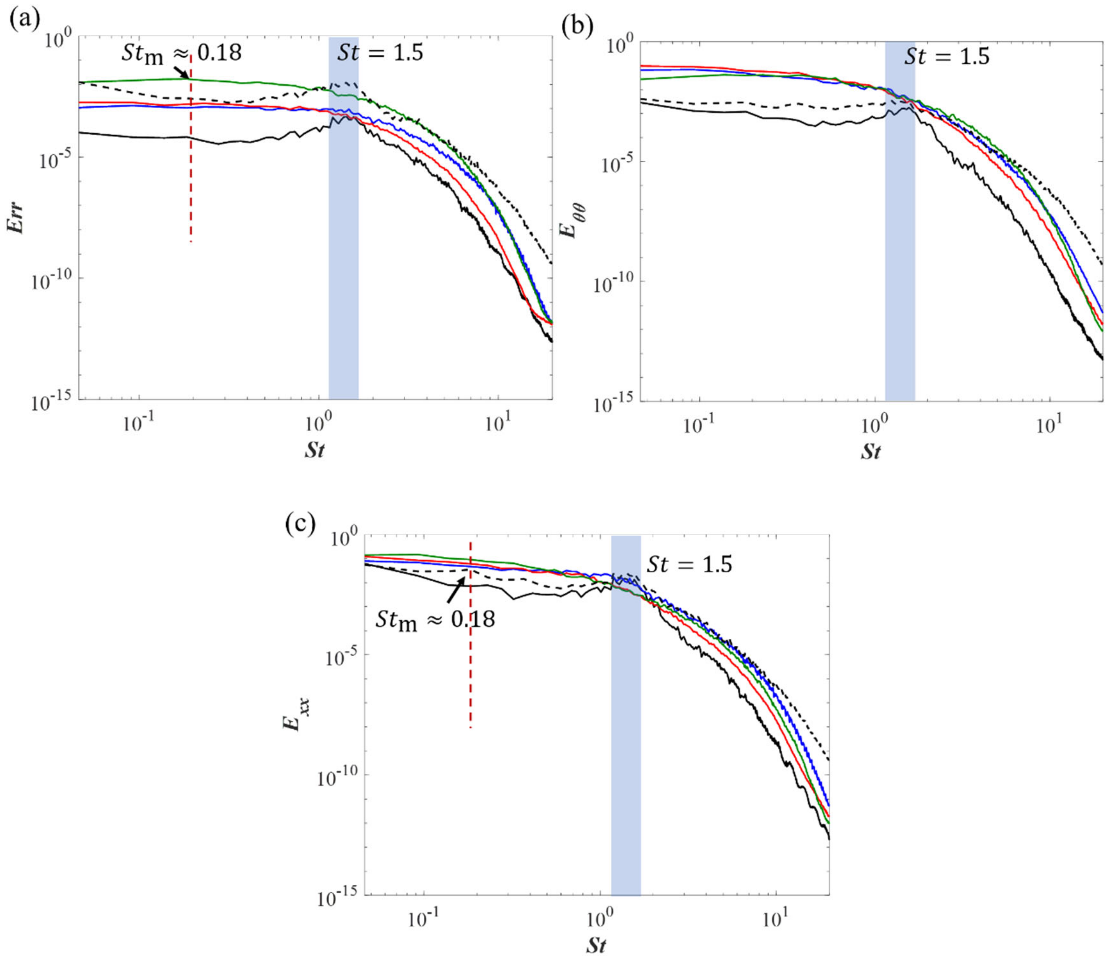

Figure 25 The spectra of the (a) radial velocity; (b) azimuthal velocity and (c) streamwise velocity for $BR = 0.8$ at $Re_s = 1360$. (black solid: $(x/d, r/d) = (1,0.6)$; blue: $(x/d, r/d) = (2.4,0.6)$; red: $(x/d, r/d) = (3,0.6)$; green: $(x/d, r/d) = (5,0.6)$; black dashed: $(x/d, r/d) = (1,0.5)$)

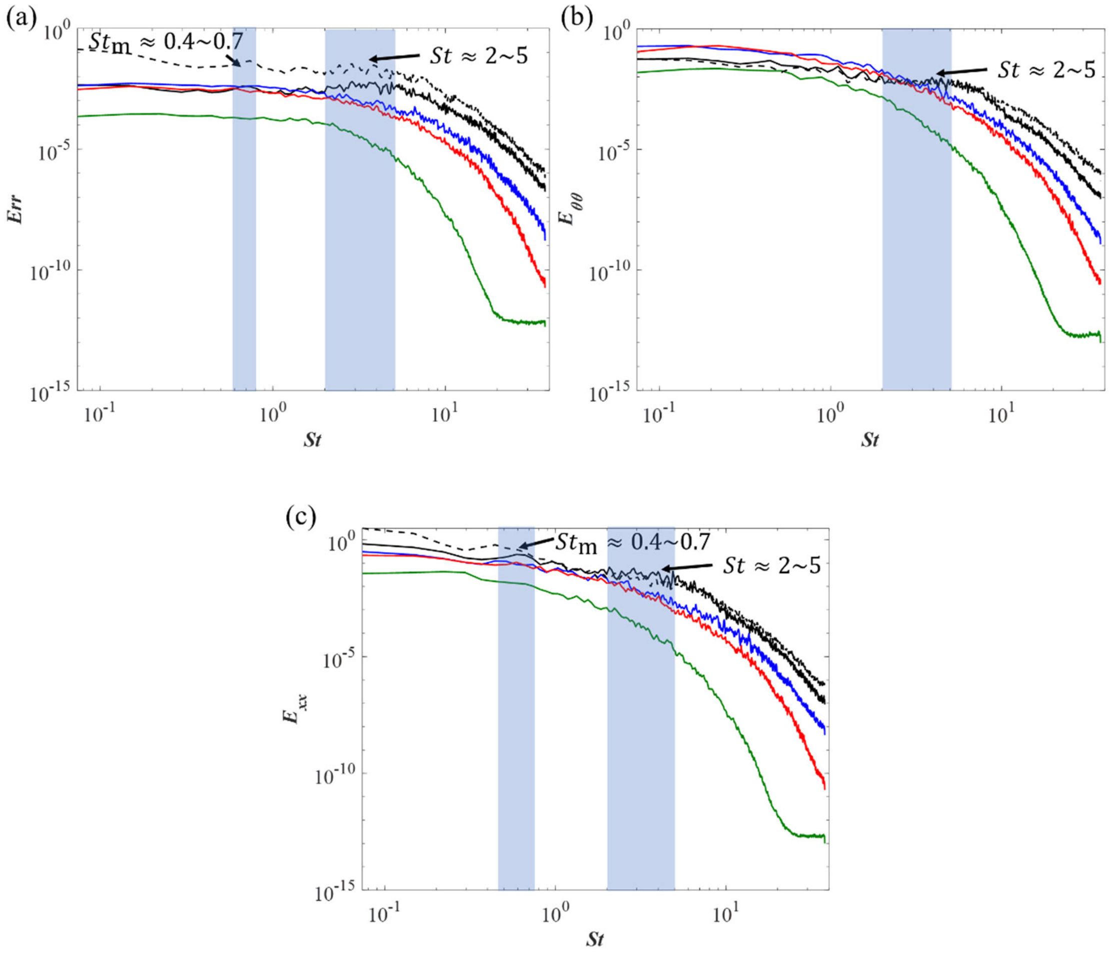

Figure 26 The spectra of the (a) radial velocity; (b) azimuthal velocity and (c) streamwise velocity for $BR = 0.9$ at $Re_s = 1338.75$. (black solid: $(x/d, r/d) = (1{,}0.6)$; blue: $(x/d, r/d) = (2.4{,}0.6)$; red: $(x/d, r/d) = (3{,}0.6)$; green: $(x/d, r/d) = (5{,}0.6)$; black dashed: $(x/d, r/d) = (1{,}0.5)$)

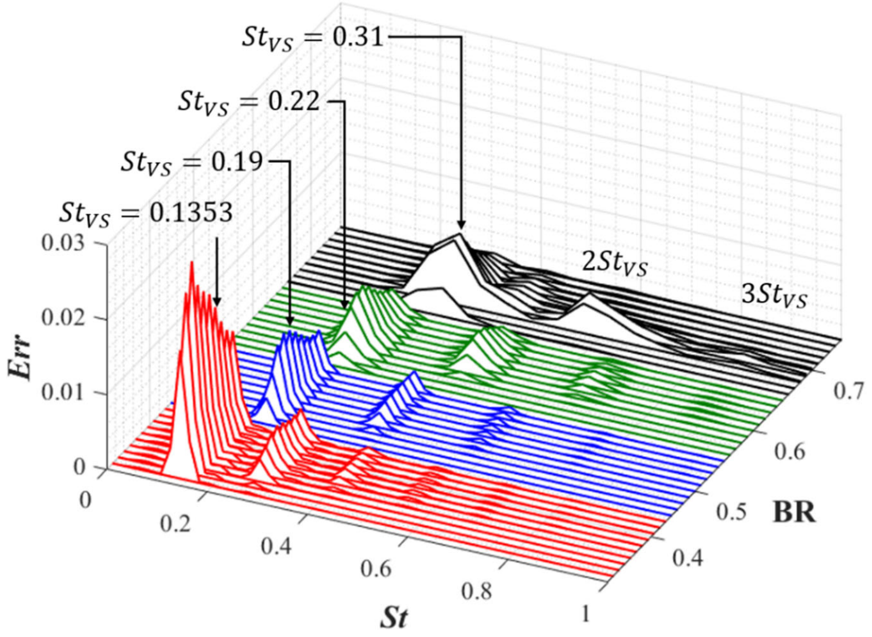

Figure 27 The spectra of the radial velocities at the streamwise locations of $x/d = 0.2\sim2$ spaced by $x/d = 0.2$ for $BR = 0.4$ (red); 0.5 (blue); 0.6 (green); 0.7 (black) at $Re_s = 500$

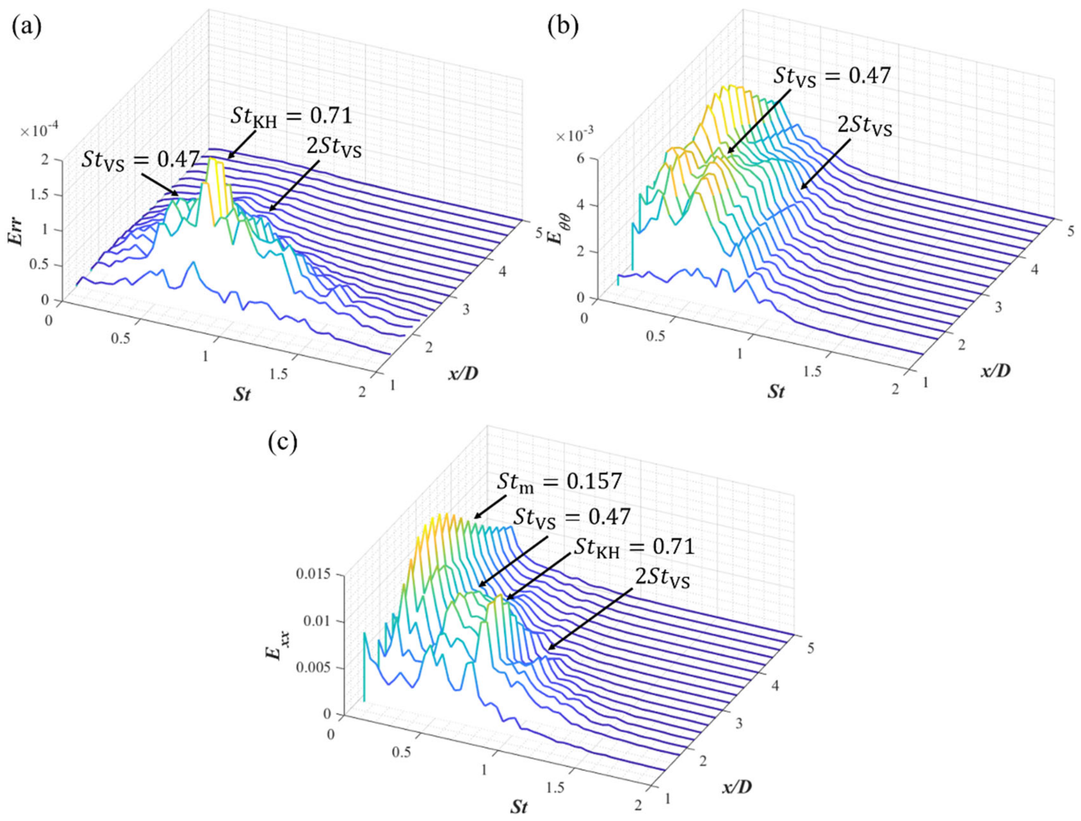

Figure 28 The spectra of the (a) radial velocity; (b) azimuthal velocity and (c) streamwise velocity for $BR = 0.8$ at $Re_s = 500$ at the streamwise locations of $x/d = 0.2\sim5$ spaced by $x/d = 0.2$

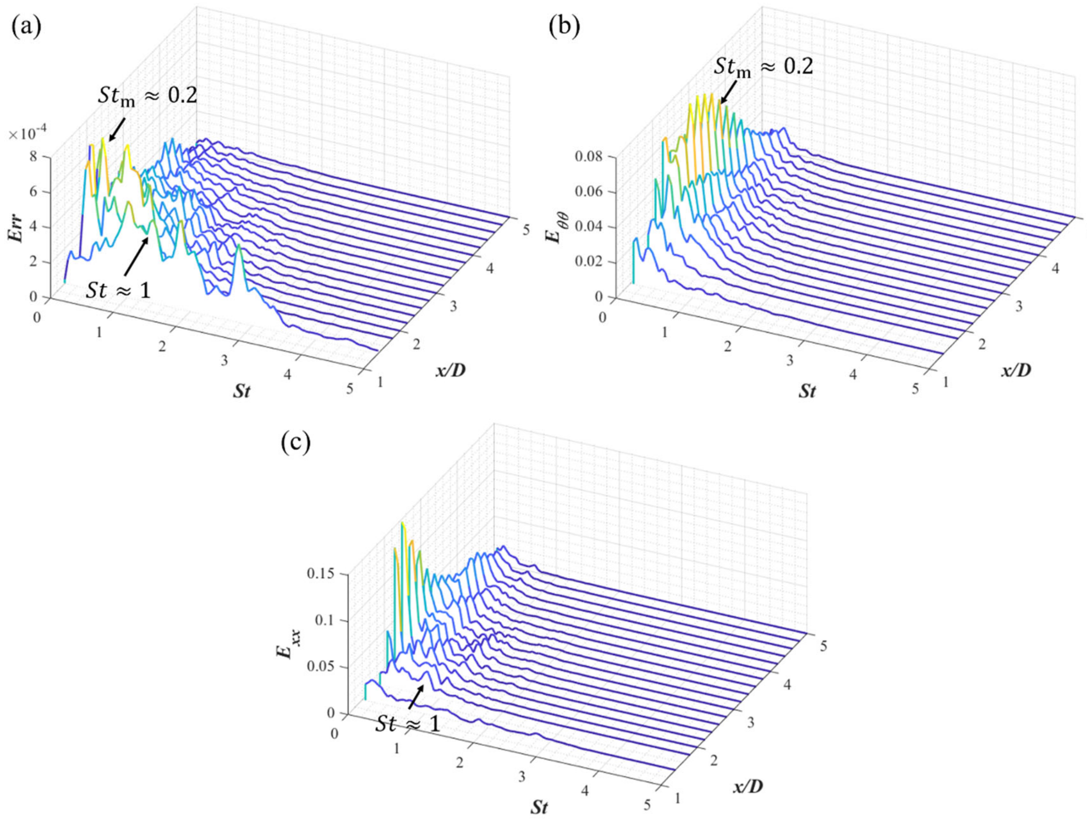

Figure 29 The spectra of the (a) radial velocity; (b) azimuthal velocity and (c) streamwise velocity for $BR = 0.9$ at $Re_s = 500$ at the streamwise locations of $x/d = 0.2\sim 5$ spaced by $x/d = 0.2$

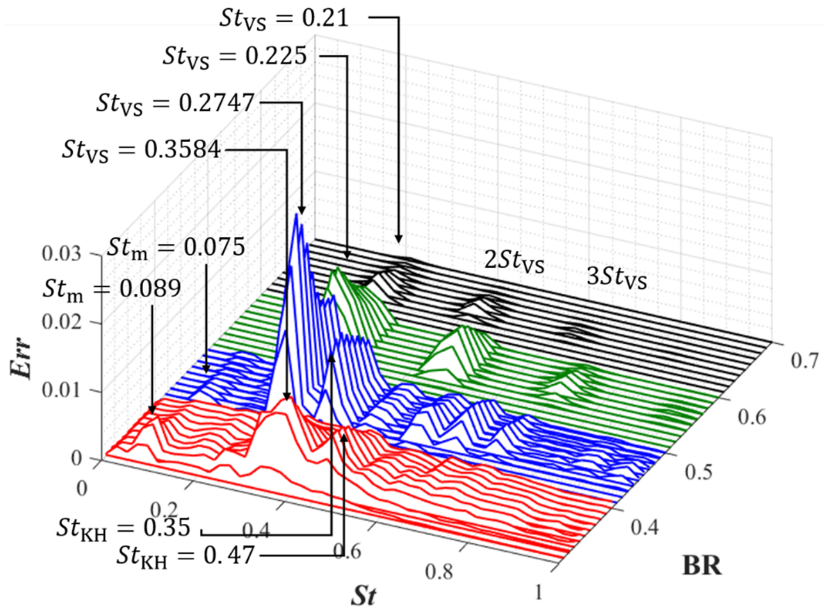

Figure 30 The spectra of the radial velocities at the streamwise locations of $x/d = 0.2{\sim}2$ spaced by $x/d = 0.2$ for $BR = 0.4$ (red); 0.5 (blue); 0.6 (green); 0.7 (black) at $Re_g = 500$

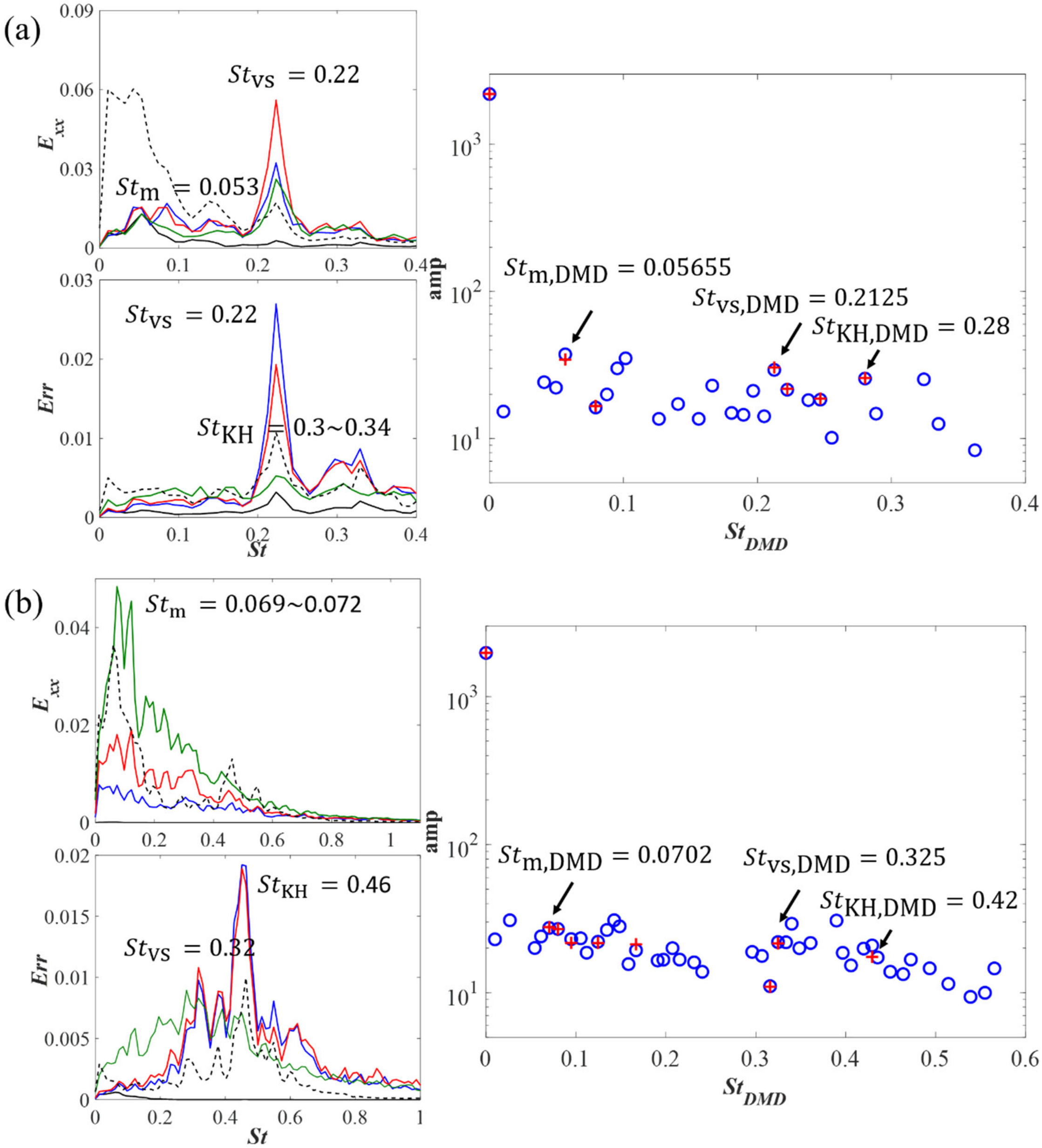
(a)
E_{xx}
St_{vs} = 0.22
St_{m} = 0.053
Err
St_{vs} = 0.22
St_{KH} = 0.3~0.34
St
amp
$St_{\mathrm{m,DMD}}$ = 0.05655
$St_{\mathrm{vs,DMD}}$ = 0.2125
$St_{\mathrm{KH,DMD}}$ = 0.28
St_{DMD}
(b)
E_{xx}
St_{m} = 0.069~0.072
Err
St_{KH} = 0.46
St_{vs} = 0.32
St
amp
$St_{\mathrm{m,DMD}}$ = 0.0702
$St_{\mathrm{vs,DMD}}$ = 0.325
$St_{\mathrm{KH,DMD}}$ = 0.42
St_{DMD}

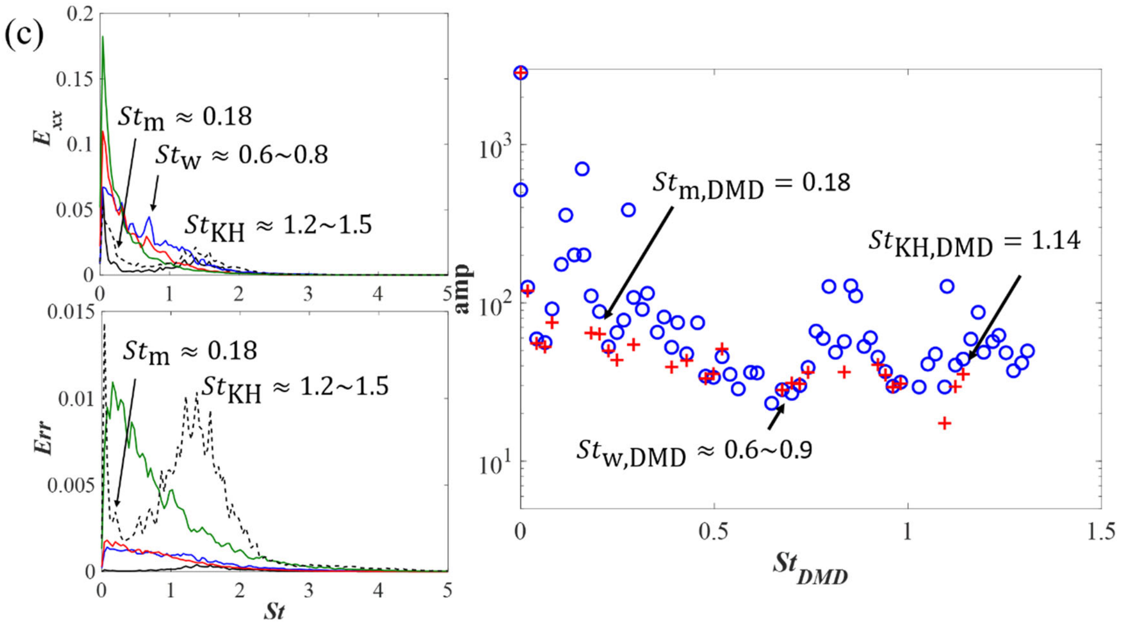

Figure 31 The frequency spectra of the DMD modes for (a) $BR = 0.4$; (b) 0.6 and (c) 0.8 with the dominant modes denoted by the arrows (Blue circles: the modes obtained by using the original DMD method; red crossings: the modes obtained by applying sparsity-promoted algorithm)

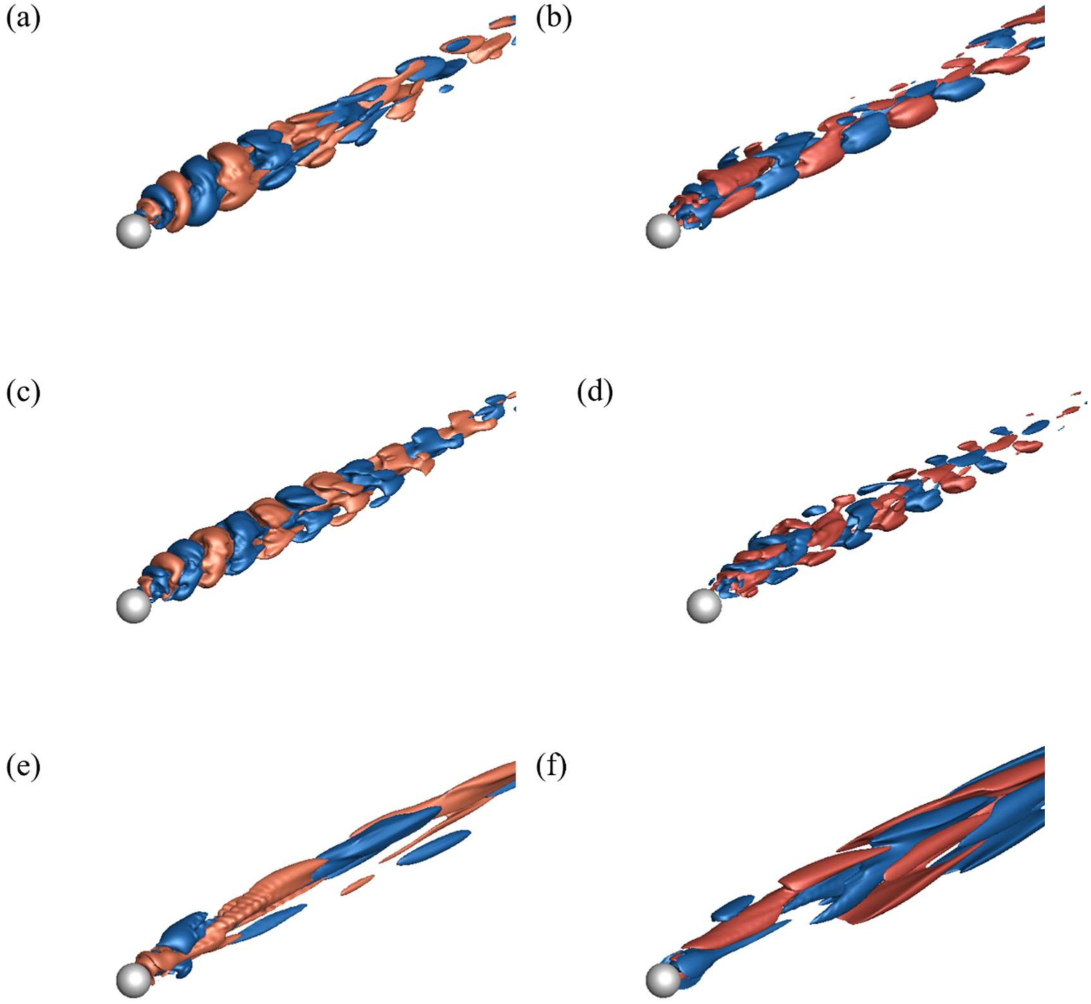

Figure 32 Iso-surfaces of $u_r/U_m = \pm 0.0002$ for the radial velocity (a, c, e) and $u/U_m = \pm 0.0005$ for the streamwise velocity (b, d, f) of the three dominant DMD modes of $BR = 0.4$: (a, b) vortex shedding mode; (c, d) KH instability mode; (e, f) low-frequency mode

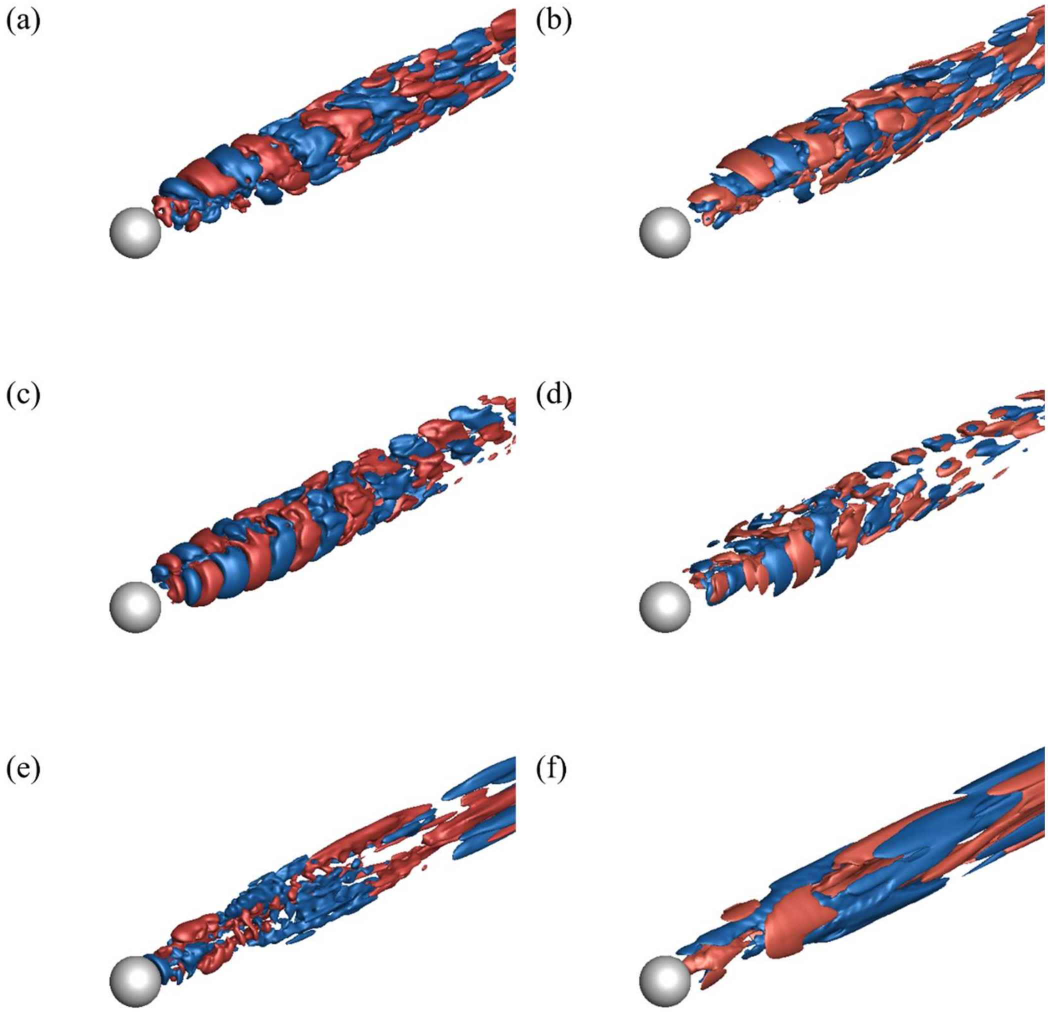

Figure 33 Iso-surfaces of $u_r/U_m = \pm 0.0002$ for the radial velocity (a, c, e) and $u/U_m = \pm 0.0005$ for the streamwise velocity (b, d, f) of the three dominant DMD modes of $BR = 0.6$: (a, b) vortex shedding mode; (c, d) KH instability mode; (e, f) low-frequency mode

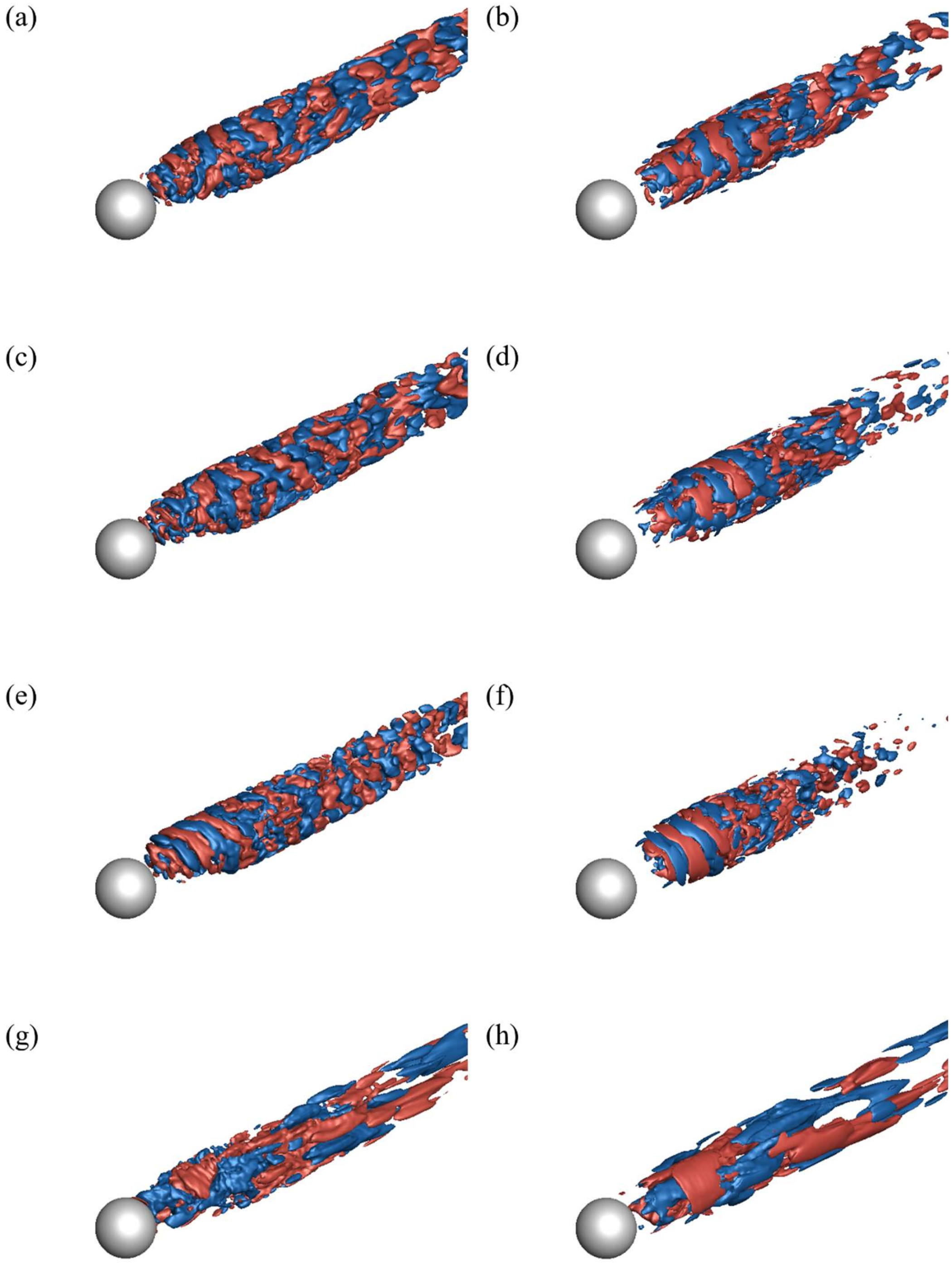

Figure 34 Iso-surfaces of $u_r/U_m = \pm 0.0002$ for the radial velocity (a, c, e, g) and $u/U_m = \pm 0.0005$ for the streamwise velocity (b, d, f, h) of the four dominant DMD modes of $BR = 0.8$: (a, b) DMD modes at $St_{\text{DMD}} = 0.74$; (c, d) DMD modes at $St_{\text{DMD}} = 0.835$; (e, f) KH instability mode; (g, h) low-frequency mode

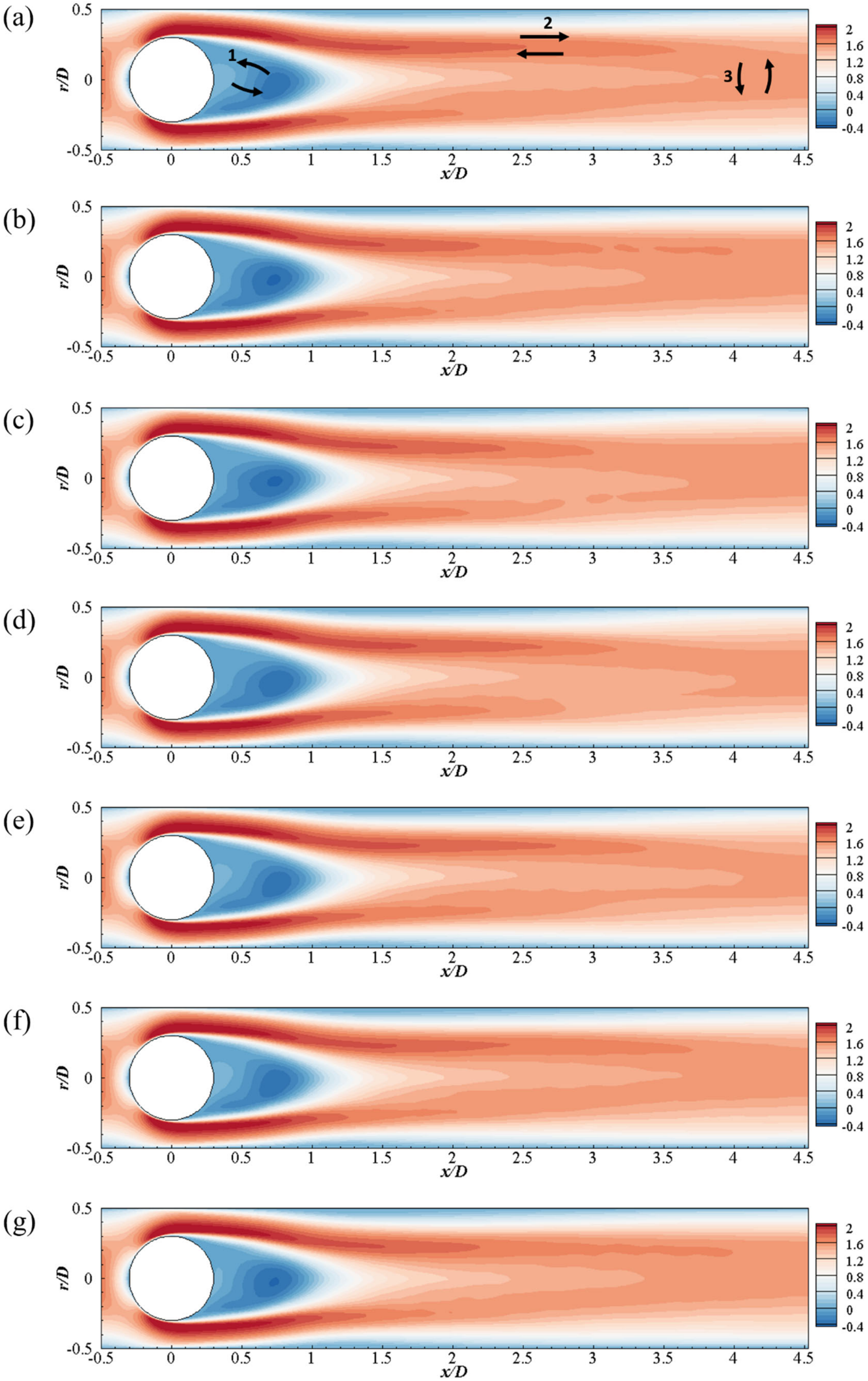
(a)
(b)
(c)
(d)
(e)
(f)
(g)
1
2
3
r/D
x/D
0.5
0
-0.5
-0.5
0
0.5
1
1.5
2
2.5
3
3.5
4
4.5
2
1.6
1.2
0.8
0.4
0
-0.4

(h)

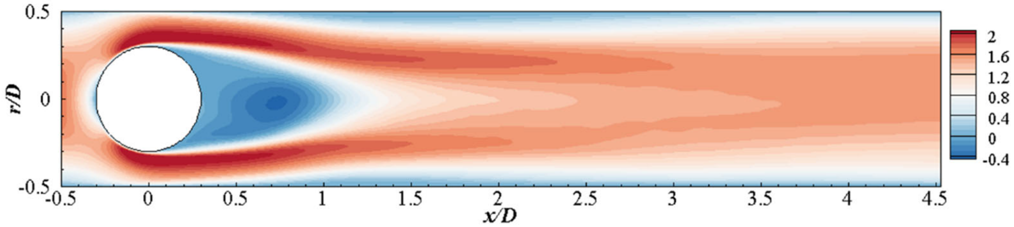

Figure 35 The streamwise velocity of the mean flow with the superposition of the low frequency DMD mode at eight instants on the XY slice at (a) $tU_\infty/d = 579.47$; (b) $tU_\infty/d = 582.2$; (c) $tU_\infty/d = 584.93$; (d) $tU_\infty/d = 587.66$; (e) $tU_\infty/d = 590.39$; (f) $tU_\infty/d = 593.12$; (g) $tU_\infty/d = 595.85$; (h) $tU_\infty/d = 595.58$

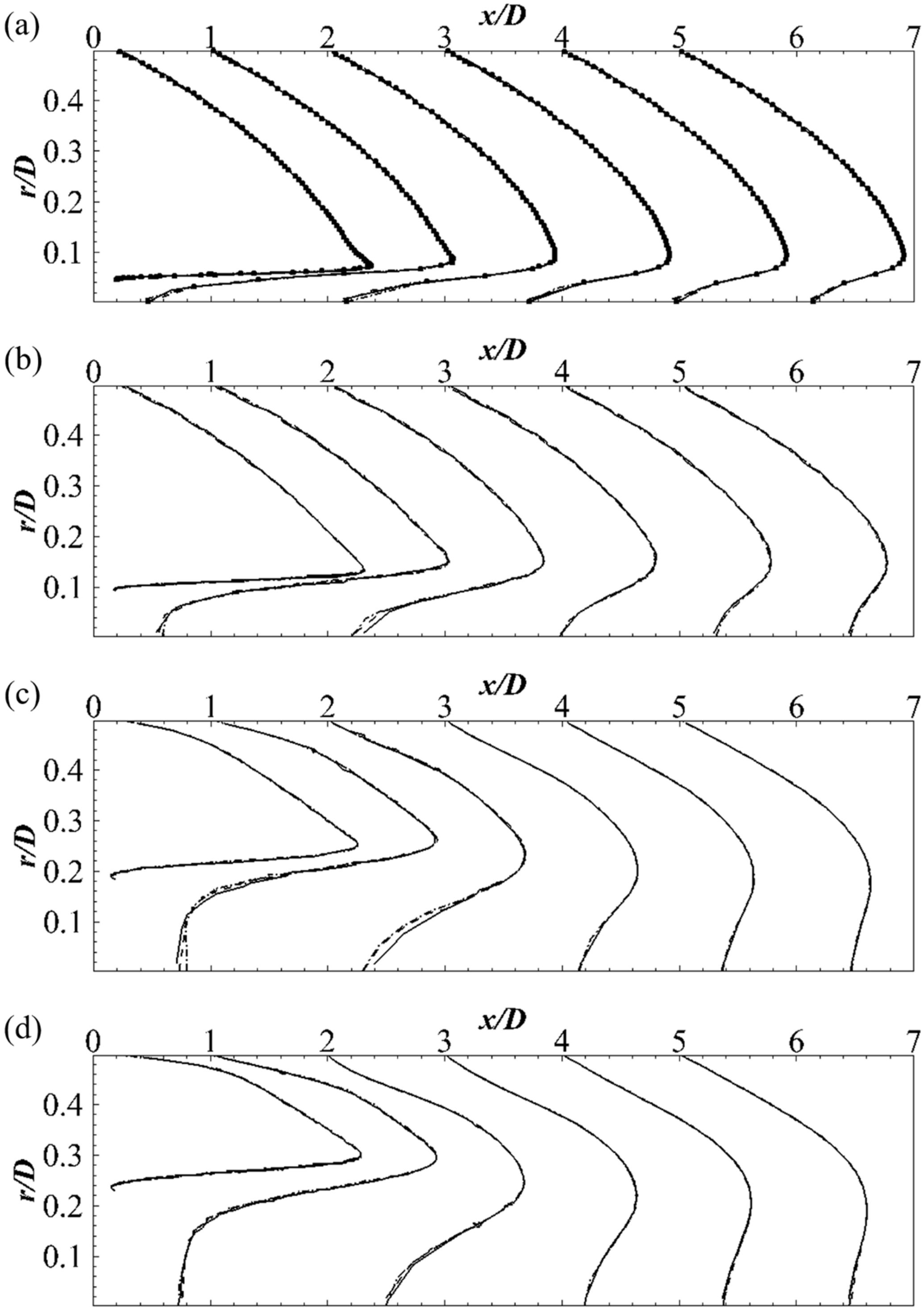
(a)
x/D
0
1
2
3
4
5
6
7
r/D
0.4
0.3
0.2
0.1
(b)
x/D
0
1
2
3
4
5
6
7
r/D
0.4
0.3
0.2
0.1
(c)
x/D
0
1
2
3
4
5
6
7
r/D
0.4
0.3
0.2
0.1
(d)
x/D
0
1
2
3
4
5
6
7
r/D
0.4
0.3
0.2
0.1

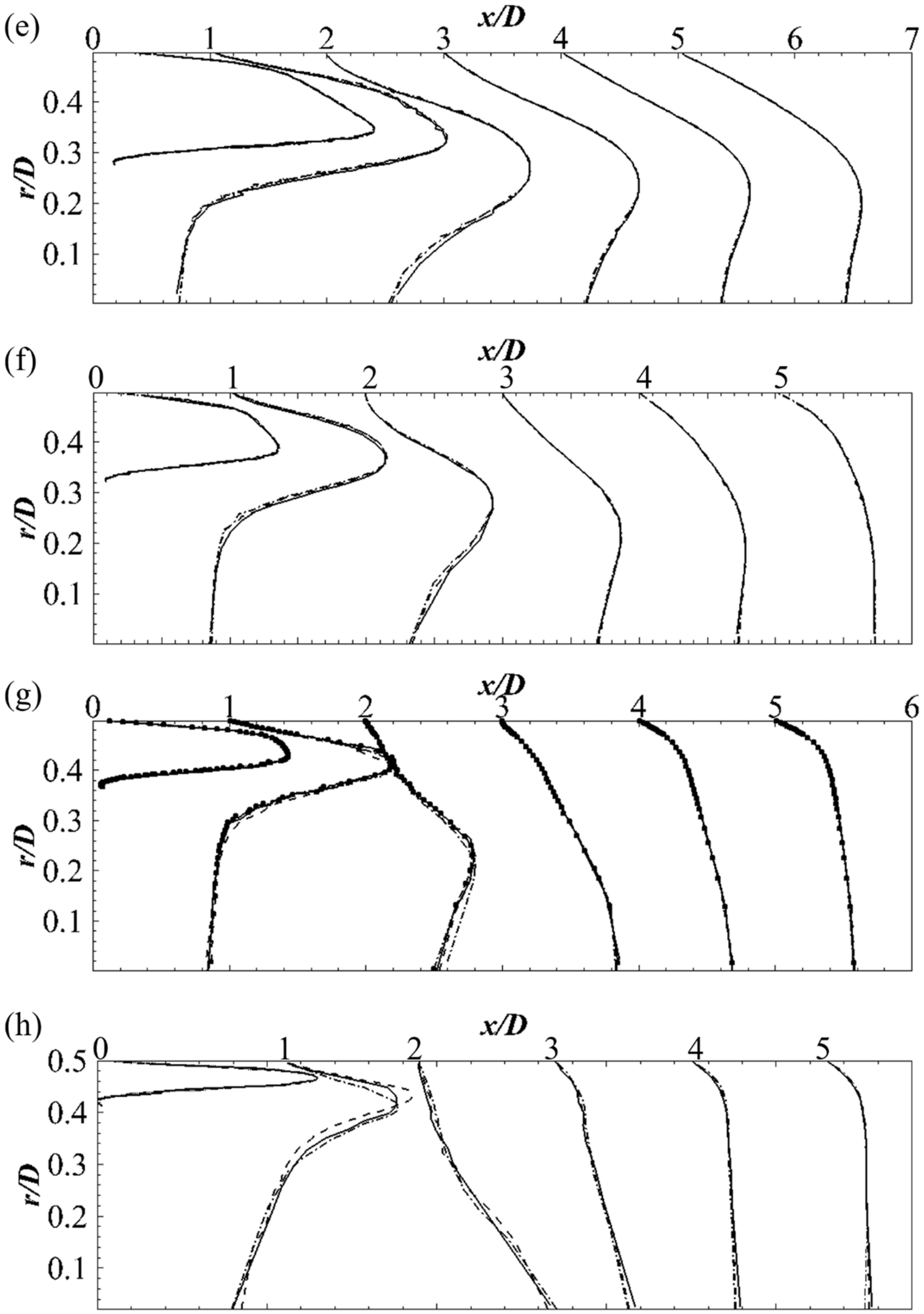

Figure 36 Azimuthal- and time-averaged streamwise profiles at the streamwise locations of $x/d = 0.2, 1, 2, 3, 4, 5$ in the wake flow behind the sphere for different grid resolutions: Case 1: Solid lines; Case 2: Dashed; Case 3: Dash-dotted; Case 4: Black circles with $BR =$ (a) 0.1; (b) 0.2; (c) 0.4; (d) 0.5; (e) 0.6; (f) 0.7; (g) 0.8; (h) 0.9

Physics of Fluids ACCEPTED MANUSCRIPT

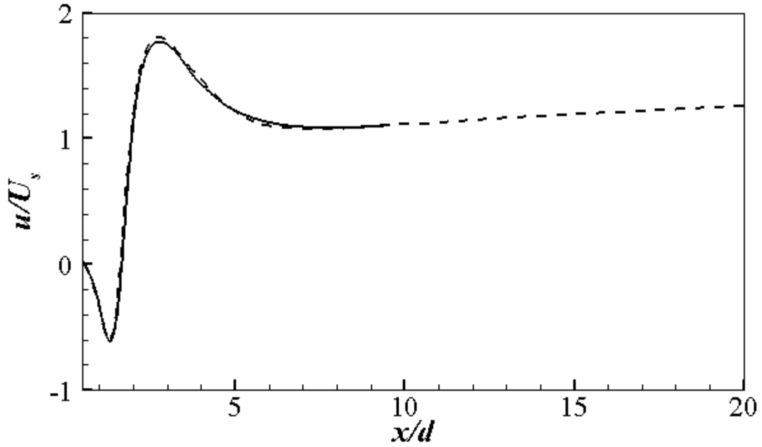

Figure 37 The time-averaged streamwise velocity along the centerline of the pipe (Solid lines: H3; Dashed: H3L)

Physics of Fluids ACCEPTED MANUSCRIPT

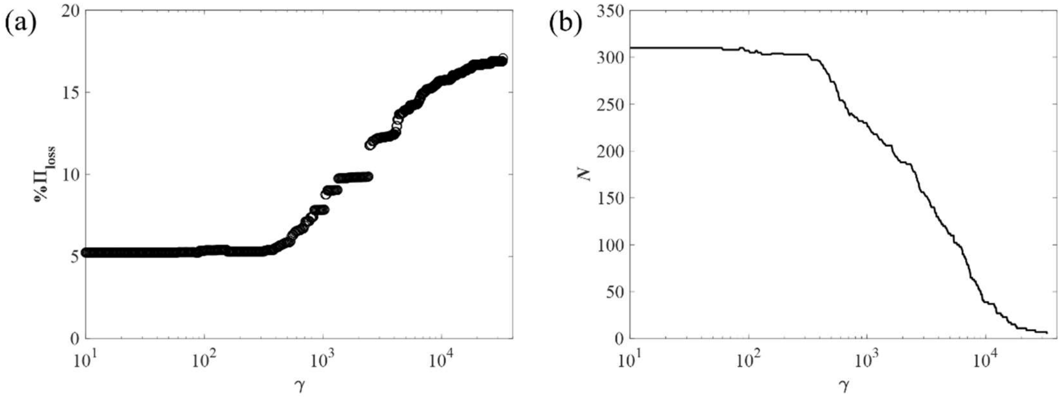

Figure 38 (a) The approximation loss Π_{loss} with γ; (b) the number of modes N retain in Eq (B1) with γ

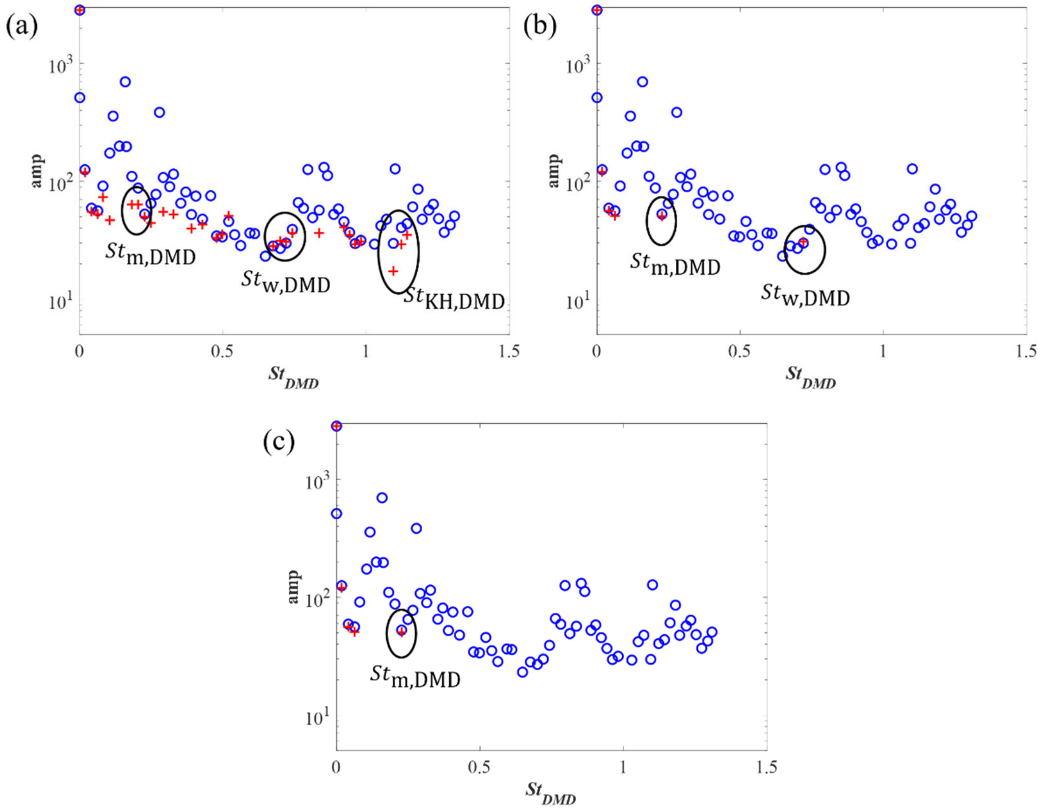

Figure 39 The frequency spectra of the DMD modes obtained by using the original standard DMD method (Blue circles) and the SPDMD (red crossings) with different number of modes (a) $N = 57$; (b) $N = 13$; (c) $N = 9$

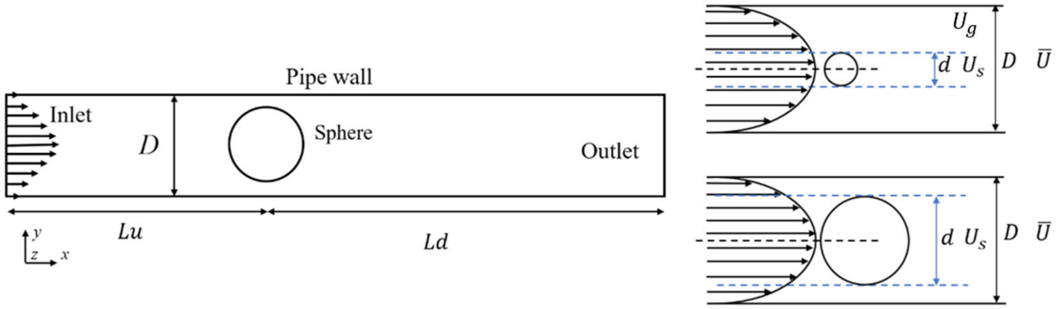
Pipe wall
Inlet
D
Sphere
Outlet
Lu
Ld
y
z
x
U_g
d
U_s
D
$\overline{U}$
d
U_s
D
$\overline{U}$

Figure 1 Computational domain and an example view of the sphere with $BR = 0.4$ and $BR = 0.8$.

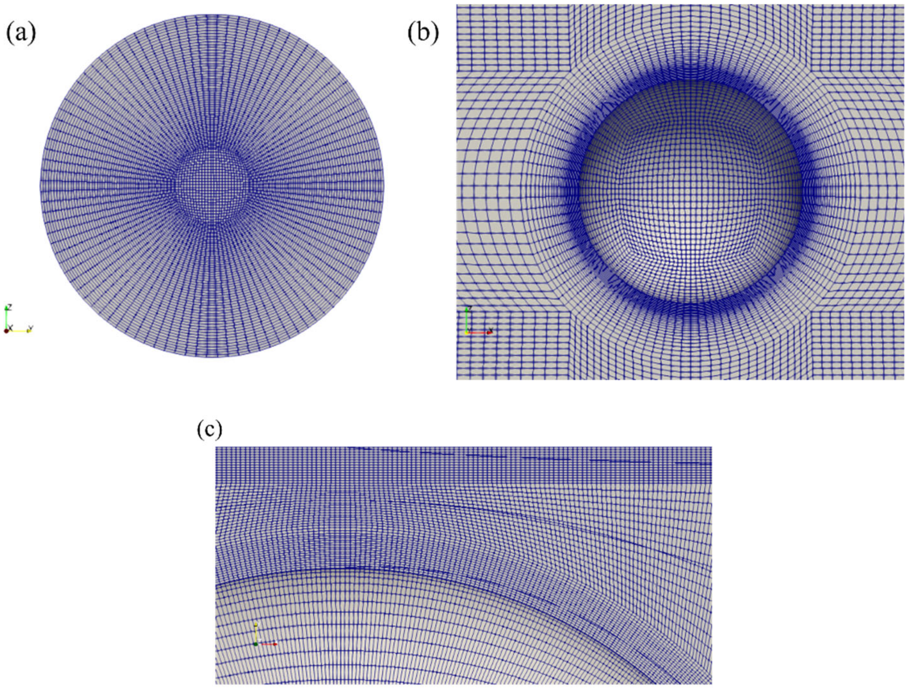

Figure 2 Computational grids. (a) YZ view at the inlet; (b) XZ view around the sphere for $BR = 0.2$ and (c) XZ view around the sphere and near the pipe wall for $BR = 0.8$

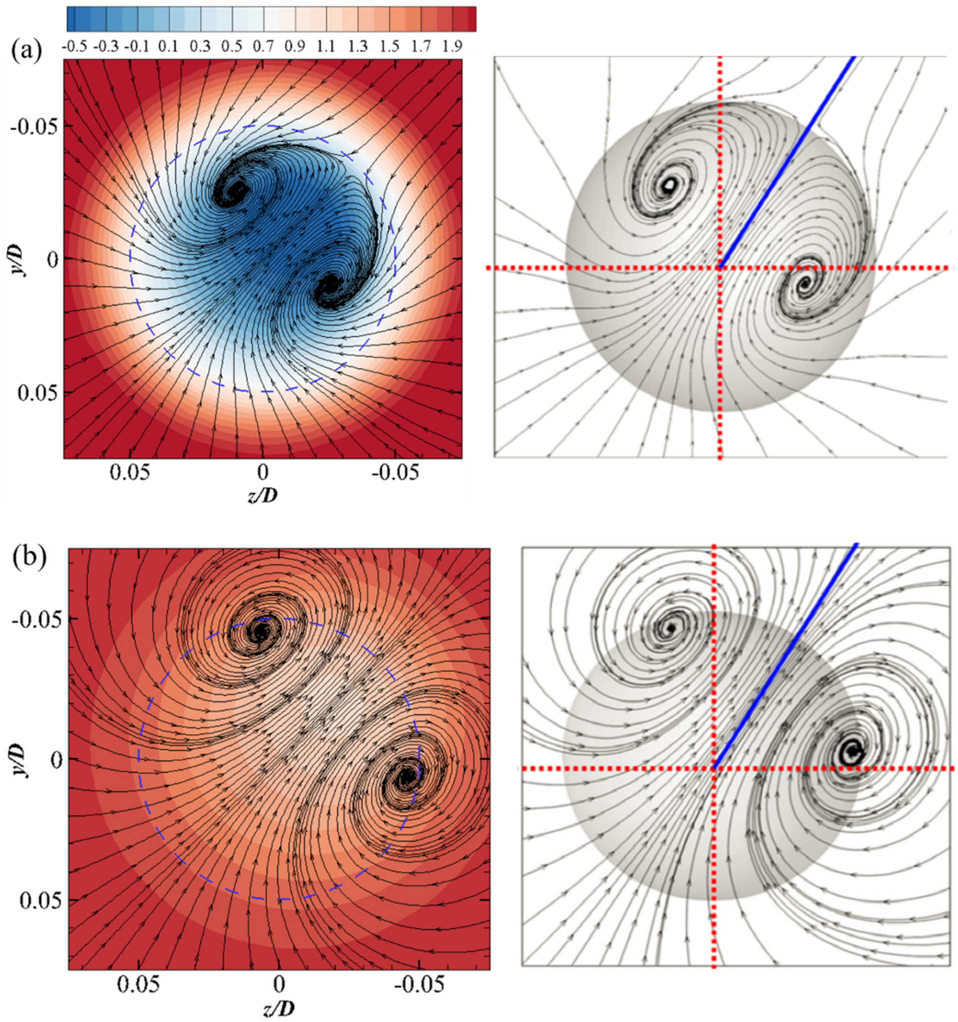

Figure 3 Time-averaged streamlines on two constant x/d planes at (a) $x/d = 1$ and (b) $x/d = 7$ for $BR = 0.1$ at $Re_s = 250$ for the sphere subjected to a uniform flow of the present study (Left. The blue dashed lines indicate the sphere) compared with those in Tiwari et al. [61] (Right) at the same streamwise locations. The color contours denote the value of the time-averaged streamwise velocity.

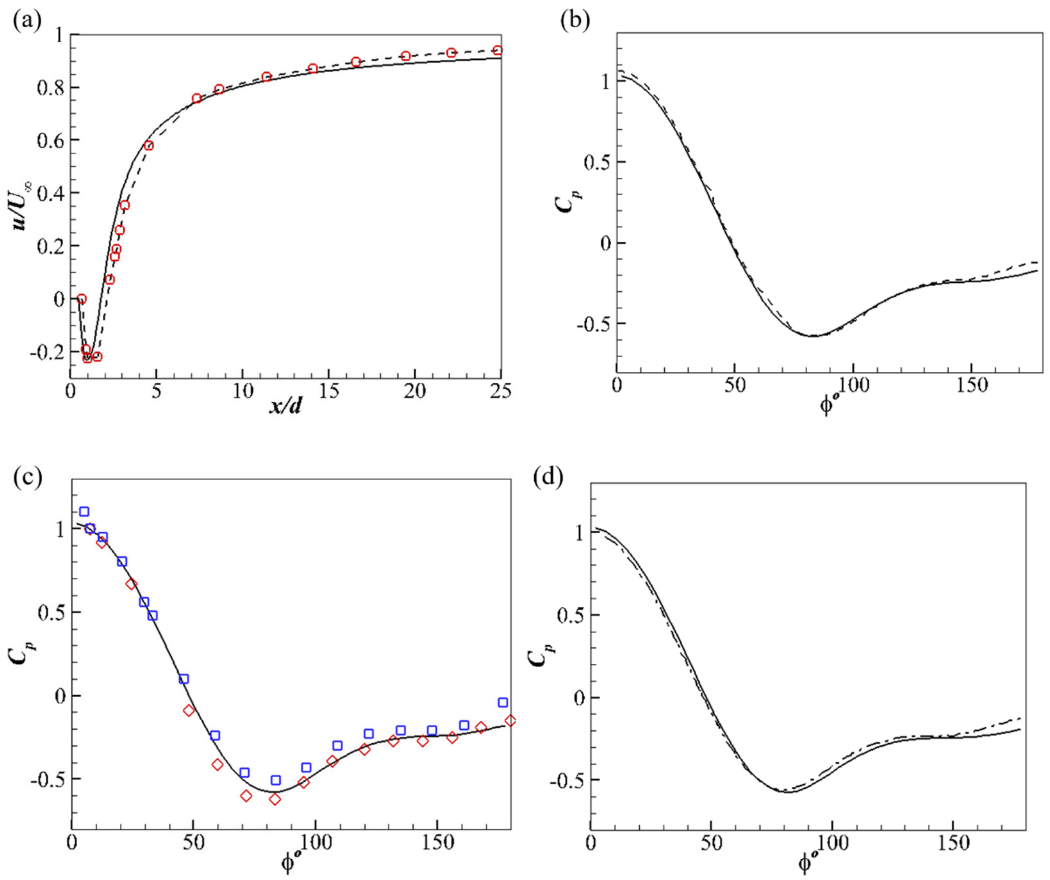

Figure 4 (a) The time-averaged streamwise velocity along the centerline of the pipe at $Re_s = 300$; the pressure distributions on the sphere at (b) $Re_s = 250$; (c) $Re_s = 300$; (d) $Re_s = 350$ (solid lines: present study; red circles: experimental data in Wu and Faeth[67] at $Re_s = 280$; dashed: DNS data in Tomboulides and Orszag[62] at $Re_s = 200$; red diamond: Le Clair et al.[25] at $Re_s = 300$; blue square: Magnaudet et al.[29] at $Re_s = 300$; Dash-dotted: Bagchi et al.[2] at $Re_s = 350$)

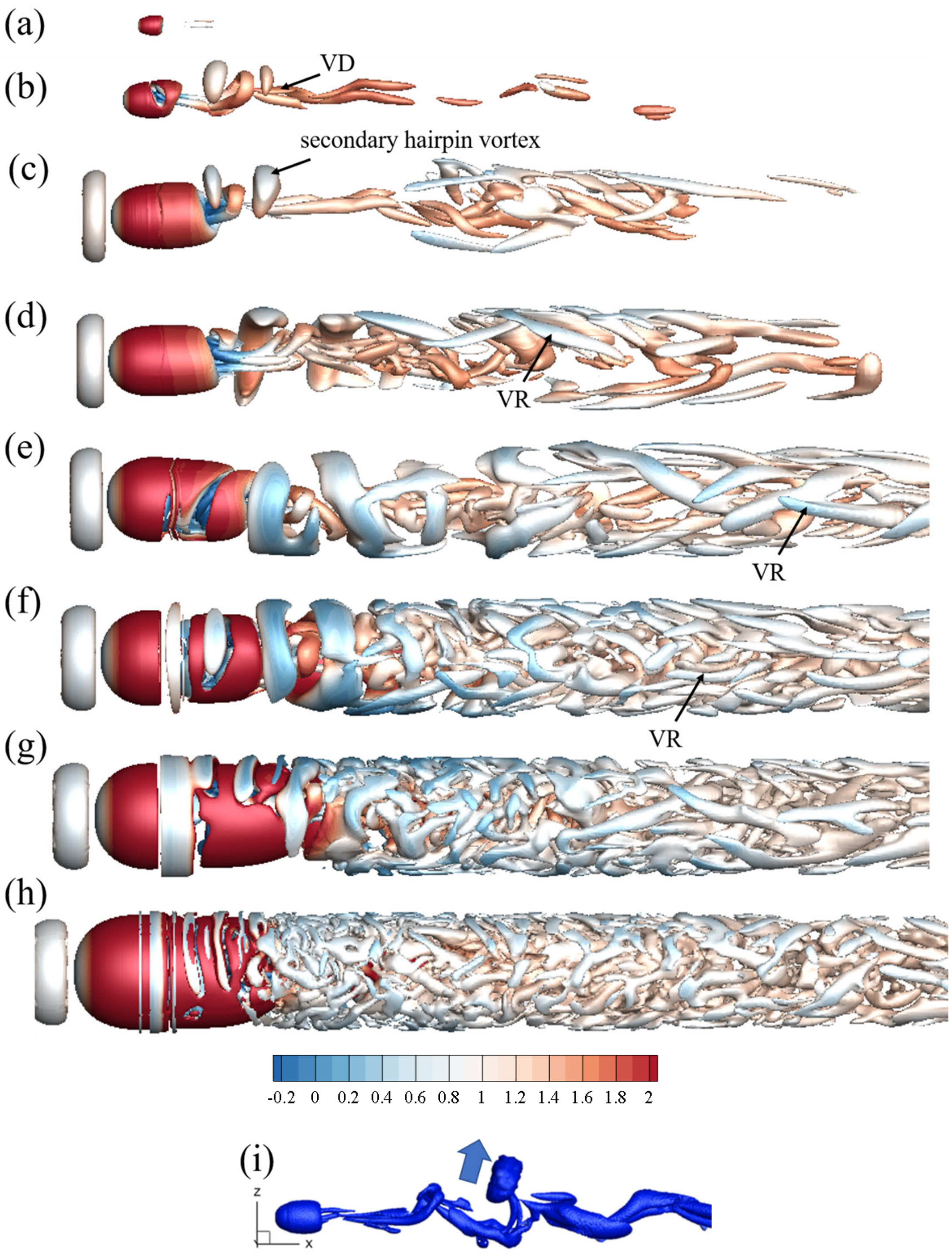
(a)
(b)
VD
secondary hairpin vortex
(c)
(d)
VR
(e)
VR
(f)
VR
(g)
(h)
-0.2 0 0.2 0.4 0.6 0.8 1 1.2 1.4 1.6 1.8 2
(i)
z
x

Figure 5 Instantaneous iso-surfaces of $Q = 2$ colored by the time-averaged streamwise velocity at $Re_p = 1250$ for (a) $BR = 0.1$; (b) $BR = 0.2$; (c) $BR = 0.4$; (d) $BR = 0.5$; (e) $BR = 0.6$; (f) $BR = 0.7$; (g) $BR = 0.8$; (h) $BR = 0.9$; (i) $Re_s = 500$ reprint of Tiwari et al.[61]

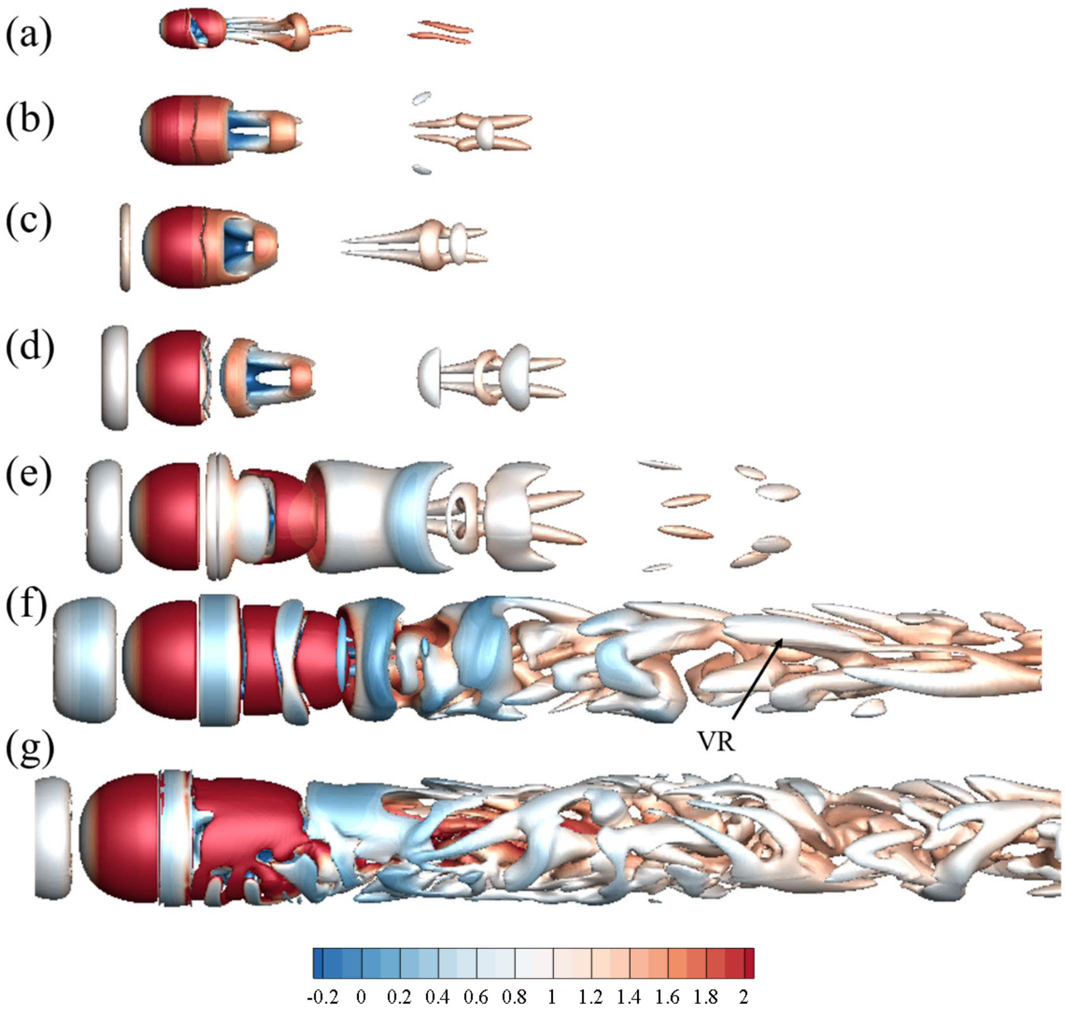
(a)
(b)
(c)
(d)
(e)
(f)
VR
(g)
-0.2
0
0.2
0.4
0.6
0.8
1
1.2
1.4
1.6
1.8
2

Figure 6 Instantaneous iso-surfaces of $Q^* = 1$ colored by the time-averaged streamwise velocity at $Re_s = 500$ for (a) $BR = 0.2$; (b) $BR = 0.4$; (c) $BR = 0.5$; (d) $BR = 0.6$; (e) $BR = 0.7$; (f) $BR = 0.8$; (g) $BR = 0.9$

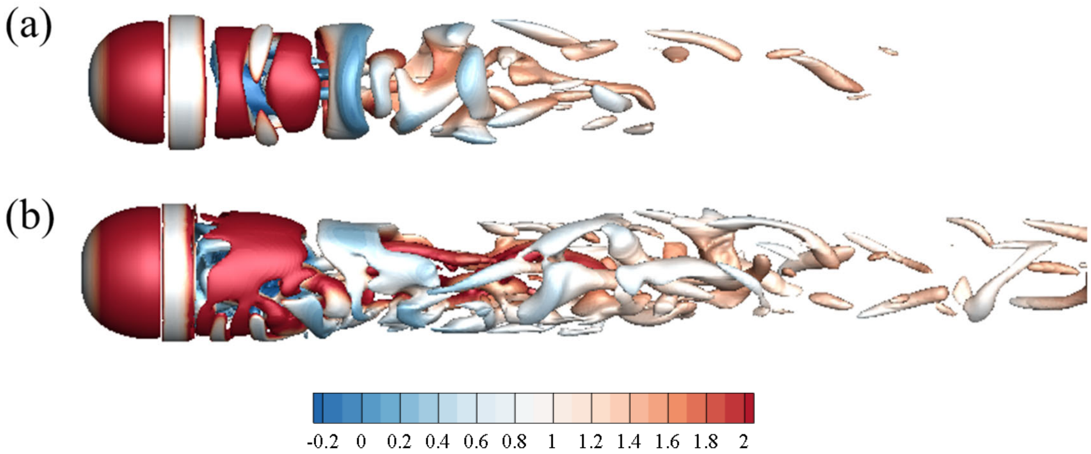
(a)
(b)
-0.2
0
0.2
0.4
0.6
0.8
1
1.2
1.4
1.6
1.8
2

Figure 7 Instantaneous iso-surfaces of $Q^* = 10$ colored by the time-averaged streamwise velocity at $Re_s = 500$ for (a) $BR = 0.8$ and (b) $BR = 0.9$

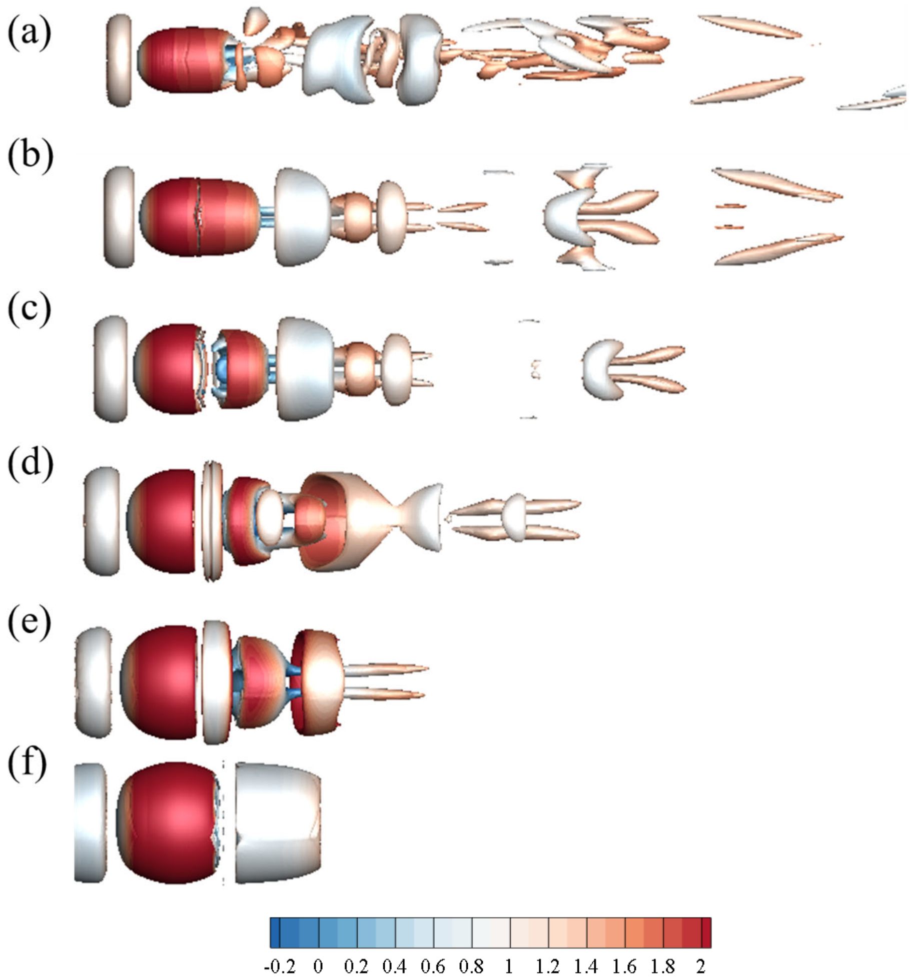
(a)
(b)
(c)
(d)
(e)
(f)
-0.2
0
0.2
0.4
0.6
0.8
1
1.2
1.4
1.6
1.8
2

Figure 8 Instantaneous iso-surfaces of $Q^* = 1$ colored by the time-averaged streamwise velocity at $Re_g = 500$ for (a) $BR = 0.4$; (b) $BR = 0.5$; (c) $BR = 0.6$; (d) $BR = 0.7$; (e) $BR = 0.8$; (f) $BR = 0.9$

Physics of Fluids ACCEPTED MANUSCRIPT

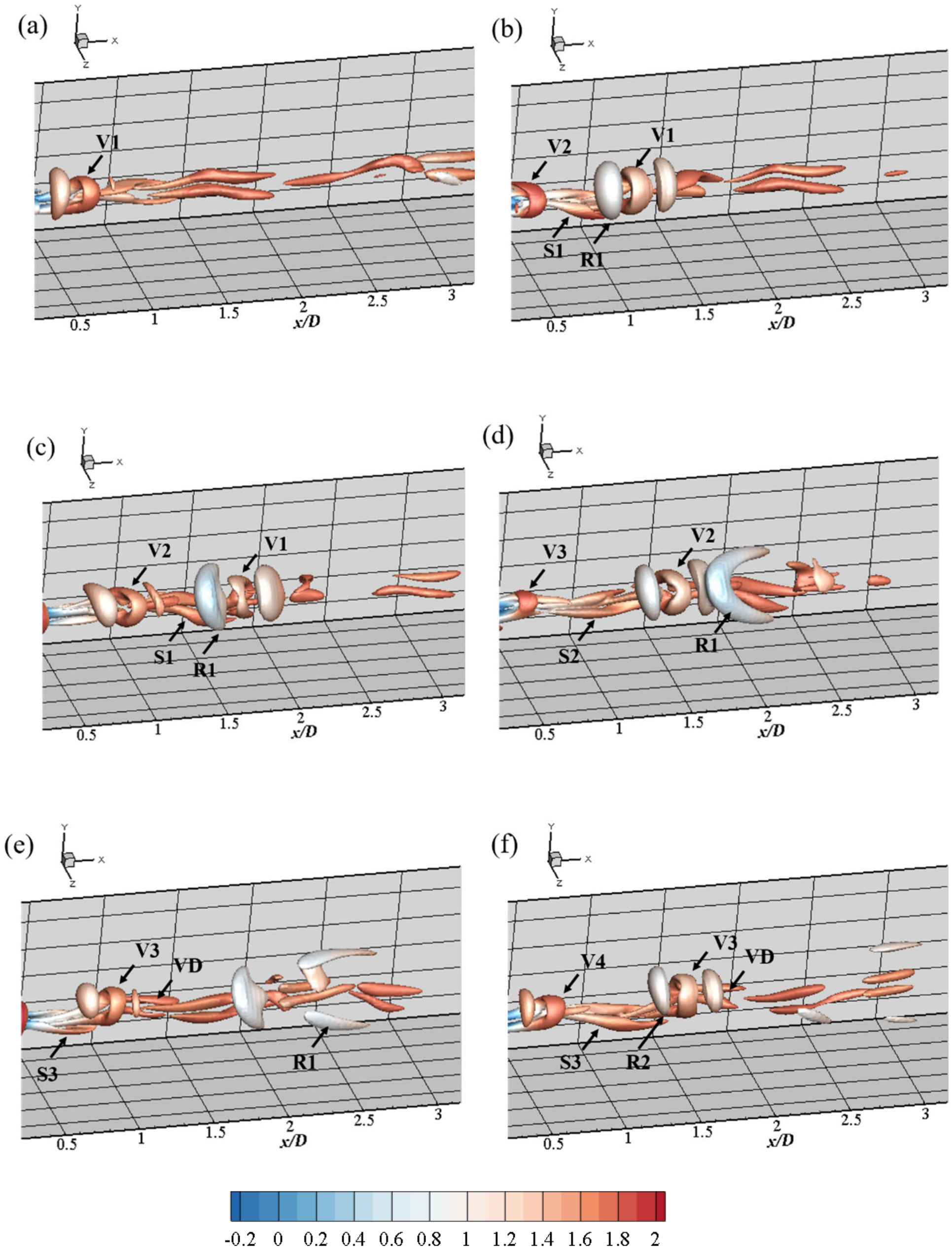
(a)
V1
0.5
1
1.5
2
2.5
3
x/D
(b)
V2
V1
S1
R1
(c)
V2
V1
S1
R1
(d)
V3
V2
S2
R1
(e)
V3
VD
S3
R1
(f)
V4
V3
VD
S3
R2
Y
X
Z
-0.2
0
0.2
0.4
0.6
0.8
1
1.2
1.4
1.6
1.8
2

Figure 9 Instantaneous iso-surfaces of $Q = 2$ for $BR = 0.2$ colored by the time-averaged streamwise velocity at $Re_p = 1250$ at (a) $tU_s/d = 150$; (b) $tU_s/d = 154$; (c) $tU_s/d = 158$; (d) $tU_s/d = 162$; (e) $tU_s/d = 166$; (f) $tU_s/d = 170$

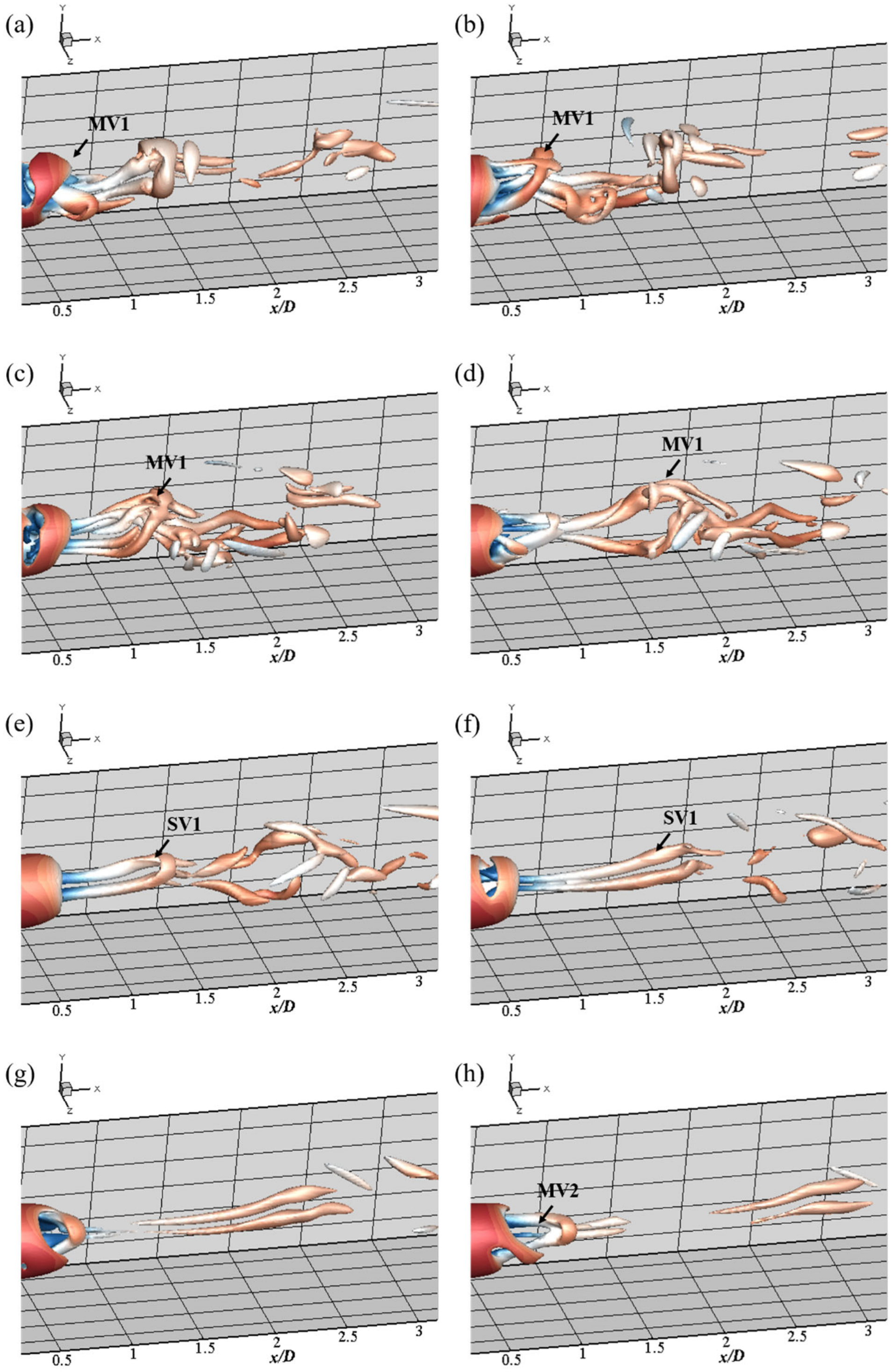
(a)
MV1
(b)
MV1
(c)
MV1
(d)
MV1
(e)
SV1
(f)
SV1
(g)
(h)
MV2
Y
X
Z
0.5
1
1.5
2
2.5
3
x/D

Physics of Fluids ACCEPTED MANUSCRIPT

This is the author's peer reviewed, accepted manuscript. However, the online version of record will be different from this version once it has been copyedited and typeset.
PLEASE CITE THIS ARTICLE AS DOI:10.1063/5.0017349

AIP Publishing

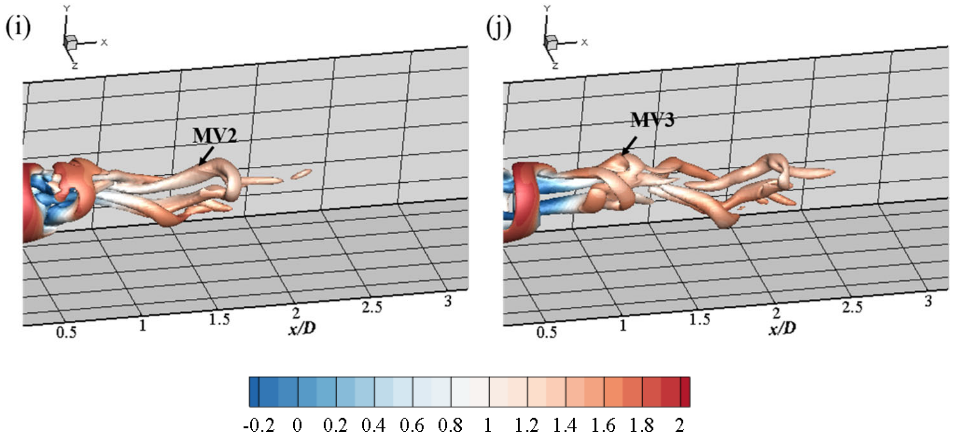

Figure 10 Instantaneous iso-surfaces of $Q = 10$ for $BR = 0.4$ colored by the time-averaged streamwise velocity at $Re_p = 1250$ at (a) $tU_s/d = 649.52$; (b) $tU_s/d = 651.36$; (c) $tU_s/d = 653.2$; (d) $tU_s/d = 655.04$; (e) $tU_s/d = 656.88$; (f) $tU_s/d = 659.64$; (g) $tU_s/d = 661.48$; (h) $tU_s/d = 663.32$; (i) $tU_s/d = 665.16$; (j) $tU_s/d = 667$

Physics of Fluids

PLEASE CITE THIS ARTICLE AS DOI:10.1063/5.0017349

AIP Publishing

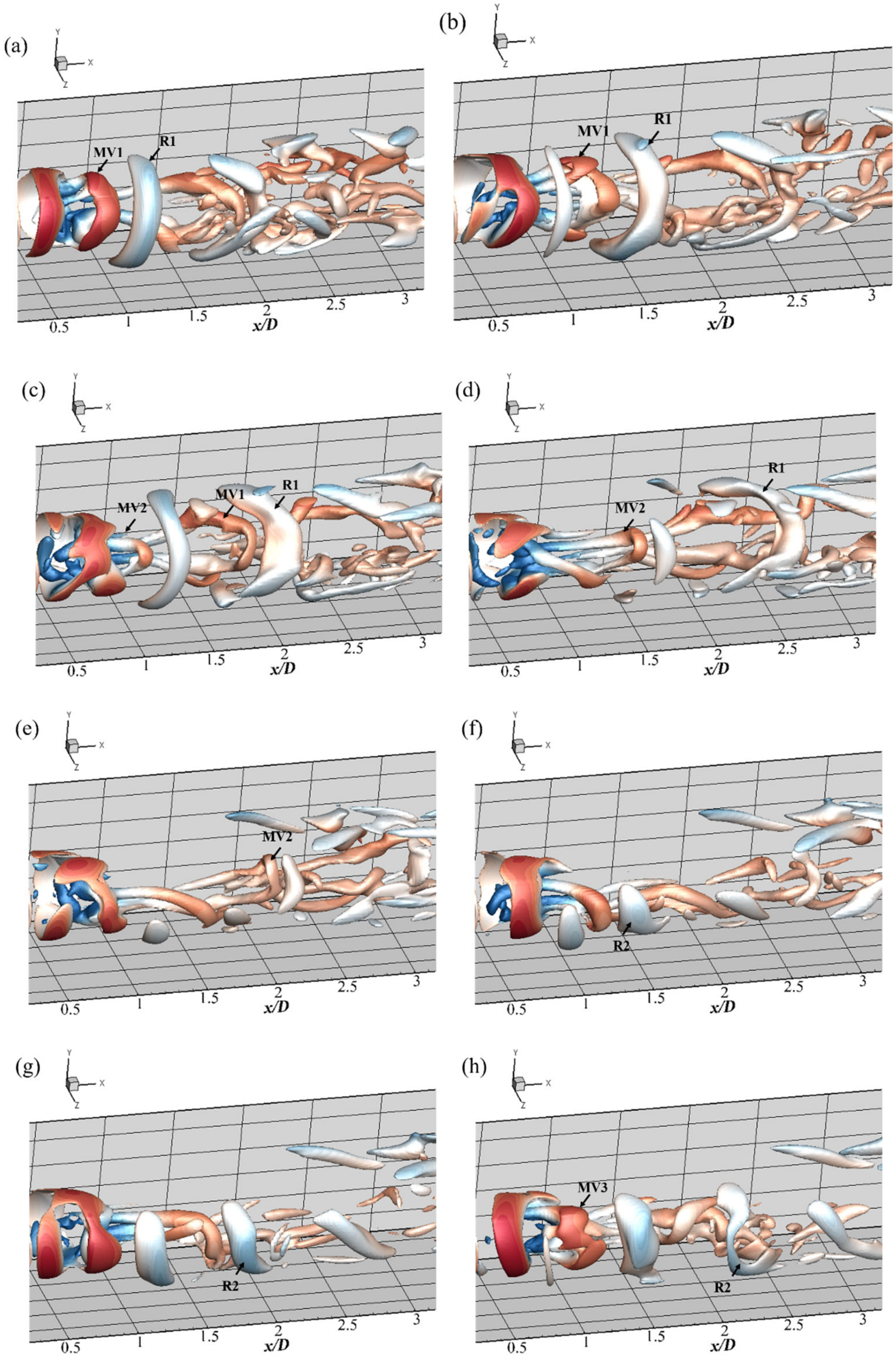
(a)
MV1
R1
(b)
MV1
R1
(c)
MV2
MV1
R1
(d)
R1
MV2
(e)
MV2
(f)
R2
(g)
R2
(h)
MV3
R2
Y
X
Z
0.5
1
1.5
2
2.5
3
x/D

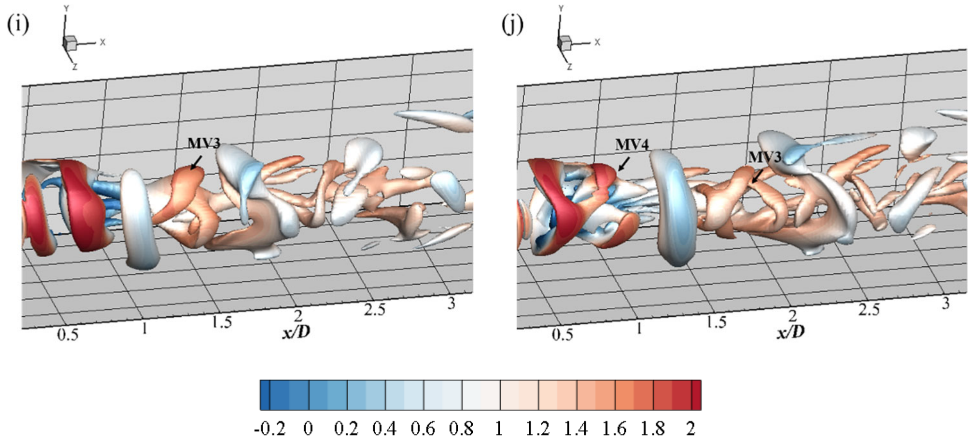
(i)
(j)
MV3
MV4
MV3
0.5
1
1.5
2
2.5
3
x/D
-0.2
0
0.2
0.4
0.6
0.8
1
1.2
1.4
1.6
1.8
2

Figure 11 Instantaneous iso-surfaces of $Q = 10$ for $BR = 0.6$ colored by the time-averaged streamwise velocity at $Re_p = 1250$ at (a) $tU_s/d = 508.4$; (b) $tU_s/d = 509.5$; (c) $tU_s/d = 510.6$; (d) $tU_s/d = 511.7$; (e) $tU_s/d = 512.8$; (f) $tU_s/d = 513.9$; (g) $tU_s/d = 515$; (h) $tU_s/d = 516.1$; (i) $tU_s/d = 517.2$; (j) $tU_s/d = 518.3$

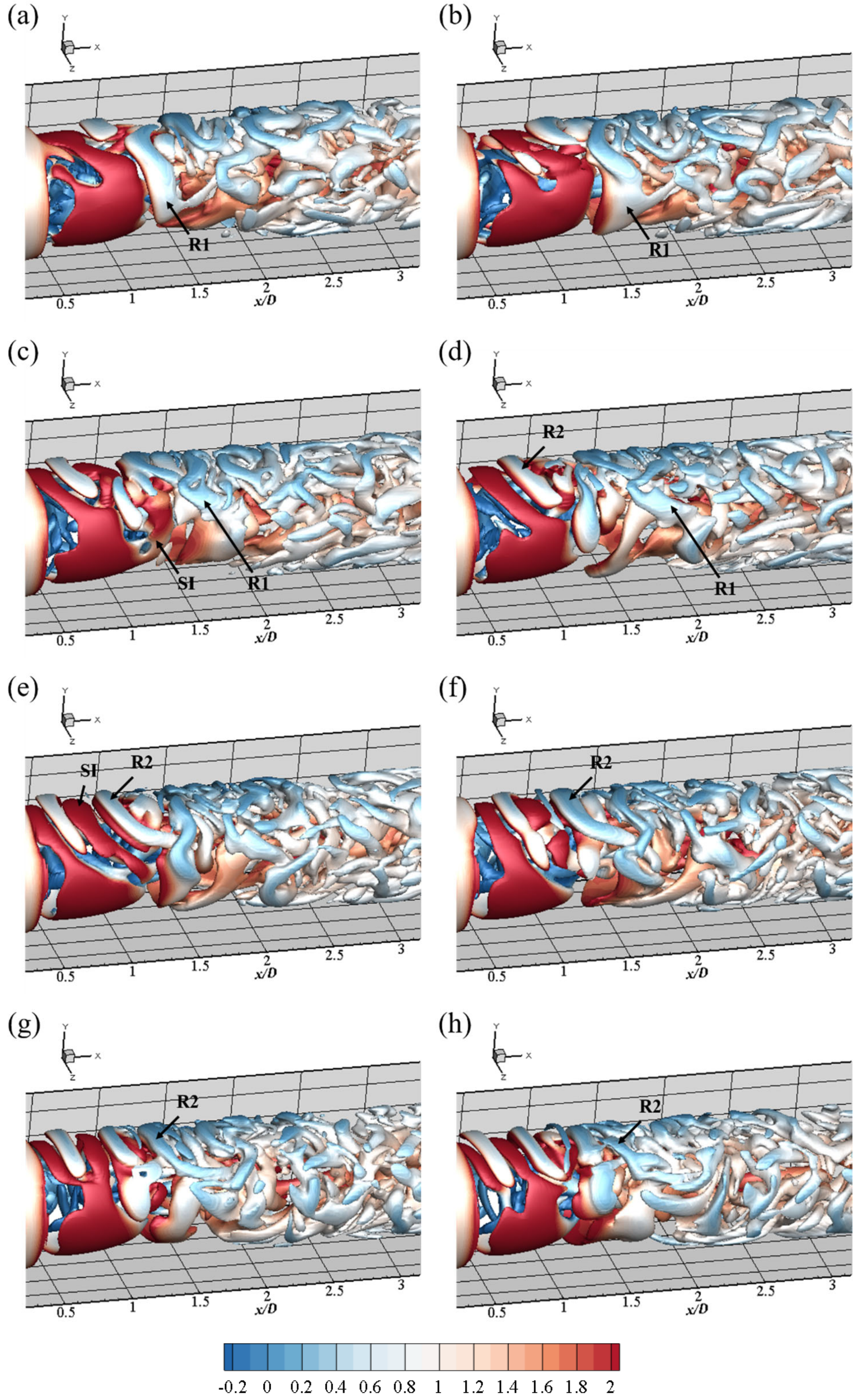
(a)
R1
(b)
R1
(c)
SI
R1
(d)
R2
R1
(e)
SI
R2
(f)
R2
(g)
R2
(h)
R2
Y
X
Z
0.5
1
1.5
2
2.5
3
x/D
-0.2
0
0.2
0.4
0.6
0.8
1
1.2
1.4
1.6
1.8
2

Figure 12 Instantaneous iso-surfaces of $Q = 10$ for $BR = 0.8$ colored by the time-averaged streamwise velocity at $Re_p = 1250$ at (a) $tU_s/d = 258.4$; (b) $tU_s/d = 258.74$; (c) $tU_s/d = 259.08$; (d) $tU_s/d = 259.42$; (e) $tU_s/d = 259.76$; (f) $tU_s/d = 260.1$; (g) $tU_s/d = 260.44$; (h) $tU_s/d = 260.78$

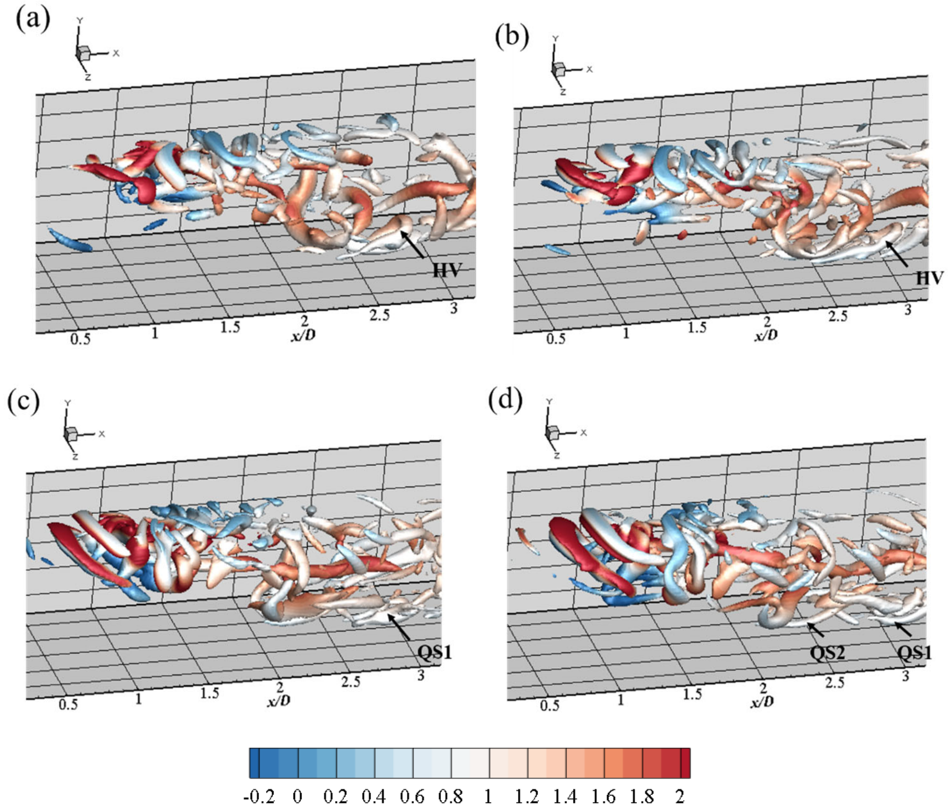
(a)
(b)
(c)
(d)
Y
X
Z
HV
HV
QS1
QS2
QS1
0.5
1
1.5
2
2.5
3
x/D
-0.2
0
0.2
0.4
0.6
0.8
1
1.2
1.4
1.6
1.8
2

Figure 13 Instantaneous iso-surfaces of $Q = 100$ for $BR = 0.8$ colored by the time-averaged streamwise velocity at $Re_p = 1250$ at (a) $tU_s/d = 258.4$; (b) $tU_s/d = 258.74$; (c) $tU_s/d = 259.08$; (d) $tU_s/d = 259.42$ in Figure 12

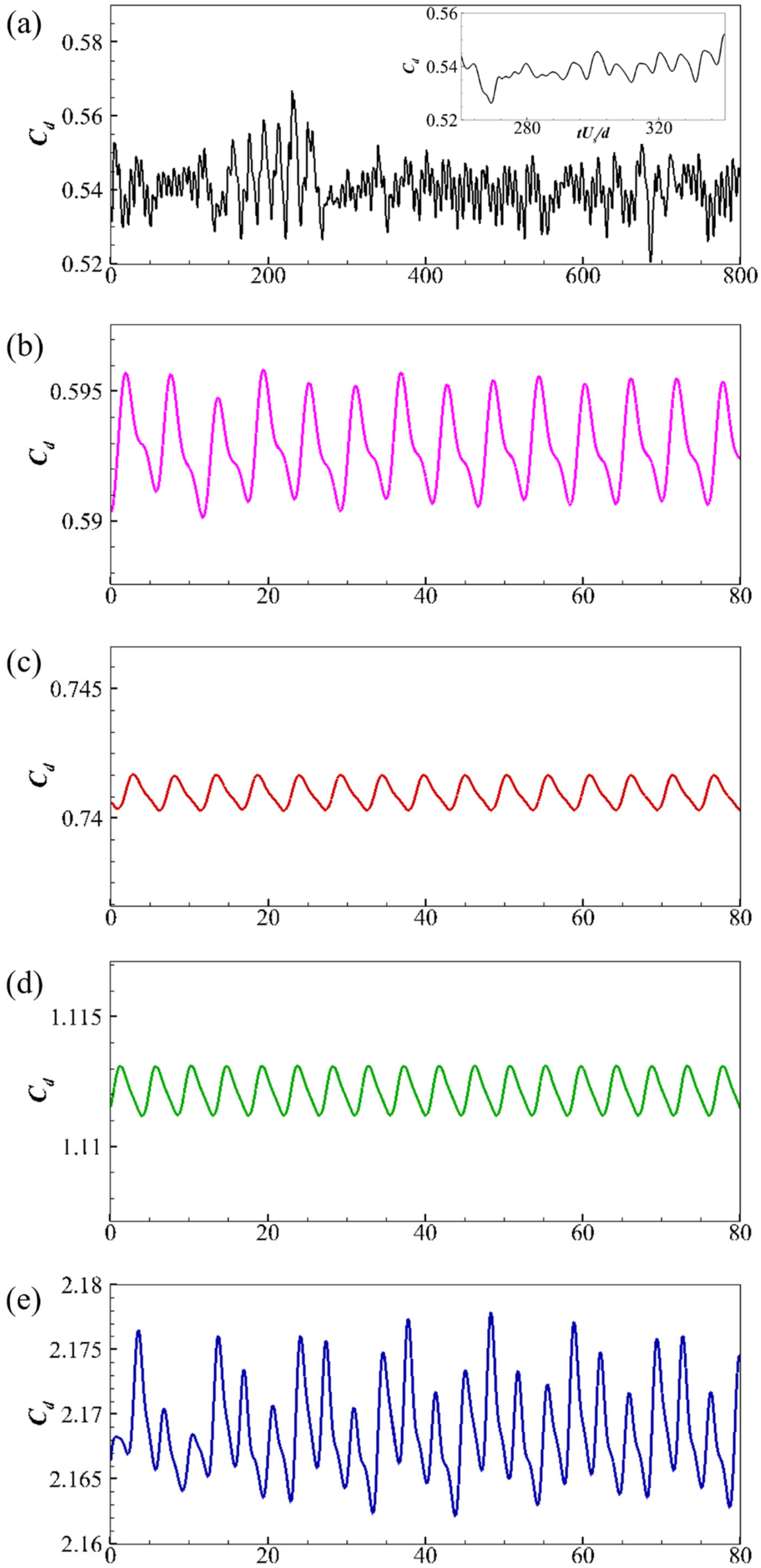
(a)
C_d
0.58
0.56
0.54
0.52
0
200
400
600
800
0.56
C_d
0.54
0.52
280
tU_s/d
320
(b)
C_d
0.595
0.59
0
20
40
60
80
(c)
C_d
0.745
0.74
0
20
40
60
80
(d)
C_d
1.115
1.11
0
20
40
60
80
(e)
C_d
2.18
2.175
2.17
2.165
2.16
0
20
40
60
80

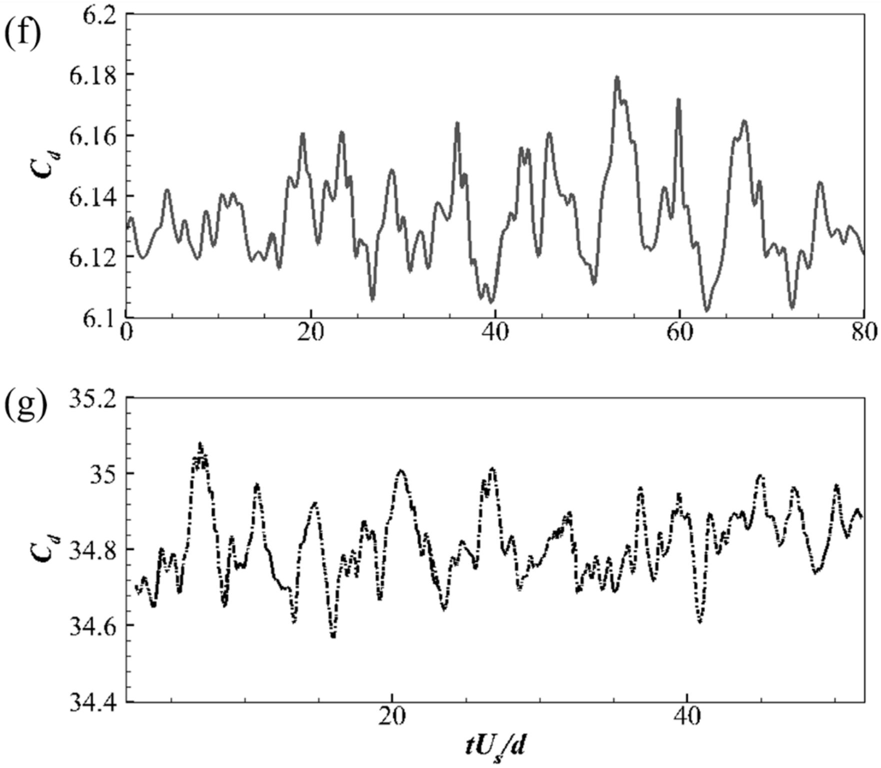

Figure 14 The time histories of C_d for (a) $BR = 0.2$; (b) $BR = 0.4$; (c) $BR = 0.5$; (d) $BR = 0.6$; (e) $BR = 0.7$; (f) $BR = 0.8$; (g) $BR = 0.9$

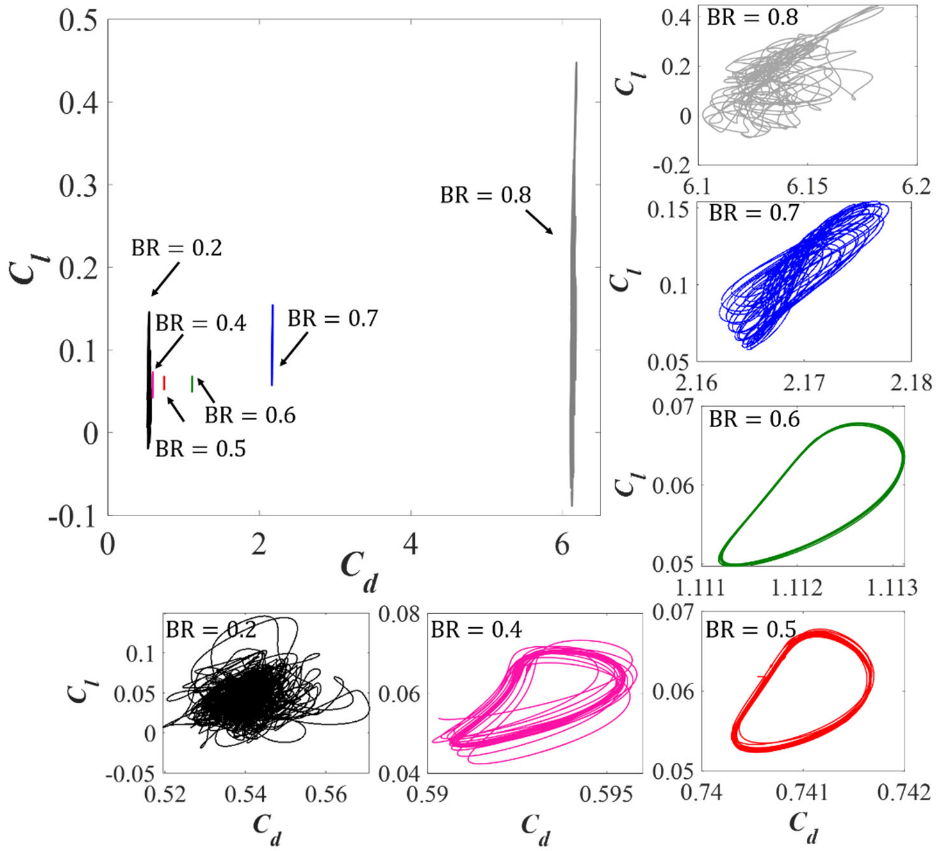

Figure 15 Phase diagram (C_d, C_l) for the sphere at $Re_s = 500$

PLEASE CITE THIS ARTICLE AS DOI: 10.1063/5.0017349

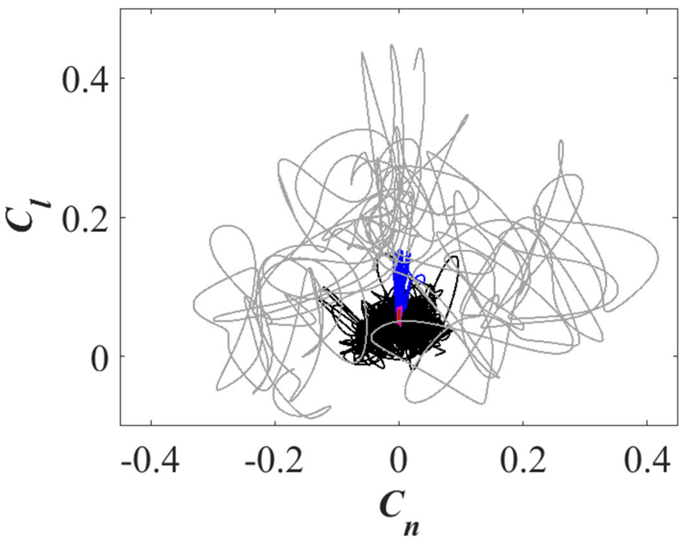

Figure 16 Phase diagram (C_n, C_l) for the sphere at $Re_s = 500$

Physics of Fluids ACCEPTED MANUSCRIPT

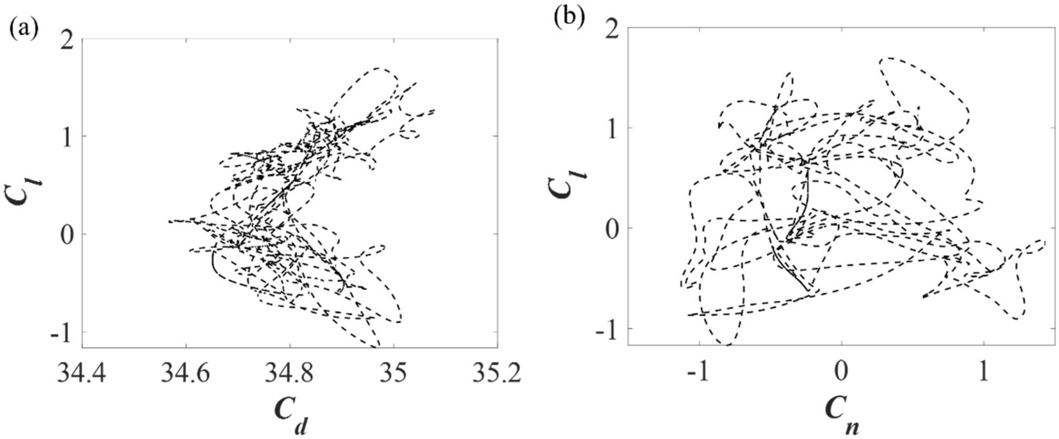

Figure 17 Phase diagram (a) (C_d, C_l) and (b) (C_n, C_l) for the sphere at $Re_s = 500$ for $BR = 0.9$

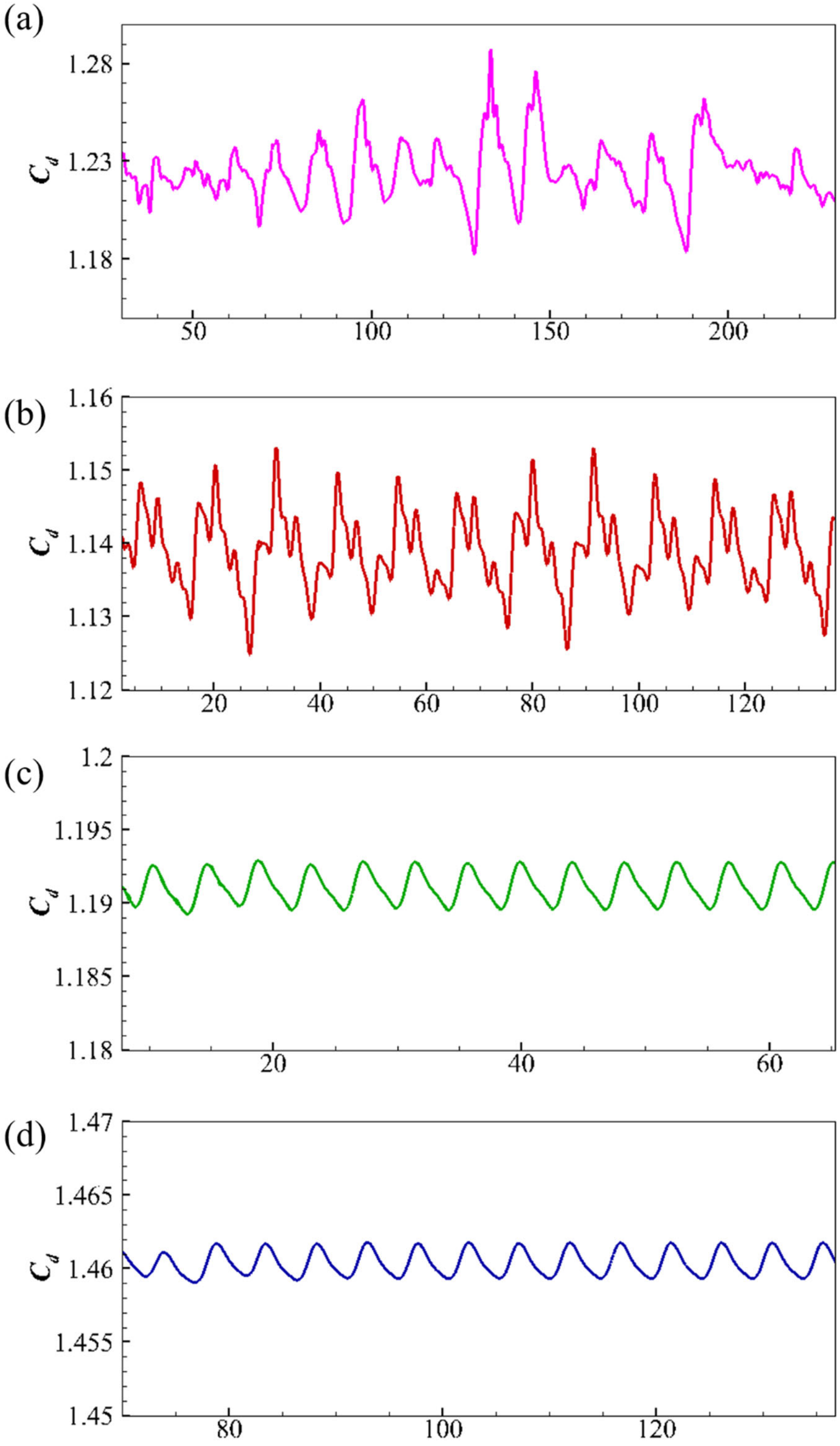
(a)
C_d
1.28
1.23
1.18
50
100
150
200
(b)
C_d
1.16
1.15
1.14
1.13
1.12
20
40
60
80
100
120
(c)
C_d
1.2
1.195
1.19
1.185
1.18
20
40
60
(d)
C_d
1.47
1.465
1.46
1.455
1.45
80
100
120

Physics of Fluids ACCEPTED MANUSCRIPT

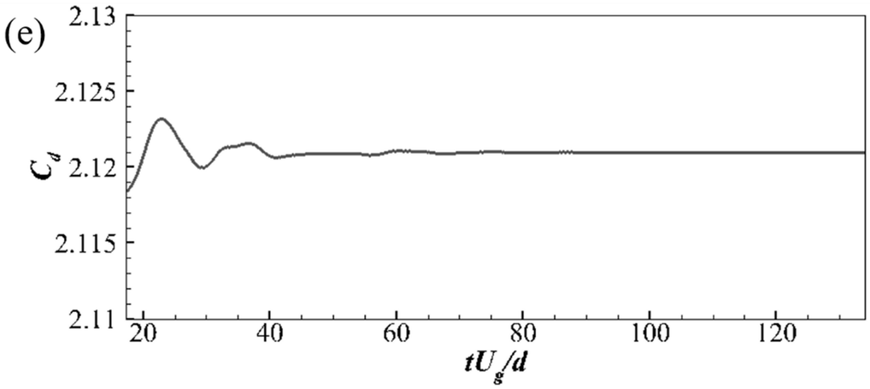

Figure 18 The time histories of C_d for (a) $BR = 0.4$; (b) $BR = 0.6$; (c) $BR = 0.6$; (d) $BR = 0.7$; (e) $BR = 0.8$

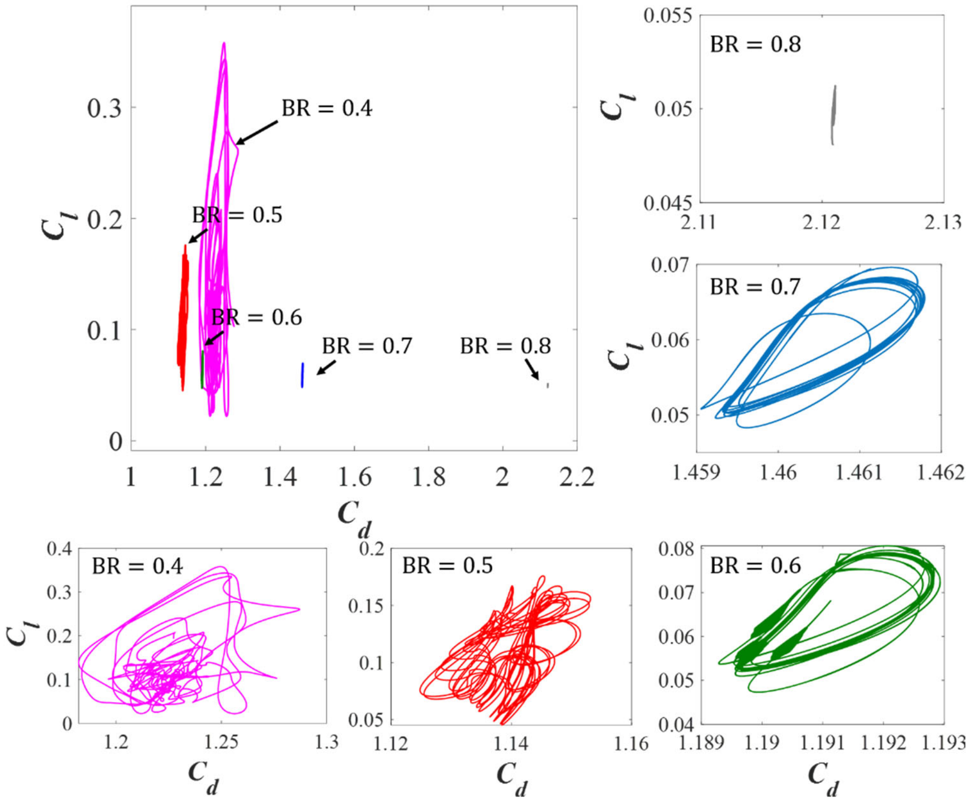

Figure 19 Phase diagram (C_d, C_l) for the sphere at $Re_g = 500$

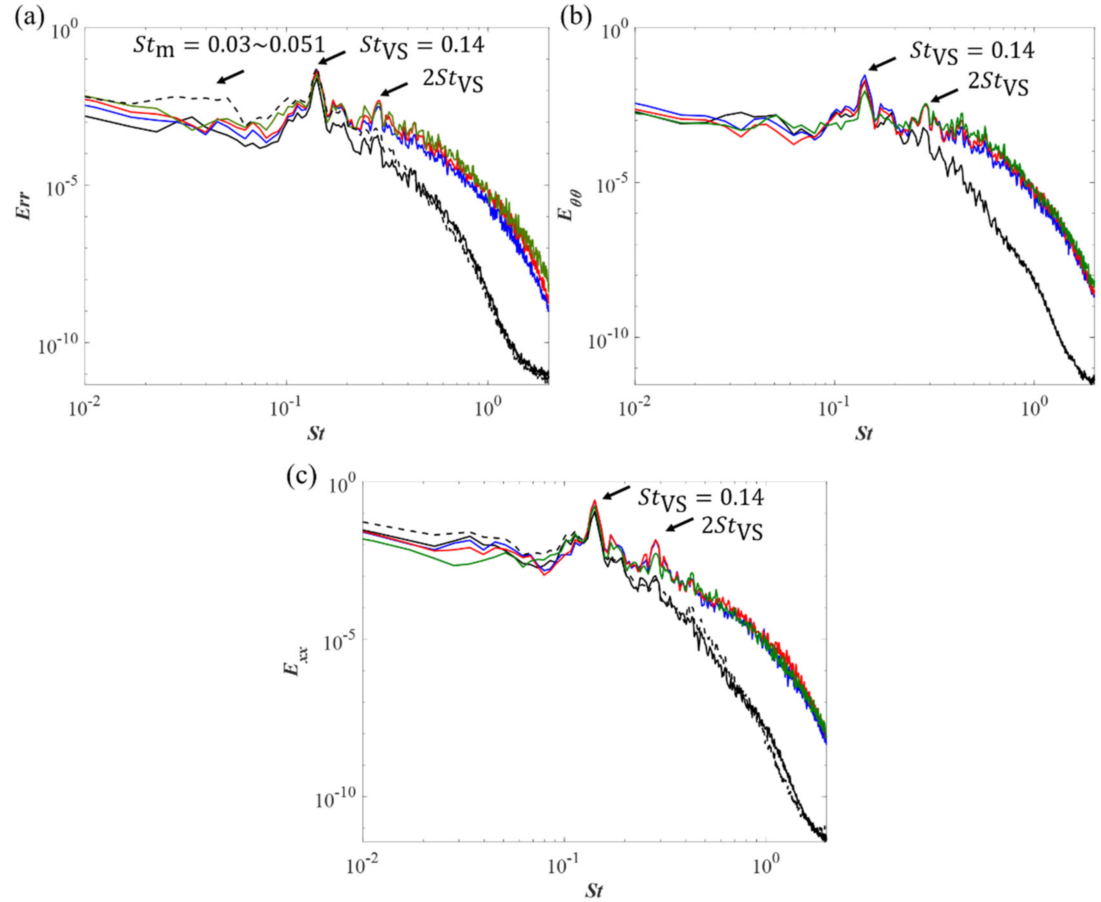

Figure 20 The spectra of the (a) radial velocity; (b) azimuthal velocity and (c) streamwise velocity for $BR = 0.2$ at $Re_s = 490$. (black solid: $(x/d, r/d) = (1,0.6)$; blue: $(x/d, r/d) = (2.4,0.6)$; red: $(x/d, r/d) = (3,0.6)$; green: $(x/d, r/d) = (5,0.6)$; black dashed: $(x/d, r/d) = (1,0.5)$)

Physics of Fluids ACCEPTED MANUSCRIPT

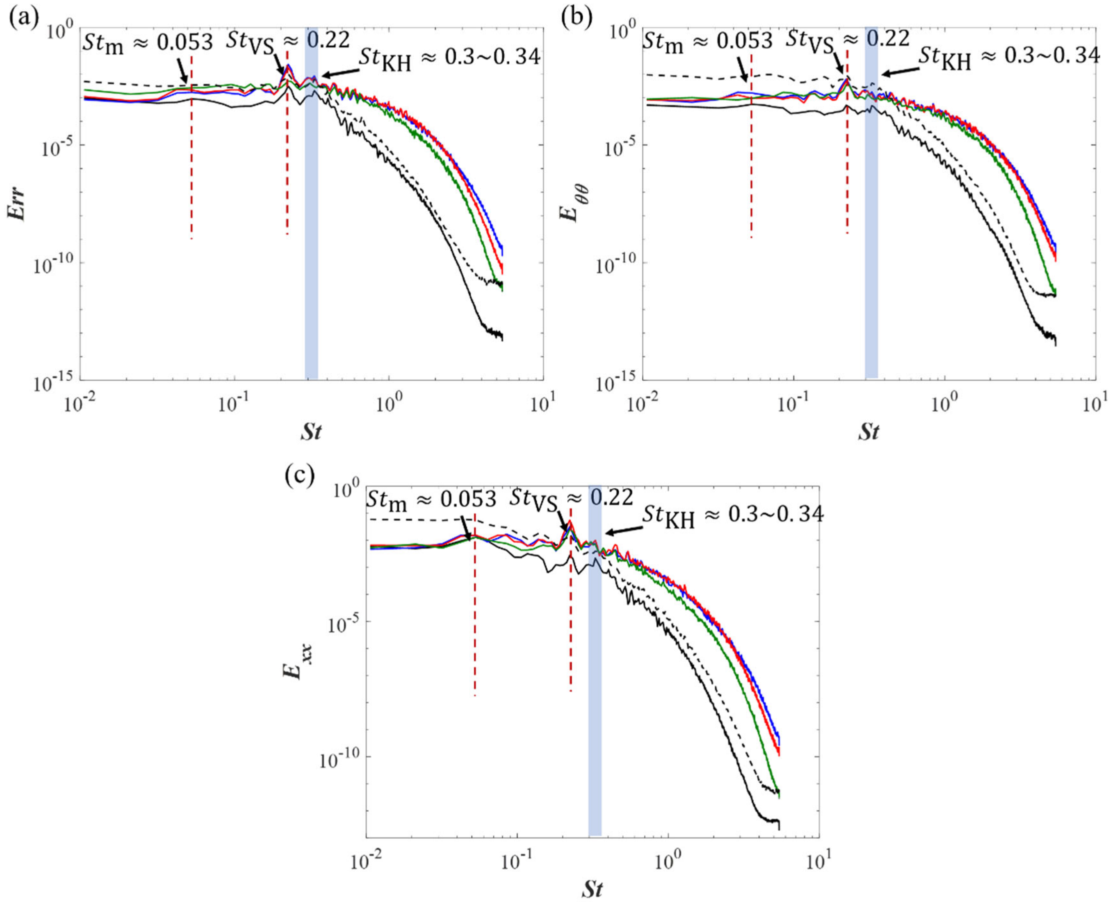

Figure 21 The spectra of the (a) radial velocity; (b) azimuthal velocity and (c) streamwise velocity for $BR = 0.4$ at $Re_s = 920$. (black solid: $(x/d, r/d) = (1,0.6)$; blue: $(x/d, r/d) = (2.4,0.6)$; red: $(x/d, r/d) = (3,0.6)$; green: $(x/d, r/d) = (5,0.6)$; black dashed: $(x/d, r/d) = (1,0.5)$)

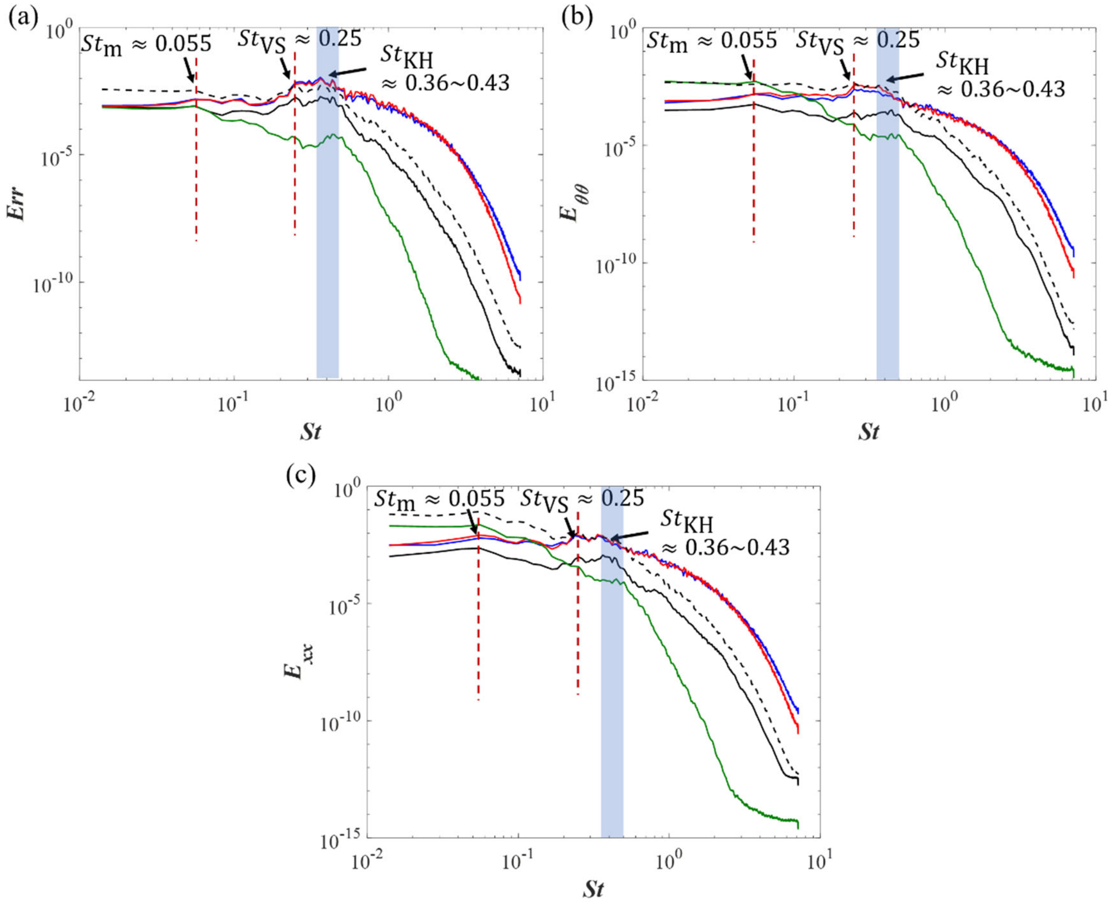

Figure 22 The spectra of the (a) radial velocity; (b) azimuthal velocity and (c) streamwise velocity for $BR = 0.5$ at $Re_s = 1093.8$. (black solid: $(x/d, r/d) = (1,0.6)$; blue: $(x/d, r/d) = (2.4,0.6)$; red: $(x/d, r/d) = (3,0.6)$; green: $(x/d, r/d) = (5,0.6)$; black dashed: $(x/d, r/d) = (1,0.5)$)

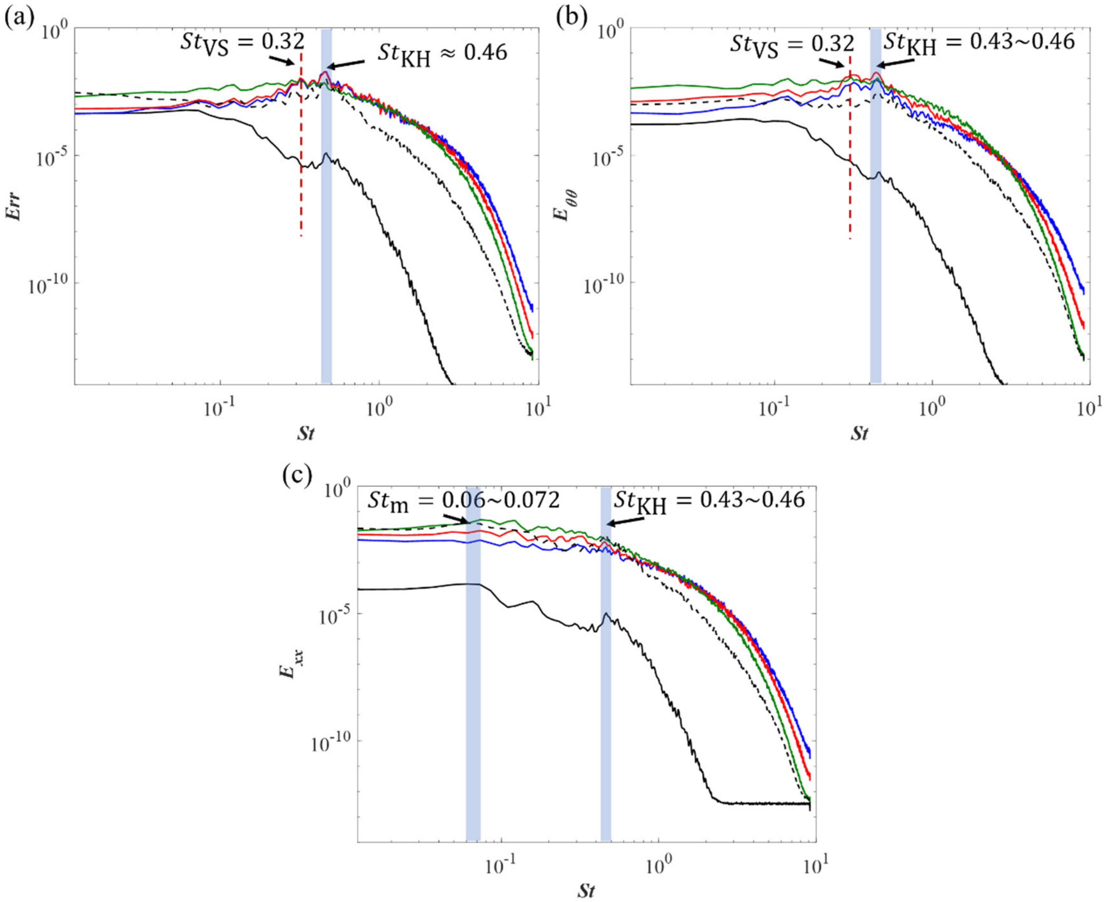

Figure 23 The spectra of the (a) radial velocity; (b) azimuthal velocity and (c) streamwise velocity for $BR = 0.6$ at $Re_s = 1230$. (black solid: $(x/d, r/d) = (1,0.6)$; blue: $(x/d, r/d) = (2.4,0.6)$; red: $(x/d, r/d) = (3,0.6)$; green: $(x/d, r/d) = (5,0.6)$; black dashed: $(x/d, r/d) = (1,0.5)$)

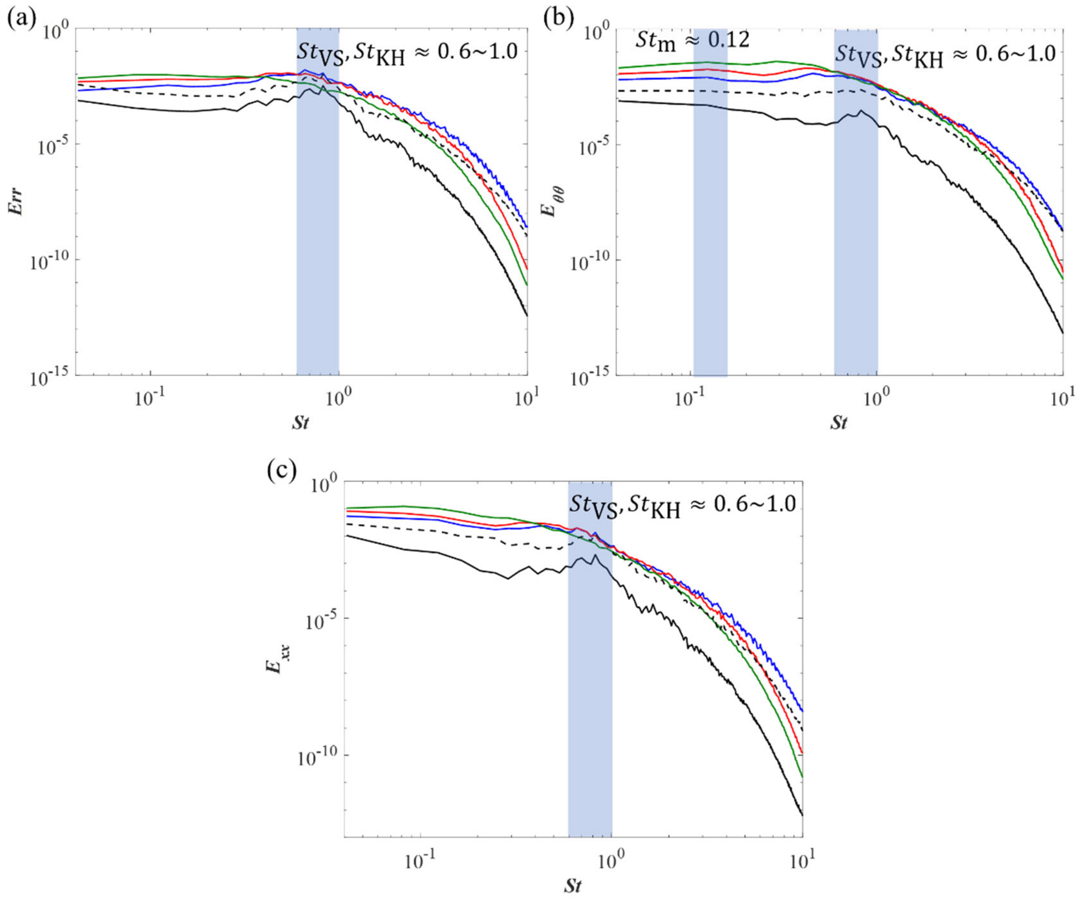

Figure 24 The spectra of the (a) radial velocity; (b) azimuthal velocity and (c) streamwise velocity for $BR = 0.7$ at $Re_s = 1321$. (black solid: $(x/d, r/d) = (1,0.6)$; blue: $(x/d, r/d) = (2.4,0.6)$; red: $(x/d, r/d) = (3,0.6)$; green: $(x/d, r/d) = (5,0.6)$; black dashed: $(x/d, r/d) = (1,0.5)$)

.

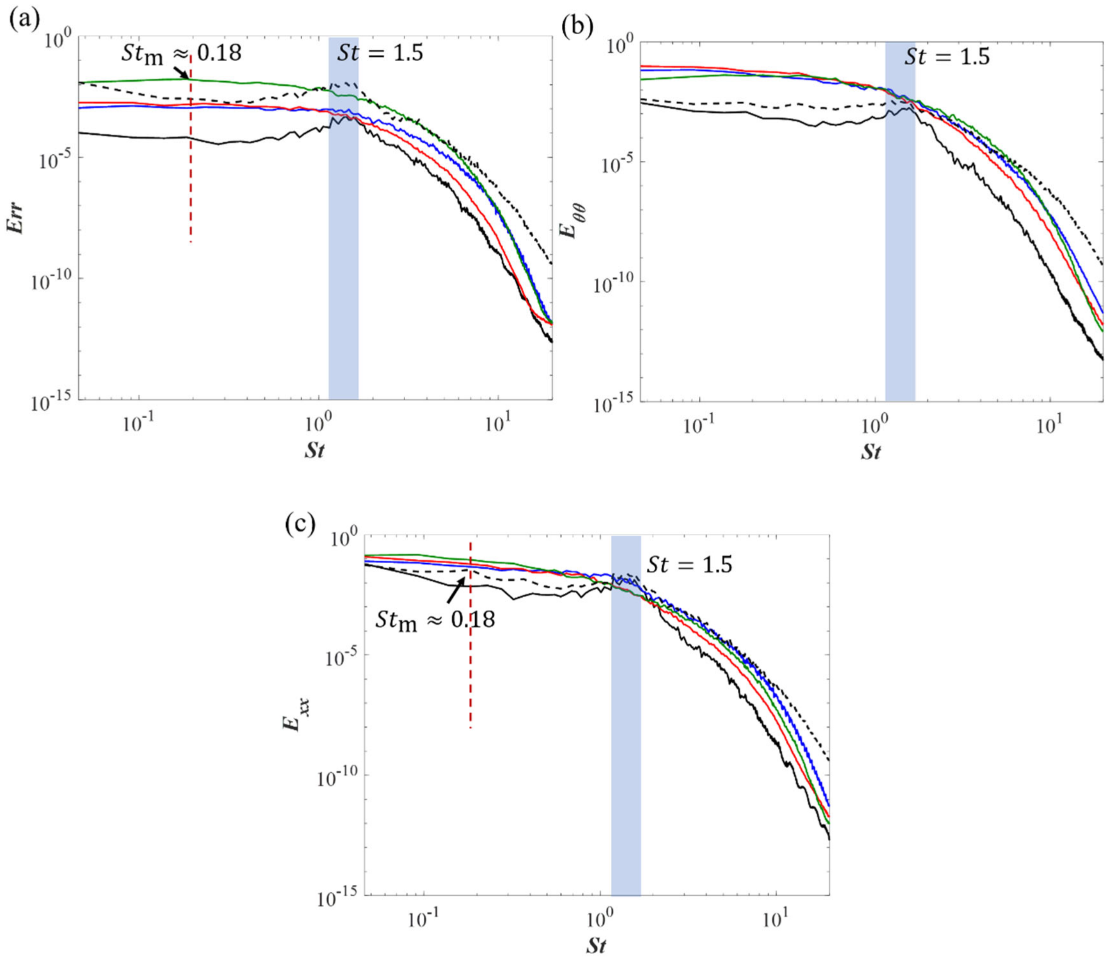

Figure 25 The spectra of the (a) radial velocity; (b) azimuthal velocity and (c) streamwise velocity for $BR = 0.8$ at $Re_s = 1360$. (black solid: $(x/d, r/d) = (1,0.6)$; blue: $(x/d, r/d) = (2.4,0.6)$; red: $(x/d, r/d) = (3,0.6)$; green: $(x/d, r/d) = (5,0.6)$; black dashed: $(x/d, r/d) = (1,0.5)$)

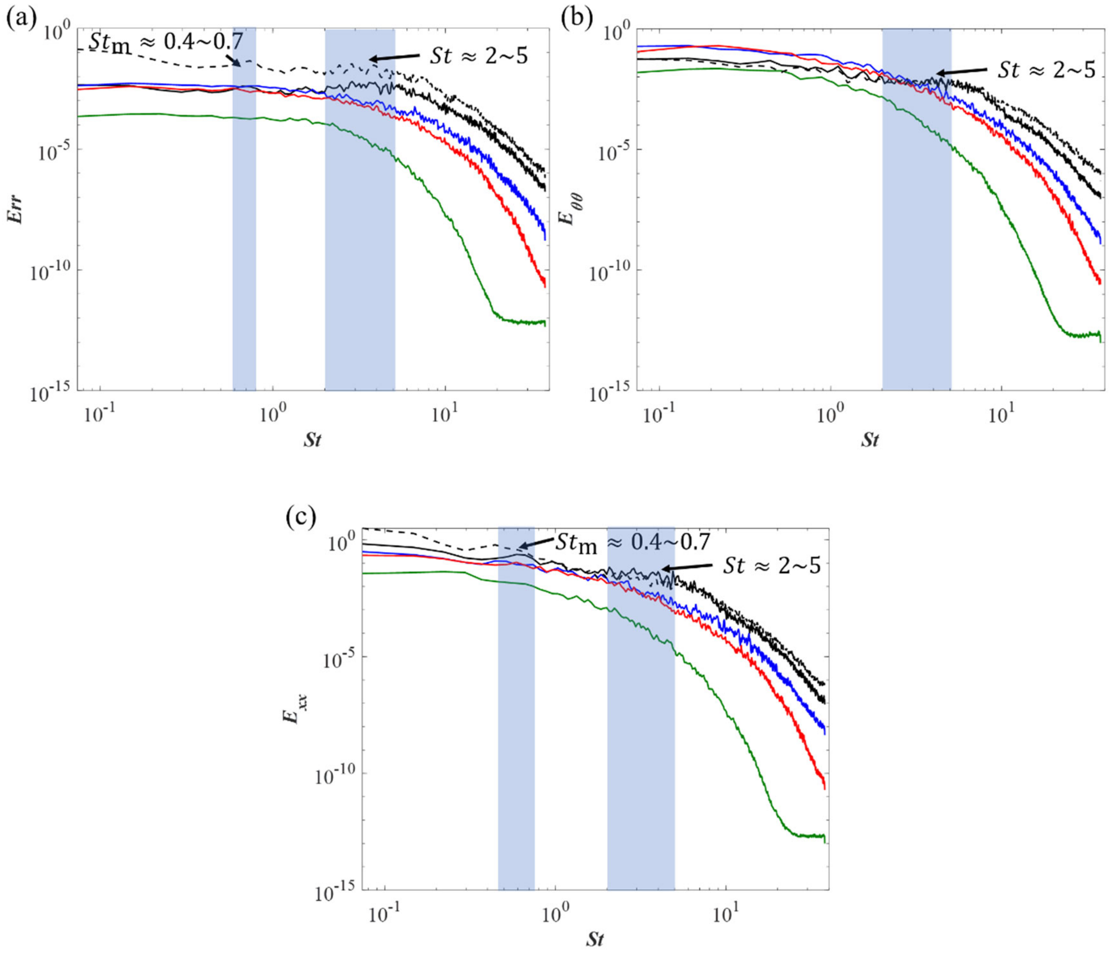

Figure 26 The spectra of the (a) radial velocity; (b) azimuthal velocity and (c) streamwise velocity for $BR = 0.9$ at $Re_s = 1338.75$. (black solid: $(x/d, r/d) = (1,0.6)$; blue: $(x/d, r/d) = (2.4,0.6)$; red: $(x/d, r/d) = (3,0.6)$; green: $(x/d, r/d) = (5,0.6)$; black dashed: $(x/d, r/d) = (1,0.5)$)

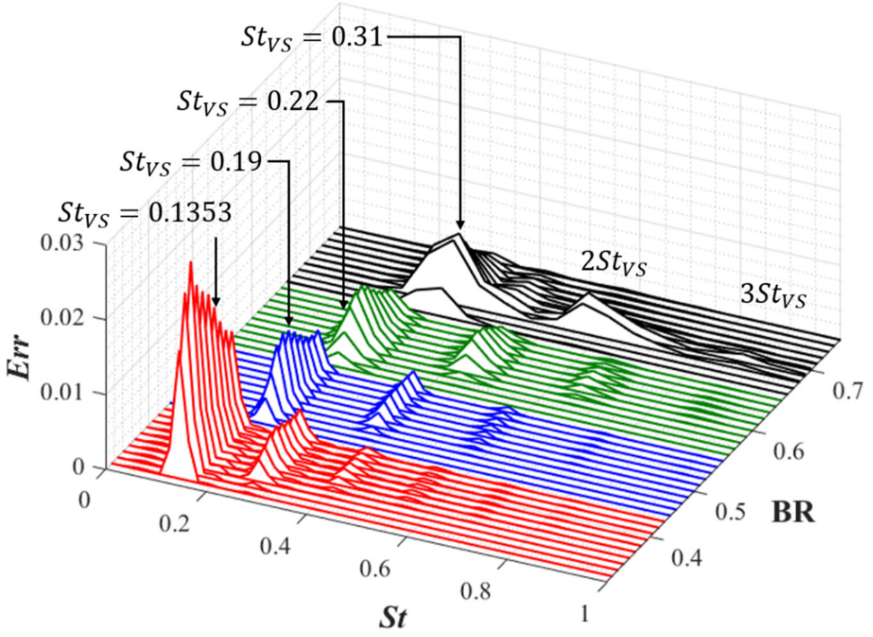

Figure 27 The spectra of the radial velocities at the streamwise locations of $x/d = 0.2{\sim}2$ spaced by $x/d = 0.2$ for $BR = 0.4$ (red); 0.5 (blue); 0.6 (green); 0.7 (black) at $Re_s = 500$

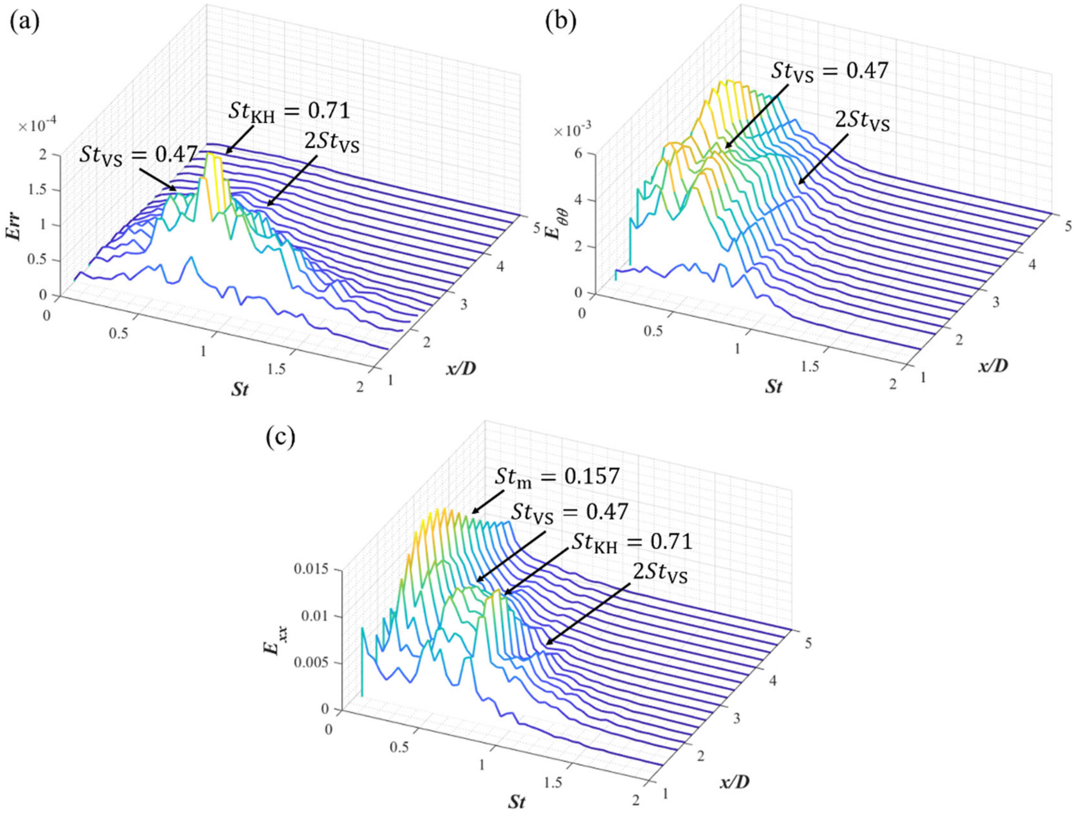

Figure 28 The spectra of the (a) radial velocity; (b) azimuthal velocity and (c) streamwise velocity for $BR = 0.8$ at $Re_s = 500$ at the streamwise locations of $x/d = 0.2 \sim 5$ spaced by $x/d = 0.2$

Physics of Fluids ACCEPTED MANUSCRIPT

This is the author's peer reviewed, accepted manuscript. However, the online version of record will be different from this version once it has been copyedited and typeset.
PLEASE CITE THIS ARTICLE AS DOI:10.1063/5.0017349

AIP Publishing

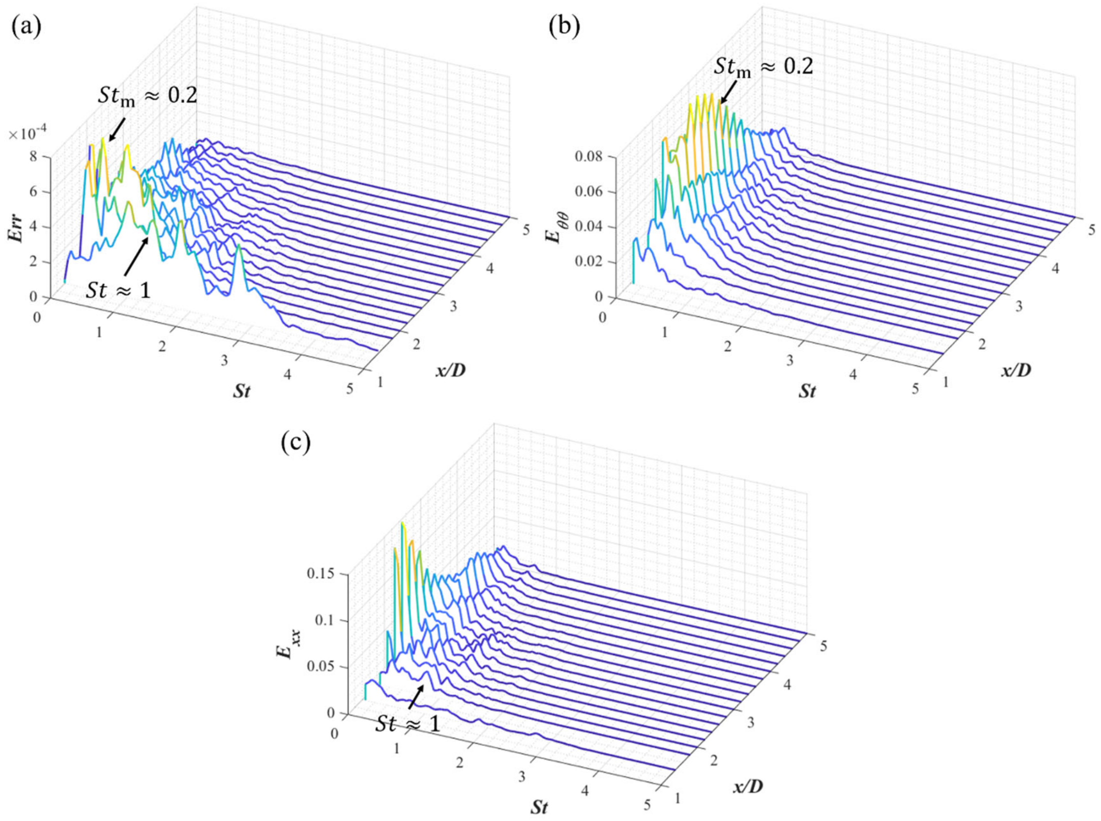

Figure 29 The spectra of the (a) radial velocity; (b) azimuthal velocity and (c) streamwise velocity for $BR = 0.9$ at $Re_s = 500$ at the streamwise locations of $x/d = 0.2 \sim 5$ spaced by $x/d = 0.2$

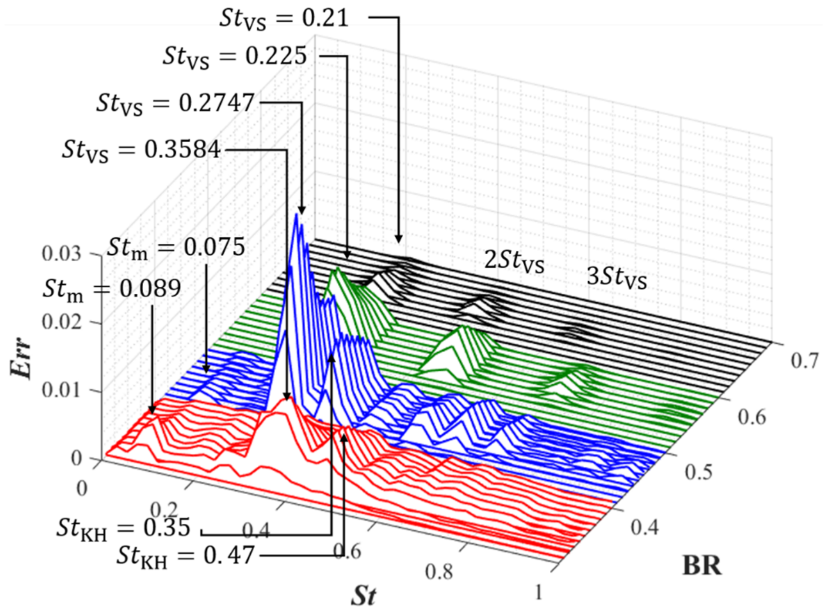

Figure 30 The spectra of the radial velocities at the streamwise locations of $x/d = 0.2{\sim}2$ spaced by $x/d = 0.2$ for $BR = 0.4$ (red); 0.5 (blue); 0.6 (green); 0.7 (black) at $Re_g = 500$

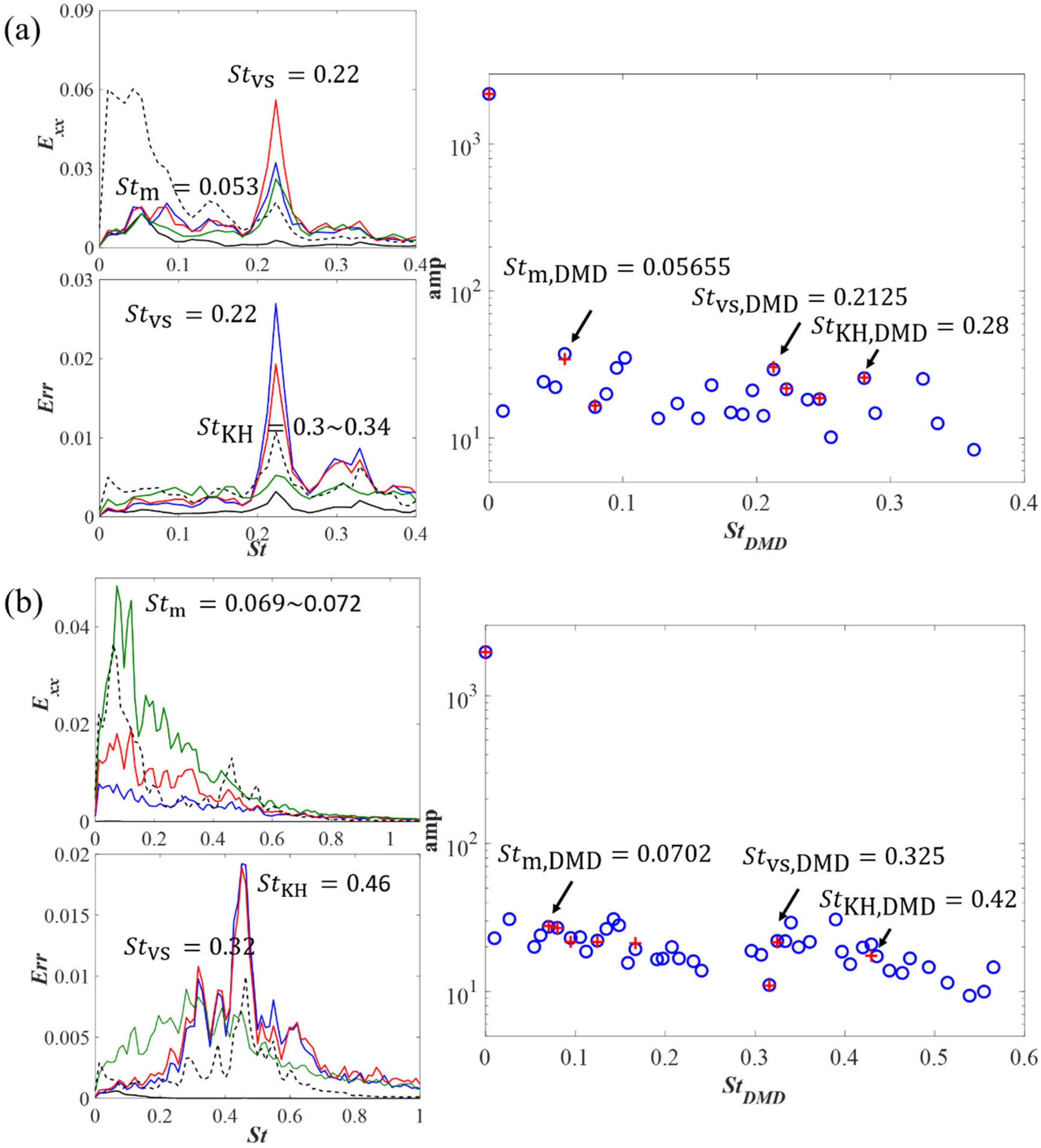
(a)
E_{xx}
St_{vs} = 0.22
St_{m} = 0.053
0.09
0.06
0.03
0
0.1
0.2
0.3
0.4
Err
St_{vs} = 0.22
St_{KH} = 0.3~0.34
0.03
0.02
0.01
St
amp
10^{3}
10^{2}
10^{1}
$St_{\mathrm{m,DMD}}$ = 0.05655
$St_{\mathrm{vs,DMD}}$ = 0.2125
$St_{\mathrm{KH,DMD}}$ = 0.28
St_{DMD}
(b)
E_{xx}
St_{m} = 0.069~0.072
0.04
0.02
0
0.2
0.4
0.6
0.8
1
Err
St_{KH} = 0.46
St_{vs} = 0.32
0.02
0.015
0.01
0.005
St
amp
$St_{\mathrm{m,DMD}}$ = 0.0702
$St_{\mathrm{vs,DMD}}$ = 0.325
$St_{\mathrm{KH,DMD}}$ = 0.42
0.5
St_{DMD}

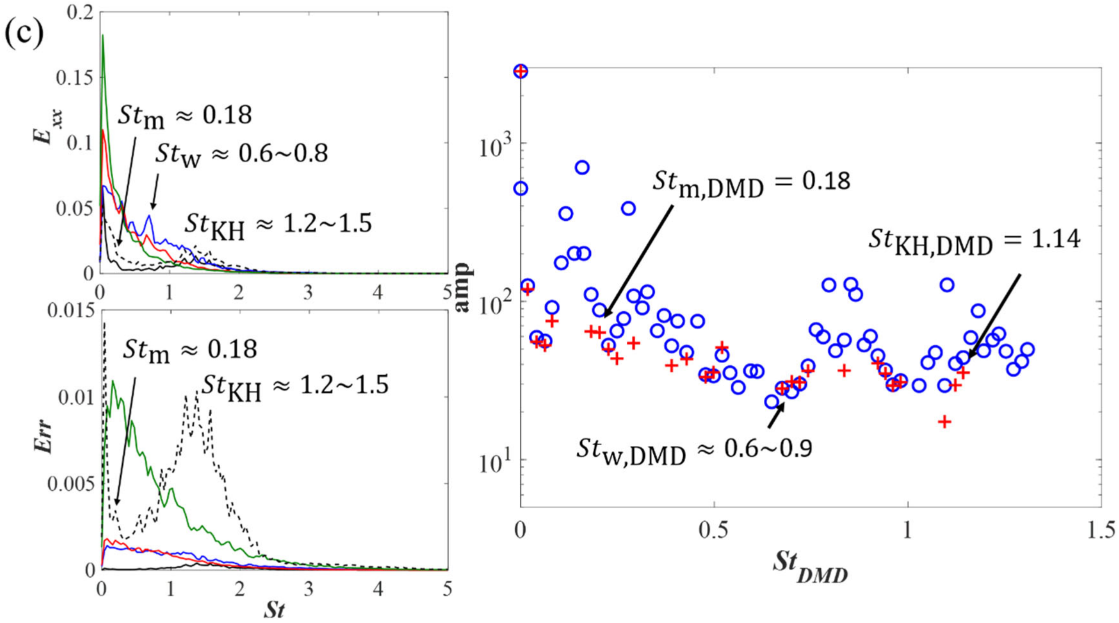

Figure 31 The frequency spectra of the DMD modes for (a) $BR = 0.4$; (b) 0.6 and (c) 0.8 with the dominant modes denoted by the arrows (Blue circles: the modes obtained by using the original DMD method; red crossings: the modes obtained by applying sparsity-promoted algorithm)

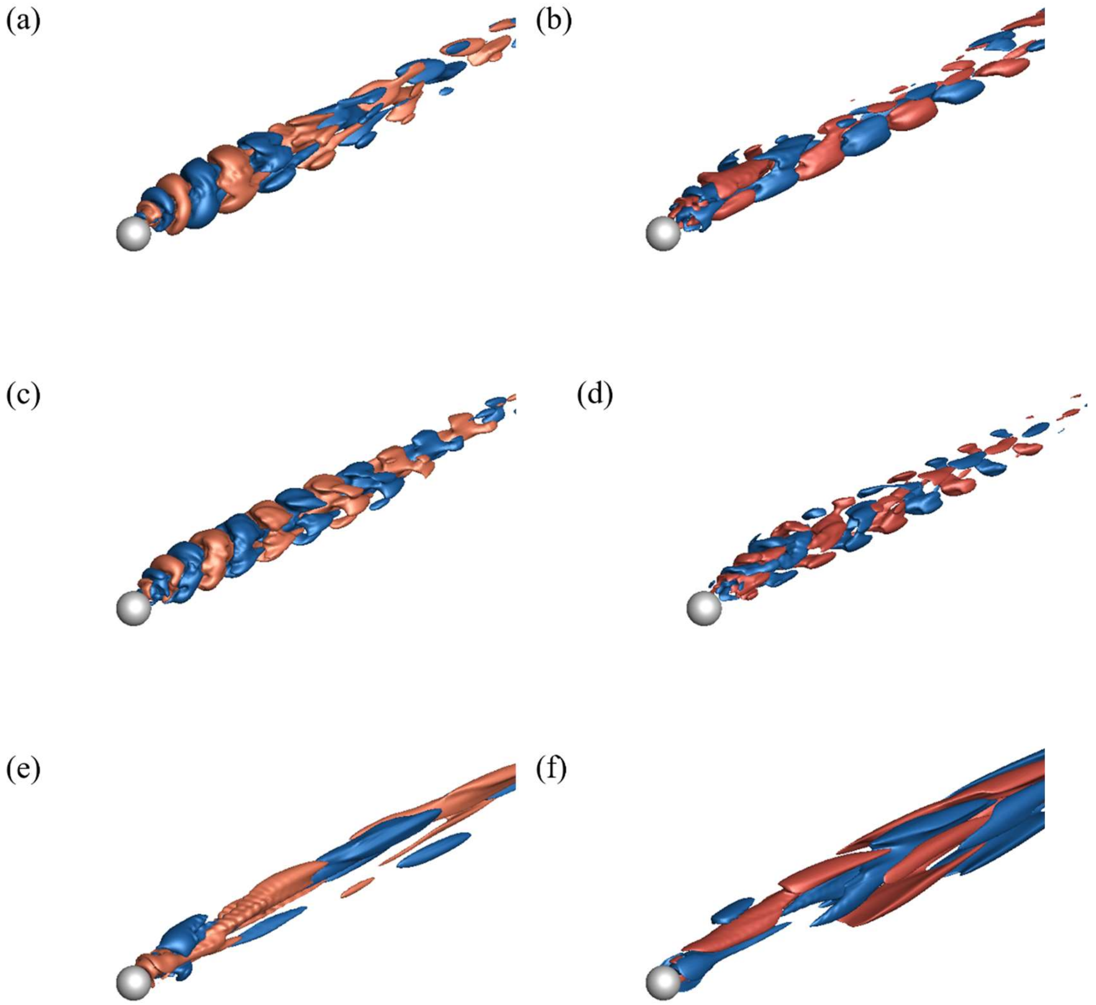

Figure 32 Iso-surfaces of $u_r/U_m = \pm 0.0002$ for the radial velocity (a, c, e) and $u/U_m = \pm 0.0005$ for the streamwise velocity (b, d, f) of the three dominant DMD modes of $BR = 0.4$: (a, b) vortex shedding mode; (c, d) KH instability mode; (e, f) low-frequency mode

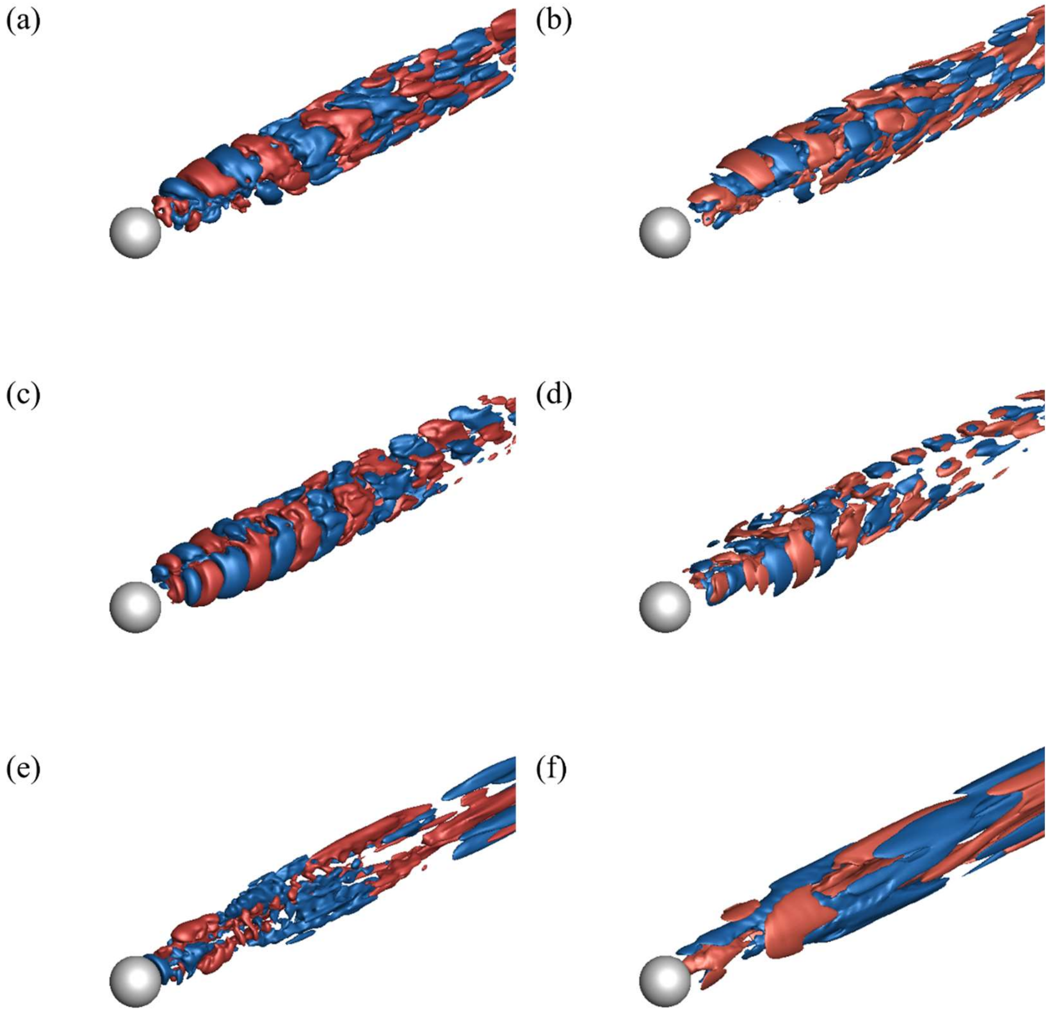

Figure 33 Iso-surfaces of $u_r/U_m = \pm 0.0002$ for the radial velocity (a, c, e) and $u/U_m = \pm 0.0005$ for the streamwise velocity (b, d, f) of the three dominant DMD modes of $BR = 0.6$: (a, b) vortex shedding mode; (c, d) KH instability mode; (e, f) low-frequency mode

Physics of Fluids ACCEPTED MANUSCRIPT

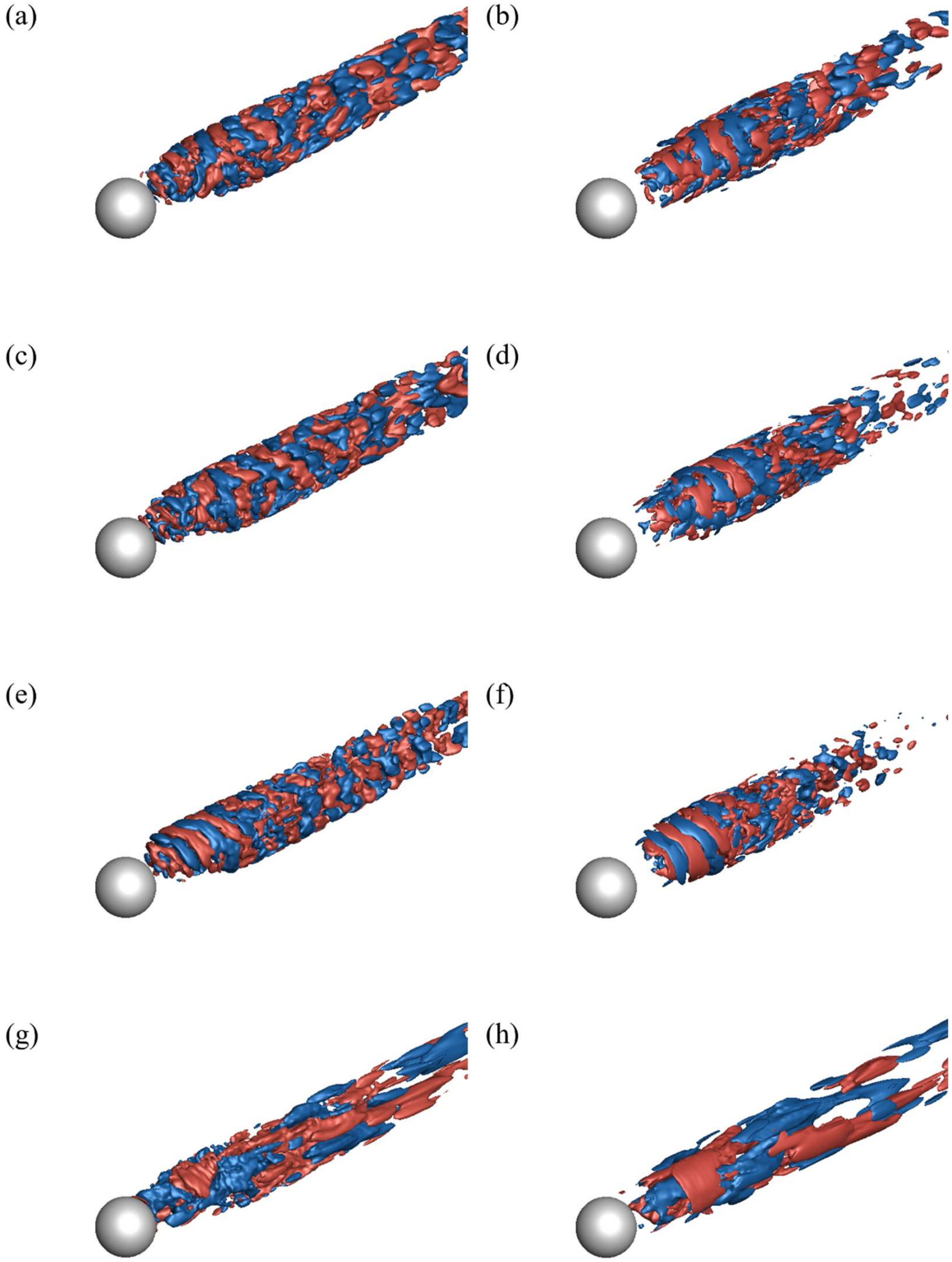

Figure 34 Iso-surfaces of $u_r/U_m = \pm 0.0002$ for the radial velocity (a, c, e, g) and $u/U_m = \pm 0.0005$ for the streamwise velocity (b, d, f, h) of the four dominant DMD modes of $BR = 0.8$: (a, b) DMD modes at $St_{\mathrm{DMD}} = 0.74$; (c, d) DMD modes at $St_{\mathrm{DMD}} = 0.835$; (e, f) KH instability mode; (g, h) low-frequency mode

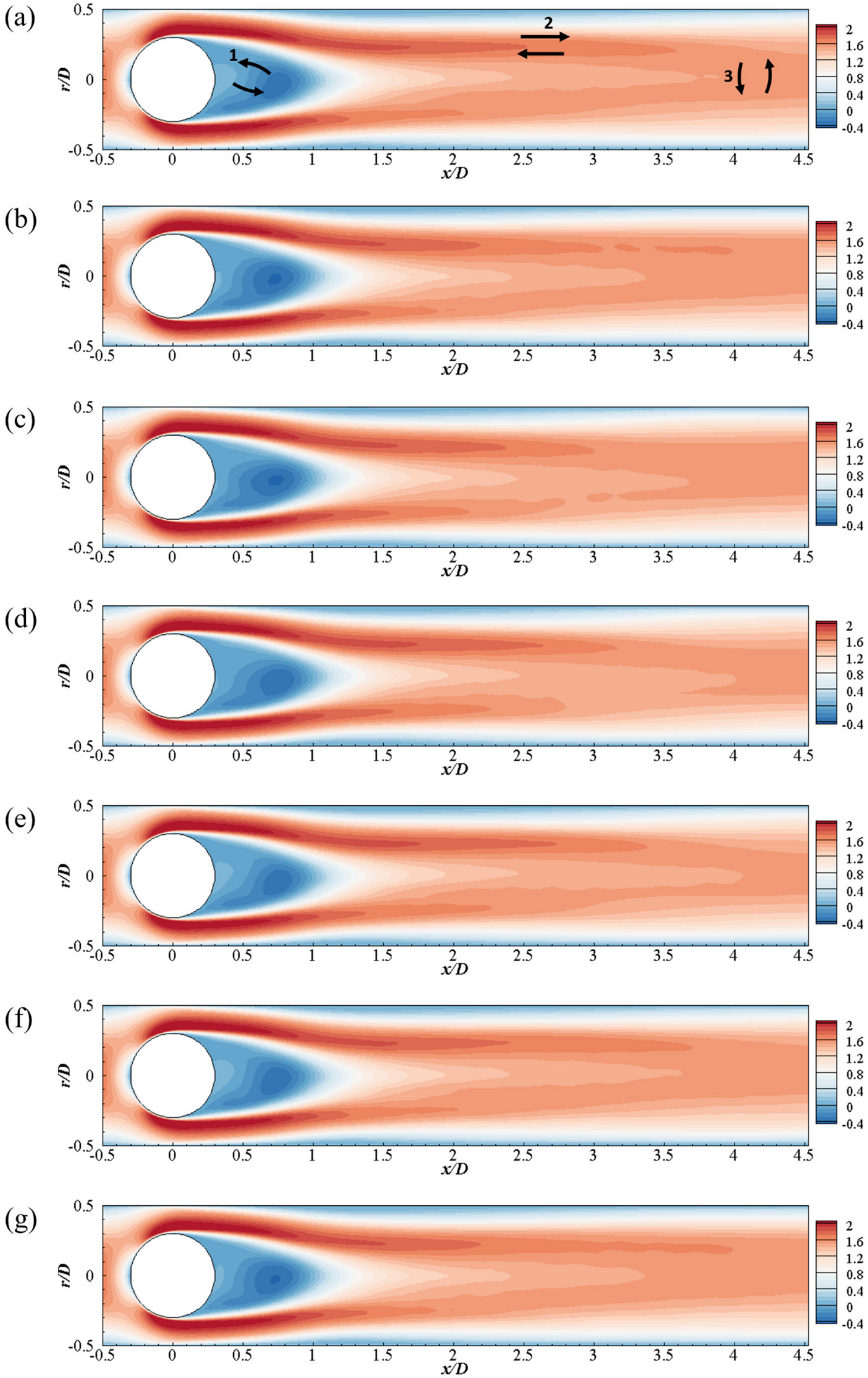
(a)
1
2
3
(b)
(c)
(d)
(e)
(f)
(g)
r/D
0.5
0
-0.5
x/D
-0.5
0
0.5
1
1.5
2
2.5
3
3.5
4
4.5
2
1.6
1.2
0.8
0.4
0
-0.4

Physics of Fluids ACCEPTED MANUSCRIPT

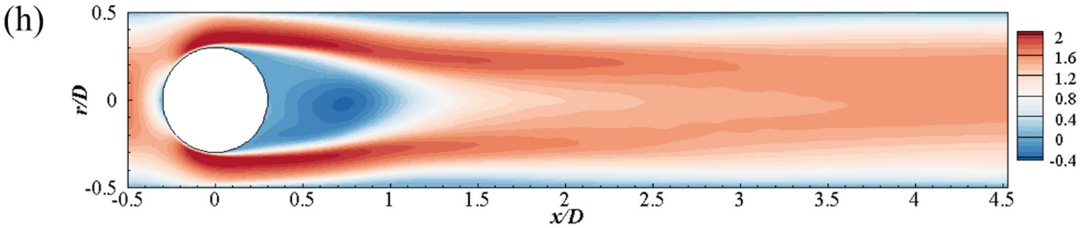

Figure 35 The streamwise velocity of the mean flow with the superposition of the low frequency DMD mode at eight instants on the XY slice at (a) $tU_\infty/d = 579.47$; (b) $tU_\infty/d = 582.2$; (c) $tU_\infty/d = 584.93$; (d) $tU_\infty/d = 587.66$; (e) $tU_\infty/d = 590.39$; (f) $tU_\infty/d = 593.12$; (g) $tU_\infty/d = 595.85$; (h) $tU_\infty/d = 595.58$

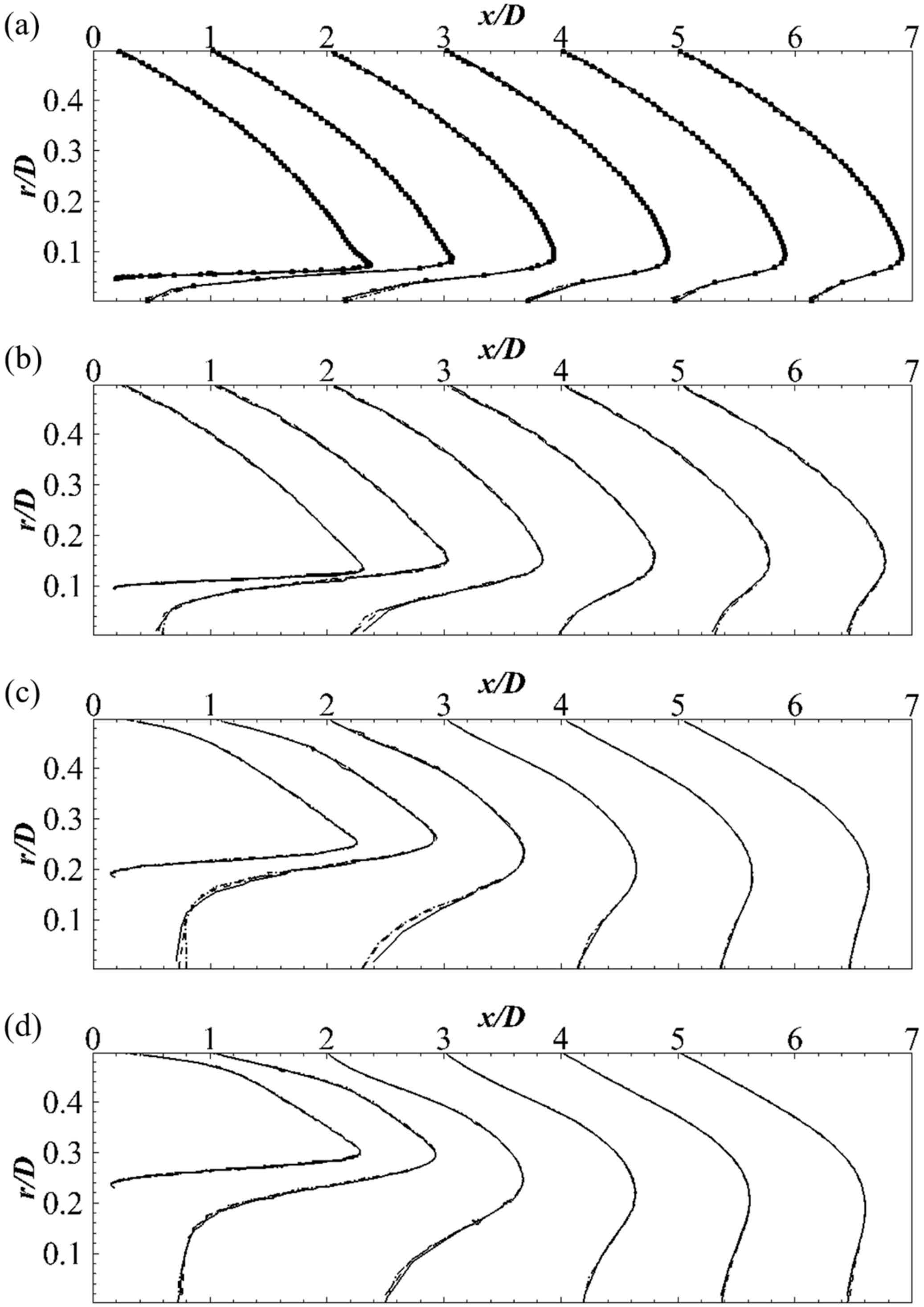
(a)
(b)
(c)
(d)
x/D
0
1
2
3
4
5
6
7
r/D
0.1
0.2
0.3
0.4

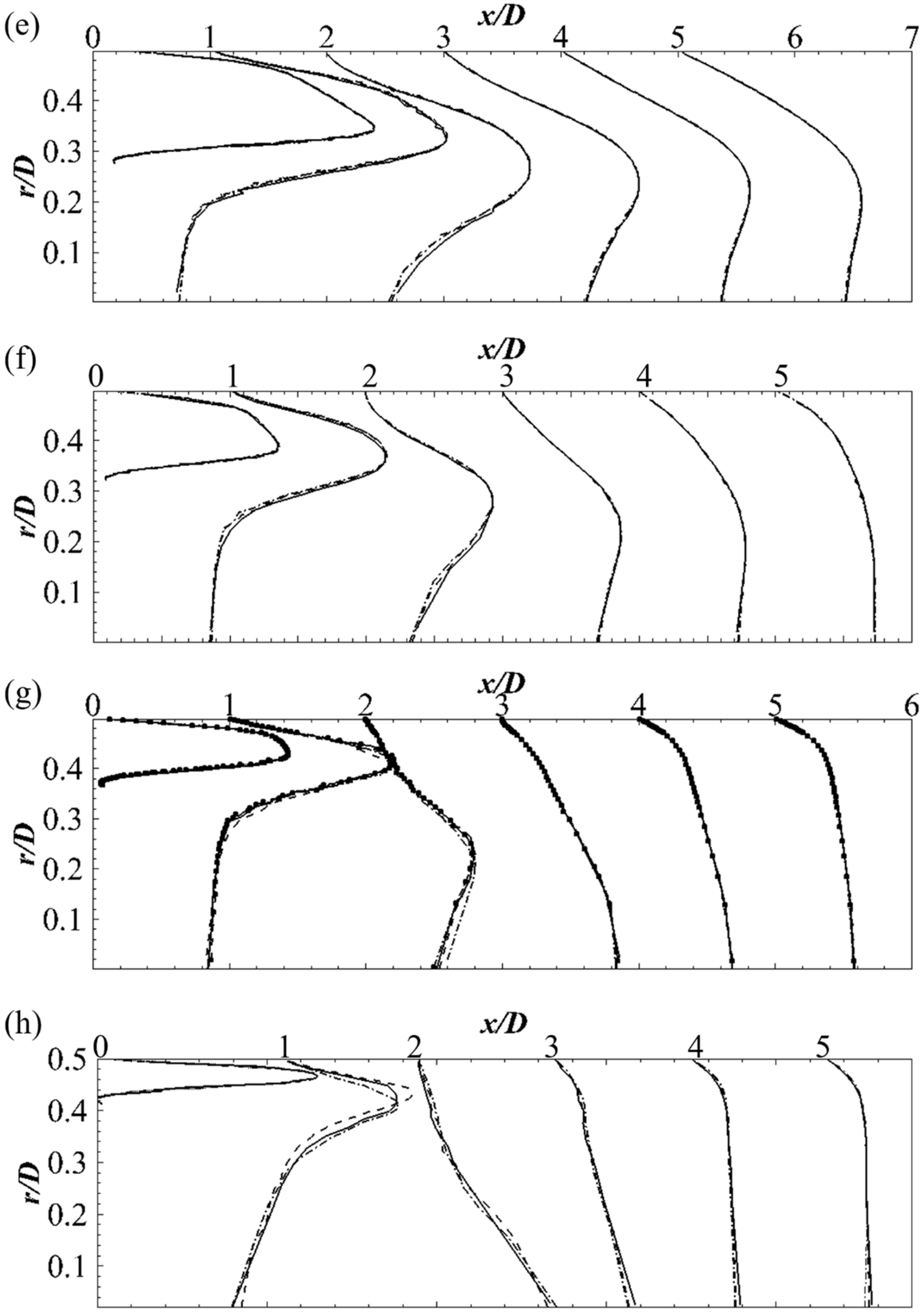

Figure 36 Azimuthal- and time-averaged streamwise profiles at the streamwise locations of $x/d = 0.2, 1, 2, 3, 4, 5$ in the wake flow behind the sphere for different grid resolutions: Case 1: Solid lines; Case 2: Dashed; Case 3: Dash-dotted; Case 4: Black circles with $BR =$ (a) 0.1; (b) 0.2; (c) 0.4; (d) 0.5; (e) 0.6; (f) 0.7; (g) 0.8; (h) 0.9

Physics of Fluids ACCEPTED MANUSCRIPT

AIP Publishing

This is the author's peer reviewed, accepted manuscript. However, the online version of record will be different from this version once it has been copyedited and typeset.
PLEASE CITE THIS ARTICLE AS DOI: 10.1063/5.0017349

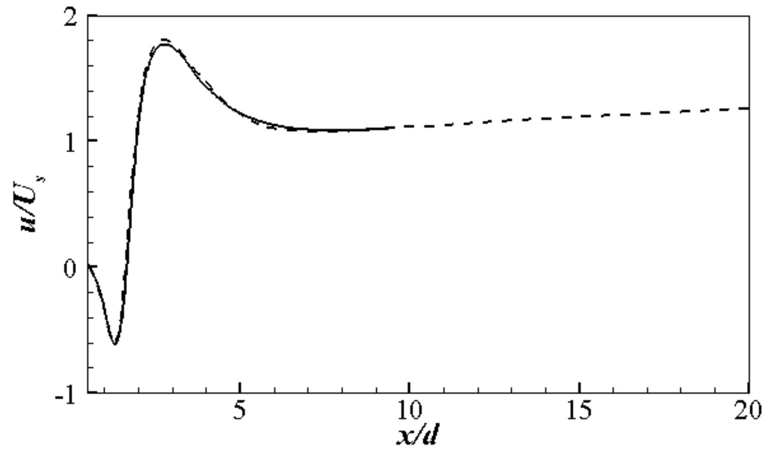

Figure 37 The time-averaged streamwise velocity along the centerline of the pipe (Solid lines: H3; Dashed: H3L)

Physics of Fluids ACCEPTED MANUSCRIPT

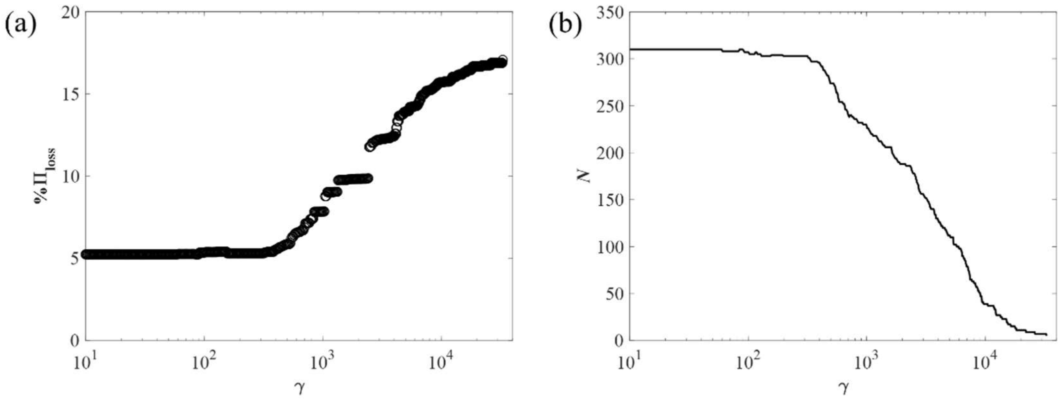

Figure 38 (a) The approximation loss Π_{loss} with γ; (b) the number of modes N retain in Eq (B1) with γ

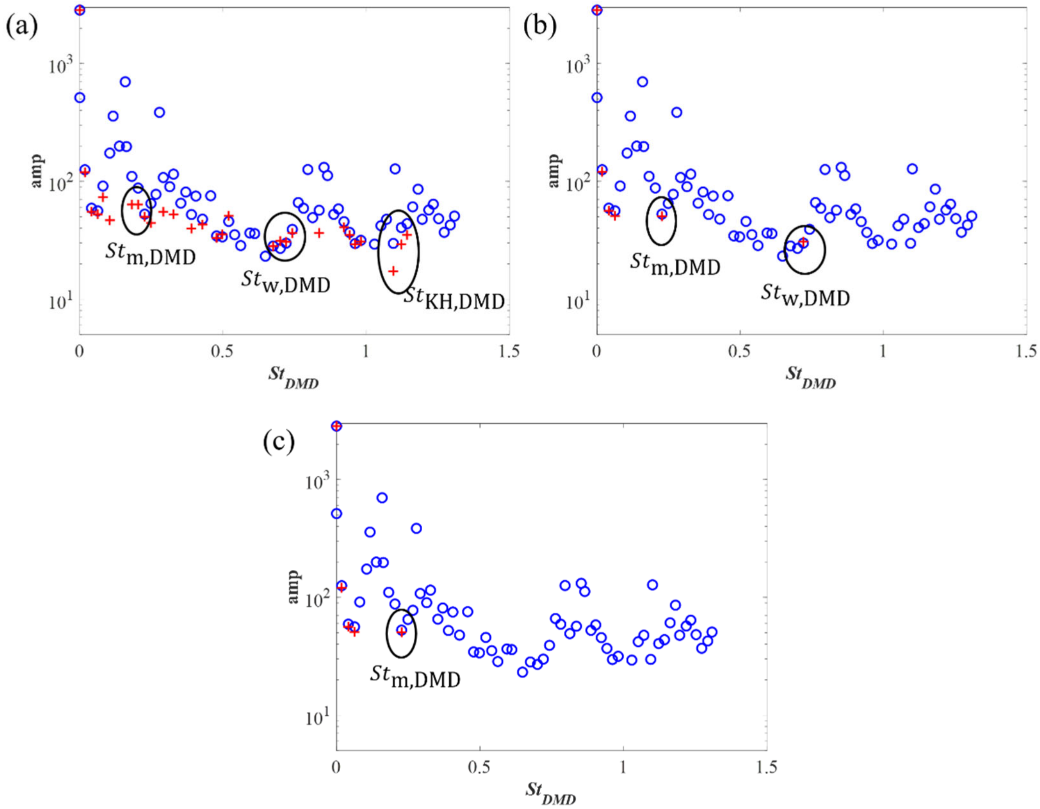

Figure 39 The frequency spectra of the DMD modes obtained by using the original standard DMD method (Blue circles) and the SPDMD (red crossings) with different number of modes (a) $N = 57$; (b) $N = 13$; (c) $N = 9$